

Organic Semiconductor Detector for Large Area Digital Imaging

by

Umar Shafique

A thesis
presented to the University of Waterloo
in fulfillment of the
thesis requirement for the degree of
Doctor of Philosophy
in
Electrical and Computer Engineering - Nanotechnology

Waterloo, Ontario, Canada, 2014

©Umar Shafique 2014

AUTHOR'S DECLARATION

I hereby declare that I am the sole author of this thesis. This is a true copy of the thesis, including any required final revisions, as accepted by my examiners.

I understand that my thesis may be made electronically available to the public.

Abstract

Organic semiconductor technology has gained attention in both the sensor and display markets due to its low cost and simple fabrication techniques. The ability to fabricate organic semiconductor devices such as photodetectors and transistors on a flexible, lightweight substrate makes them less fragile and ideal candidates for portable large-area imaging applications. The use of organic semiconductor technology in large-area medical imaging can bring about a new generation of flexible and lightweight indirect X-ray imagers. These imagers are immune to mechanical shock and should be ideal for portable intraoral X-ray radiology. In order to realize these organic flexible imagers and their use in large-area medical imaging, many challenges associated with the device performance and fabrication need to be overcome. Among these challenges, one of the greatest is to improve the dark current performance of the organic semiconductor photodetectors (key for imager performance) with a high-photo to-dark current ratio. Low dark current is needed to improve the sensitivity of the imager, whereas a large photo-to-dark current ratio reduces noise in the extracted image.

Numerous techniques have been reported to improve the dark current performance in vertical organic photodetector design; however, lateral photodetectors still lack research attention. This thesis presents a lateral multilayer photodetector design and a simplified technique to improve the dark current performance of lateral organic semiconductor photodetectors. Our technique allows us to apply a large bias voltage while maintaining a low dark current, high photo-to-dark current ratio, and improves detector speed; thus, the overall sensitivity of the detector is improved.

We further show the integration of an organic photodetector with an organic backplane readout circuit to form a flexible large-area imager. This imager can be used for large-area digital imaging applications such as in medical radiology.

Acknowledgements

I would like to thank my supervisor Prof. Karim S. Karim for his continuous support, his valuable advice and encouragement throughout my doctoral studies. I would like to thank my parents, Mr. Muhammad Shafique, Mrs. Shahida Shafique, my brother Shahid Shafique, my sister Khadija Tahira, and wife Amna Umar, whose prayers, love and encouragement gave me strength to accomplish and struggle to achieve my goals and be successful in my life

I would like to thank the other committee members, Dr. Craig S. Levin, Dr. Omar Ramahi, Dr. Eihab Abdel Rahman and Dr. Bo Cui for their keen and expert advice on my work. I would like to thank Janet Mary McPherson for her kind and extraordinary help and teaching to polish my writing.

Many thanks to Dr. Gerwin H. Gelinck from the HOLST Center in the Netherlands for giving me an opportunity to work on novel flexible X-ray imagers, at the world-class research and development facility at the Hi-Tech campus at Eindhoven. Thanks to my colleagues and friends at HOLST and the MI-Plaza Philips labs team for their expert input and endless efforts to accomplish the key milestones of the project. Above all, I thank them for providing me with the read-out images of our shared work so that I could see the outcome of the flexible X-ray imager that I helped to design.

Special thanks to Ir. Alexander U. Douglas and Dr. Matthias Simon from Philips Research, Medical Imaging who taught me new understanding of problems and ways to effectively solve them quickly. I thank them for listening to me for hours, for sharing their resources for an extended time, and for always being a major source of help.

I would like to thank Richard Barber for his endless support in keeping the G2N tools and lab operational, in ensuring our safety in the clean room, and for his valuable suggestions and friendly talk.

I am thankful to Dr. Clara Santato and her working group at Ecole Polytechnique de Montreal for hosting my research activities in her lab and for her endless support both professional and personal. Special thanks to Dr. Khasan S. Karimov, Dr. Sue Horton, Dr. Hany Aziz, Dr. Siva Sivoththaman, Dr. Svitlana Taraban Gordon, and Dr. Mary A. Wells, for being a friends and excellent mentors. Special thanks to my friends who contributed in every step of my PhD life.

Lastly I would like to thank the my colleagues, G2N lab members, the WIN community, the STAR group members, the ECE department faculty and staff, and the Graduate Students Association for making my journey joyful and full of success.

Dedication

*Dedicated to my family, especially my mother **Mrs. Shahida Shafique** (late) and father **Mr. Muhammad Shafique**.*

Table of Contents

AUTHOR'S DECLARATION	ii
Abstract.....	iii
Acknowledgements	iv
Dedication.....	vi
Table of Contents	vii
List of Figures.....	ix
List of Tables	xiii
Chapter 1 Introduction.....	1
1.1 Large-area Digital Imaging	1
1.2 Organic Semiconductor Technology	4
1.3 Organic Semiconductor Photodetectors	4
1.4 Organic Semiconductor Imagers	7
1.5 Thesis Motivation and Organization	8
Chapter 2 Background	10
2.1 Organic Semiconductors	10
2.1.1 Organic Semiconductor Materials	12
2.2 Organic Semiconductor Photodetector.....	16
2.2.1 Dark Current (Charge Injection)	17
2.2.2 Charge Transport	18
2.2.3 Hopping Transport.....	19
2.2.4 Excitons (Photogeneration)	20
2.3 Organic Semiconductor Large-area Digital Imagers.....	22
2.4 Organic Semiconductor Fabrication.....	24
Chapter 3 Flexible X-ray Imager.....	26
3.1 Introduction	26
3.2 Experiment	27
3.3 Results and Discussion	33
3.4 Conclusion.....	41
Chapter 4 Lateral Organic Semiconductor Photodetector	42
4.1 Introduction	42
4.2 Dual Layer MSM Photoconductor	43

4.3 Lateral Photodetector Design with Interface Layers.....	47
4.3.1 Introduction.....	47
4.3.2 Method and Materials	47
4.3.3 Results and Discussion.....	48
4.3.4 Conclusion	67
Chapter 5 Effect of Spacing in MIOSIM Photodetectors	68
5.1 Introduction.....	68
5.2 Method	69
5.2.1 Design and Fabrication	69
5.2.2 Measurement.....	70
5.3 Photodetector performance	70
5.3.1 Polystyrene: Conduction.....	73
5.3.2 Effect of Electrode Spacing	74
5.4 Mathematical Analysis.....	77
5.5 Conclusion	80
Chapter 6 Summary and Contributions.....	81
6.1 Summary	81
6.2 Contributions.....	82
Bibliography.....	84

List of Figures

Figure 1.1 An active matrix imager. Each pixel is made of a photodiode and Thin Film Transistor (TFT). Columns are connected to the TFT gate; rows are the output line to read data and are connected externally to charge amplifiers and later to analog-to-digital converters and memory..	2
Figure 1.2: Signal conversion principle of an active matrix detector: with indirect-amorphous silicon (a-Si) detectors. As with direct-amorphous selenium (a-Se) detectors, electronic charge is accumulated after X-ray exposure followed by the readout through a thin-film transistor (TFT) switches before analog-to-digital signal conversion [6].....	3
Figure 2.1 Energy Diagram of two carbon atoms with sp^2 and p_z orbital forming a non-bonding orbital, σ and π molecular orbital. The electrons in the orbital are filled according to Hund's rules for spins. The interaction of two carbon atoms ($C=C$) results in splitting of the p_z orbital in to π and π^* molecular orbitals [38].....	11
Figure 2.2 Schematic representation of the energy gap of Ethylene, Butadiene, Octatetraene and Polyacetylene, showing the energy band gap reduction with increased conjugation.....	12
Figure 2.3 Detection mechanism in a lateral organic semiconductor heterojunction	17
Figure 2.4 LUMO and HOMO Energy level, Gaussian function approximation	19
Figure 2.5 Schematic representation of the various types of excitons in semiconductors and insulators. Frenkel exciton (Blue) is small radius. Large radius (Red), Wannier-Mott exciton commonly found in inorganic semiconductor materials. Intermediate radius (green) charge transfer (CT) exciton [48].....	21
Figure 2.6 An passive pixel design.....	23
Figure 2.7 An active pixel design using three transistors.....	23
Figure 2.8 Block diagram representation of a thermal evaporator system.....	25
Figure 3.1 Design lay out of 32-row and 32-column array, with $1 \times 1 \text{ mm}^2$ pixel size (left) and $200 \times 200 \mu\text{m}^2$ pixel size (right).	28
Figure 3.2 Cross section of pixel (a), and top view (b). Schematic circuit representing a single pixel with integrated OTFT and OPD (c). Voltage on a pixel node versus time for different light intensities, during one frame time (d).....	29
Figure 3.3 Effect of Water on the backplane OTFTs: Plot of gate voltage vs. drain current at drain source voltage of -10V and -1V, before (a) and after (b).....	30
Figure 3.4 Effect of Dichlorobenzene on the backplane OTFTs: Plot of gate voltage vs. drain current at drain source voltage of -10V and -1V, before (a) and after (b).....	31

Figure 3.5 Cross-sectional layout OPD on TFT anode, including transparent cathode stack and barrier layer.....	32
Figure 3.6 OTFT current of 40 transistors measured at +10V and -20V: OFF current (black) and ON current (red). The inset shows the transfer characteristics for a typical organic TFT fabricated with the complete image sensor process on a PEN plastic substrate, as well as the molecular structure of the precursor pentacene that is converted to pentacene by a thermal annealing step. The transistor channel length and width are 5 and 140 μm , respectively (a). Photograph of a flexible TFT array plus fan-out circuitry (b). Current–voltage characteristics of a large-area (12.5 mm^2) organic photodetector in the dark and under illumination at several different intensities (incident wavelength is $\lambda = 525 \pm 3 \text{ nm}$) (c). Plot of current density at -2 V vs. light intensity, plus linear fit (d).....	35
Figure 3.7 Characteristics of the 25 ppi array. (A) Histogram of background current (black) and photocurrent (grey) of 1024 pixels. (B) Recorded photo-image. A key was placed on the array (see inset). (C) X-ray image of 3 circular lead objects (with radii of 5 mm and 3 mm, respectively) recorded with a dose of 1.2 mGy s^{-1} . In all cases, the transistors were biased at a gate voltage of -20 V or $+10 \text{ V}$, and the common cathode was biased at -2 V	36
Figure 3.8 Pixel current density at -2 V as a function of light intensity for the 25 ppi (circles) and 127 ppi photodetector array (triangles). The (linear) slopes of the $1 \times 1 \text{ mm}^2$ and $200 \times 200 \mu\text{m}^2$ pixels are 0.86 and 0.81, respectively. When calculating the current density, the effective diode array is used because the TFT current is negligible.....	37
Figure 3.9 (A) X-ray image of a lead object with slits (lines and spaces of varying dimensions). The lead object was placed such that the pattern of lines and spaces becomes progressively wider from the left bottom corner to the right upper corner of the array. (B) Photograph of the actual object, imaged in (A).	38
Figure 3.10 Histogram of measured photocurrent of 25 ppi array before and after exposure to heavy X-ray dose (estimated total dose 0.5 Gy).....	39
Figure 3.11 Characteristics of the 127 ppi array. (a) Top view micrograph of $200 \times 200 \mu\text{m}$ sensor pixels in 127 ppi backplane array. Row and column electrodes, active TFT area and pixel electrode are clearly visible. (b) Photo-image recorded by illuminating the detector array through a metal mask with square holes of 1.6 mm in a checkerboard pattern. Pixels in the lighter parts are exposed, pixels in the darker parts are not exposed. (c) Micrograph of ~ 10 pixels in array that are fully or partially exposed through a pinhole in metal, and its photo-image. (d) Photo-images	

were recorded by biasing the transistors with a gate voltage of -20 V or $+10\text{ V}$ during selection and non-selection, respectively, and the common cathode at -2 V .	40
Figure 4.1 Single layer device photo current and dark current at different voltage biases, PTCBI-only device (a), CuPc only device (b)	45
Figure 4.2 Dual layer device photo current and dark current at different voltage biases, CuPc bottom and PTCBI on top (a), PTCBI bottom and CuPc on top (b)	46
Figure 4.3 (a) Absorbance as a function of wavelength of thin film of polystyrene (50nm), CuPc (30nm) PTCBI (50nm) and combined three-layer polystyrene (50nm): CuPc (30nm): PTCBI (50nm). Inset shows the lateral interdigitated electrodes patterned on glass, with an electrode spacing of $5\text{ }\mu\text{m}$, and overall area of 1 mm^2 with active area of $5.0\times 10^{-3}\text{ cm}^2$, device cross sectional layout: Aluminum metal electrodes with length of $5\text{ }\mu\text{m}$, 1 mm width channel, $5\text{ }\mu\text{m}$ wide metal electrode; thermally evaporated Polystyrene (PS); 50 nm , PTCBI; 30 nm CuPc. (b) Energy diagram of the photodetector. (c) Device cross sectional layout explaining the dark and the photoconduction.	50
Figure 4.4 IR-Spectrum of polystyrene thin film and polystyrene base material.	51
Figure 4.5 I-V Response: under dark with no polystyrene and with polystyrene of thicknesses of 10 , 50 , 100 nm , showing a significant reduction in dark current.	52
Figure 4.6 Current voltage characteristics of polystyrene only device under dark and 1 W/cm^2 of white light. No conduction in lateral $5\text{ }\mu\text{m}$ channel is observed in dark either or light.	53
Figure 4.7 Current voltage characteristics of polystyrene with aluminum top electrode under dark and 1 W/cm^2 of white light, showing conduction at a threshold voltage at 5 V across the lateral electrodes in lateral $5\text{ }\mu\text{m}$ channel with no observable photo response.	54
Figure 4.8 Current-Voltage characteristics of the lateral MIOSIM with no PS (a), 10 nm PS (b), 50 nm PS (c), 100 nm PS (d). The photocurrent is measured under illumination power of $100\text{ }\mu\text{W/cm}^2$ using a Green (525 nm), Blue (480 nm) and Red (650 nm) LED light source.	56
Figure 4.9 Plot of photo-to-dark current ratio versus applied voltage for a $100\text{ }\mu\text{W/cm}^2$ green (525 nm) light for samples with 10 nm , 50 nm , 100 nm thick PS and without PS.	57
Figure 4.10 (a) EQE as a function of applied voltage with no PS; (b) EQE as a function of applied voltage with 10 nm of PS; (c) EQE as a function of applied voltage with 50 nm of PS; (d) EQE as a function of applied external voltage with 100 nm of PS.	58
Figure 4.11 Photo-to-dark current ratio and external quantum efficiency as a function of applied bias using 525 nm wavelength LED at an illumination power intensity of $3.6\text{ }\mu\text{W/cm}^2$.	59

Figure 4.12 (a) I-V Response of 50 nm PS detector at range of illumination intensities; (b) Linearity plot, photo current as a function of light power using a 525 nm LED source at 5 V, 10 V 15 V 25 V external bias voltages	60
Figure 4.14 Transient response for 500 second run show detector following the input signal. The on and off current do not change over time.	63
Figure 4.15 A lateral photodetector with 40 nm-PTCBI, Current Voltage characteristics under different illumination of light.....	64
Figure 4.16 Lateral photodetector with 40nm -PTCBI, transient, rise time and fall time under different bias voltages	65
Figure 4.17 Capacitance as a function of frequency at different intensities of green light	67
Figure 5.1 (a) Schematic crossection of lateral bilayer organic semiconductor; PS is used as interface layer in between metal contacts and organic semiconductor bilayer. (b) Energy diagram representation. (c) Molecular structure of PTCBI, (d) Molecular structure of CuPc	69
Figure 5.2 Block diagram of the measurement setup used to characterize the devices	70
Figure 5.4 Measured absorbance spectrum (400nm to 800nm wavelength) of all three layers (plotted in black) and only PS.	74
Figure 5.6 Log-log plot for sensor (D1, D3 and D4) photocurrent vs voltage (solid plot) at light power of $400 \mu\text{W}/\text{cm}^2$ and nonlinear fit plots (dotted plot)	79

List of Tables

Table 2.1 Example of organic semiconductor materials, molecular structure and HOMO, LUMO energy level with reference to vacuum.....	15
Table 4.1 Single and double layer devices, cross-sectional layout and energy diagram.....	44
Table 4.2 Table summarizes the rise and fall times of D1, D2, D3 and D4 photo detectors	61
Table 4.3 Photodetector with 40nm of PTCBI, summary of rise time and fall time of photodetector at different applies biases	66
Table 5.1 EQE of lateral organic bilayer photodetector without-PS and with different thicknesses of PS at 5 V, 10 V, 15 V and 20 V applied bias voltages	72
Table 5.2 EQE at low illumination power	72
Table 5.3 Devices dimensions, electrode width and electrode length.....	75

Chapter 1

Introduction

Organic semiconductor technology holds great promise for large area, low cost electronics applications [1] [2]. Large-area detectors and displays, when fabricated using organic semiconductor technology, can bring new features such as printability, light weight, structural flexibility, making them ideal for portable applications[3] [4]. Organic semiconductor large-area technology uses low processing temperatures, which allows the use of low cost plastic substrates to make mechanically flexible devices (backplanes). These flexible imagers are immune to mechanical shocks and are less fragile than existing imagers made with glass substrates. Notable applications of these imagers are in both the sensor and the display industries, particularly when coupled with a scintillator that can be used for indirect radiation detection, for example in X-ray digital detectors. X-ray imagers require a detector to be equal to or larger than the size of the object to be imaged, matching the technological advantage of using organic semiconductor technology in the large area imaging industry.

This thesis presents the use of organic semiconductor technology in the X-ray imaging industry, to use in fabricating large-area flexible X-ray detectors. In addition, it introduces a lateral multilayer detector design based on organic semiconductor technology. These lateral multilayer organic semiconductor detectors can be integrated with backplanes to improve the performance of organic imagers. The proposed detector design has low dark current and can be operated at high speed under high bias voltage.

The work presented in this thesis complements the existing large-area technology, particularly to fulfill the emerging need for low-cost portable medical diagnostic equipment for improved health care.

This chapter summarizes the existing organic semiconductor technology in reference to large-area digital imaging (X-ray medical imaging). An outline of the thesis and the motivation for this work are included at the end of the chapter.

1.1 Large-area Digital Imaging

The large area digital imaging systems used today are made of active matrix flat panel digital detectors. These flat panel imagers consist of pixels (as building blocks) with a linear or a two dimensional architecture. Photocopiers and office scanners are examples using linear architecture,

whereas digital lens-less cameras and X-ray imagers use two-dimensional architecture. Each pixel in a digital imager consists of two parts: a detector and a switch. Thin Film Transistors (TFTs) are used for switching and provide addressing capabilities to the digital imager. A schematic diagram of an active matrix imager is shown in Figure 1.1.

The readout switch can be simple, such as in a one-transistor passive pixel design, or more complex, with an embedded on-pixel amplifier circuit using a multiple-transistor active pixel design. Gate and data interconnection lines (rows and columns interconnect) are used to drive the TFTs and readout individual rows and columns of an imager. The interconnect lines are further connected externally onboard electronics such as charge amplifiers and timers, to sequentially drive the TFTs and readout the photodetector diode response for an incident (light) signal.

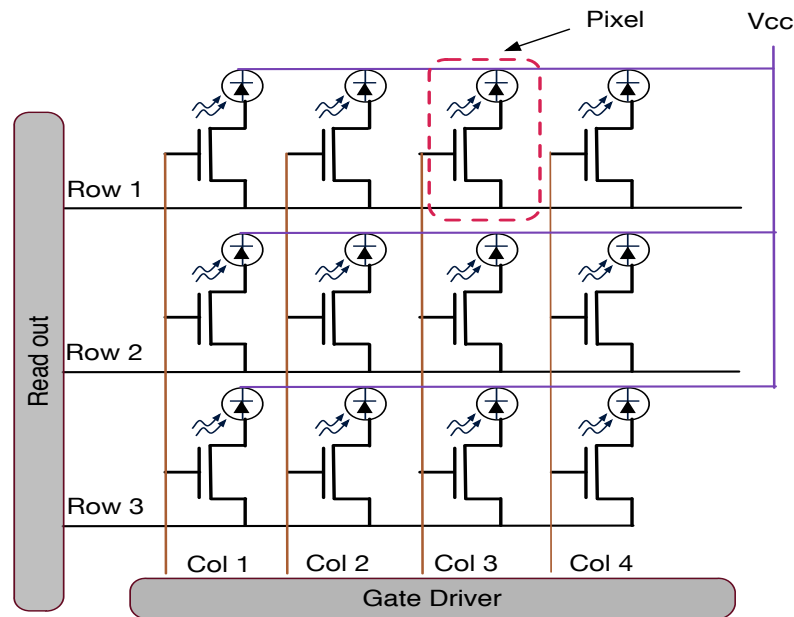


Figure 1.1 An active matrix imager. Each pixel is made of a photodiode and a Thin Film Transistor (TFT). Columns are connected to the TFT gate; rows are the output line to read data and are connected externally to charge amplifiers and later to analog-to-digital converters and memory

At present, commercial flat panel imagers use amorphous silicon (a-Si) technology to fabricate both the detector and the TFT backplane. These (a-Si) panels have been actively used for digital radiology and X-ray imagers for medical imaging applications [5]. The motivation to use Active

Matrix Flat Panel Imager (AMFPI) design in X-ray imaging is to achieve a better quality image under low dose X-ray, to make it easy to store and digitally transport the image. The extracted image is in the form of digital data and can be analyzed later using computational and image processing techniques to extract useful information.

The two schemes used to detect X-rays are direct detection and indirect detection. These schemes are presented in Figure 1.2. [6]

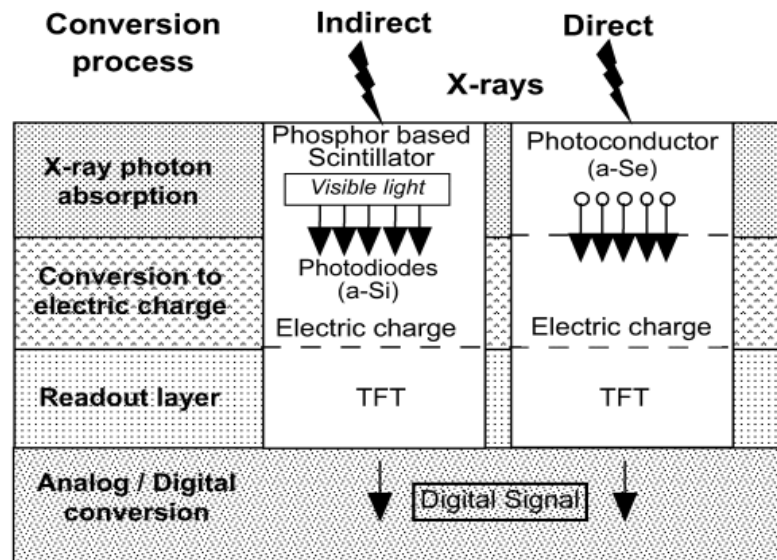


Figure 1.2: Signal conversion principle of an active matrix detector: with indirect-amorphous silicon (a-Si) detectors. As with direct-amorphous selenium (a-Se) detectors, electronic charge is accumulated after X-ray exposure followed by the readout through a thin-film transistor (TFT) switches before analog-to-digital signal conversion [6]

In the case of direct detection, the incident X-rays are absorbed by the detector. As a result, an X-ray beam generates an electric charge, for example, in the case of amorphous selenium (a-Se) [5]. In contrast, during indirect detection, the incident X-rays are first converted into visible light using a phosphor material layer. The viable light is then subsequently absorbed by the photodetector's photoactive layer and an electric charge is generated [6].

Most of the commercially available detectors are indirect detectors made using a-Si technology; direct detectors use amorphous selenium as a detector-active, X-ray-absorbing material. Amorphous silicon technology is used to fabricate the flat panel backplane TFT circuits. These panels are

fabricated on a specialized rigid glass substrate at a processing temperature of $\sim 300^{\circ}\text{C}$ and above. The use of a glass substrate adds substantial weight to the overall detector and requires a damping mechanism to protect the glass from breaking due to shocks and bumps received during use.

1.2 Organic Semiconductor Technology

Low equipment cost and the ability to fabricate devices at low temperature make organic semiconductor technology an attractive alternative to the existing amorphous silicon technology. Both the sensor and display industries have shown strong interest in using organic semiconductor material in their displays and imagers. Thin films of organic semiconductor materials can be processed at low temperatures (less than 150°C) using simple fabrication techniques ideal for mass production such as ink-jet printing, roll-to-roll printing, and screen-printing, etc. Low temperature processability allows using inexpensive plastic substrate materials. Organic semiconductor materials are amorphous and soft with a low index of refraction, which allows high absorption of light for a couple of nanometers thick organic film and greater absorption bandwidth. These materials, when processed on a plastic substrate become structurally flexible and lightweight, making them attractive to the large-area-imaging industry for portable imaging equipment [3].

1.3 Organic Semiconductor Photodetectors

Organic semiconductor photodetectors (OPD) operational abilities have been reported for different spectral regions, ranging from ultra-violet (UV) to near infra-red (NIR) light. Recently, the use of organic semiconductor photodetectors has been actively explored for the visible wavelength, in particular for detection of green wavelength light (520nm to 55nm). The driving force behind the OPD development in the visible spectrum is akin to the growing interest of research and industry in using organic semiconductor detectors in radiology applications, in making sensors, backplanes or the entire imager for indirect X-ray imaging [7], [8]. These organic detectors use small-molecule or polymer organic semiconductor materials in the form of a donor acceptor (D/A) heterojunction.

A heterojunction is an interface between two organic semiconductor materials with different energy gaps. C. W Tang, in the 1980's first reported the use of heterojunctions to achieve highly efficient devices [9]. Since then, heterojunction designs have been adapted for organic semiconductor devices architecture, to improve the Organic Light Emitting Diode (OLED) illumination efficiency, to improve the photo-generation efficiency of organic photosensor and photovoltaic devices and high mobility in the case of organic transistors [10] [11] [12] [13]. Organic semiconductor devices, organic

photovoltaic (OPV), light emitting diodes (OLED), thin film transistors (OTFT) and photodetectors (OPD) can have a single or multiple heterojunction structure. The heterojunction structure can be in the form of layers or a single layer with a bulk mixture. A layered heterojunction is easy to process using small-molecule materials, whereas bulk heterojunction structures are more commonly used and easily processable in polymers and organic semiconductor materials.

The two popular photodetector designs reported for organic photodetectors are vertical and lateral. In vertical organic photodetector design, an organic semiconductor heterojunction layer is sandwiched in between two metal electrodes with different work functions. In lateral organic photodetector design the two laterally spaced in-plane electrodes, above or under the organic semiconductor layer. A vertical detector design requires at least one metal side to be optically transparent so that light can enter and be absorbed by the photoactive layer. The most commonly used transparent conductive electrode today is Indium Tin Oxide (ITO).

Organic semiconductor heterojunction photodetectors consisting of multiple alternating layers of small-molecule organic semiconductors were reported for the first time by Forest's group in, 2000. These detectors showed a peak external quantum efficiency (EQE) of 75% and an operational bandwidth of 430 MHz. Copper phthalocyanine (CuPc) and 2,4,9,10-perylenetetracarboxylic-bis-benzimidazole (PTCBI) organic semiconductor materials were used to create a multilayer donor and acceptor heterojunction. The detector response has been studied by changing the number of alternating layers. The detector's external quantum efficiency (EQE) at different reverse bias voltages is reported. Multilayer detector with a thickness of less than 30 Å (each layer is 5 Å) showed an increase in quantum efficiency, which features to the increase in carrier collection efficiency due to the tunneling of photo-generated charges through the energy barriers between layers. Detectors with active layers thicker than 30 Å showed a slow increase in the EQE with an increase in applied bias. The slow increase in EQE is concluded to be due to the field-induced dissociation of excitons. The dark current densities of 2-, 4-, 16-, and 32-layer devices were reported at a different bias voltages in reverse bias. An increase in dark current have been reported with an increase in the number of layers (active layer). The dark current density of a two layer (10 Å thick) detector increases from $\sim 10^{-9}$ A/cm² to $\sim 10^{-7}$ A/cm² for a 32-layer device (160 Å thick) [14].

The charge transport mechanism in the organic active region and organic anode interface have been studied in a similar design, using small-molecule (CuPc-PTCBI) multilayer photodetectors. The study suggested that the photo-generated charge carriers escape the potential wells formed in the organic

multilayer stack via tunneling across the donor-acceptor interface. A weak temperature dependence of the photocurrent was observed, and electron injection has been reported as the main source of dark current. A high quantum efficiency and high speed of response can be achieved if the individual layers in the active region are thin enough such that the photo-generated carrier can tunnel through them and be collected at the opposite electrode. The anode metal needs to be a high work function metal to limit the injection of electrons from the anode to the organic active layer. This metal reduces the dark current under reverse bias operations. The anode organic junction (metal semiconductor junction) can be engineered to reduce injection, or a new material layer can be introduced in between the metal and organic semiconductor interface, acting as a charge-blocking layer. The interface layer, alternately called the blocking layer, should limit only one type of carrier. In both vertical and lateral detector designs the charge-blocking layer limits the injection of charges from the metal in to the organic semiconductor. It also protects the organic layer from damage and defects that originate due to defects arising during metal deposition above the organic semiconductor surface. Surface defects are a source of charge trapping and photon quenching, and are one of the main reasons for slow operation of these devices.

High-speed detectors have been reported using Pentacene and C60-based bilayer vertical designs. Applications of these detectors include very high frequency (VHF) optical-signal sensing and detection [15]. Other systems of small-molecule organic semiconductors with combinations of different organic semiconductor materials have been reported [11], [16]. These systems are being using combinations of material and to form an efficient donor-acceptor heterojunction, hence improved performance. Similarly, small-molecule organic semiconductor photodetectors with low dark current and high selectivity and their use in large-area imaging applications has recently been shown [17], [18].

In contrast to small-molecule devices, solution-processed devices are simple to fabricate, but the morphology of heterojunctions at the nano-scale is poorly controllable [11], requiring suitable solvents, thin film deposition techniques and an adequate control over the processing temperatures. Poly(3-hexylthiophene) (P3HT) and [6,6]-phenyl-C₆₁-butyric acid methyl ester (PCBM) are the two most-studied polymer materials, and can be solution processed. These materials have a broad absorption spectrum, ranging from the 400 nm to 600 nm wavelength, and high carrier mobility. Interest in these polymers is driven by their excellent optoelectronics properties and also their extensive applications in the solar cell industry. The wide spread use of these materials has resulted in

the clarification of many optoelectronics properties and very good control processes to tune the material molecular structure and to achieve desired properties. Most of the P3HT:PCBM-based devices reported today use vertical device geometry. However the lateral geometry is most commonly used to study the charge generation and transport mechanism in lateral bulk P3HT:PCBM blends [19].

Other sets of very popular Donor/Acceptor materials, i.e., poly[2-methoxy-5-(2-ethylhexyloxy)-1,4-phenylene-vinylene] (MEH-PPV) or poly(2-methoxy-5-(3'-7'-dimethyloctyloxy)-1,4-phenylenevinylene) (MDMO-PPV) and the PCBM, devices reported using these material report a high EQE of around 60% at the blue and green light wavelength [20]. Higher analogues of PC61BM like PC71BM have also been synthesized to an extended optical absorption window toward the visible spectrum, and many application have also been proposed in literature [21].

Lateral bilayer heterojunction photoconductors using PTCBI and N,N'-bis(3-methylphenyl)-N,N'-diphenyl-1,1'-biphenyl-4,4'-diamine (TPD) have been used as chemical detectors for chemical-sensing application [22]. The sensing mechanism is the optical, organic semiconductor PTCBI, used as the exciton-generating layer and TPD, for charge transport. These two materials are selected such that a separately control of generation and charge transport in an organic semiconductor photoconductor. The lateral bilayer detector has a photo-to-dark current ratio of maximum 100, with an external quantum efficiency of 12% at an applied electric field of 1.25×10^5 V/cm. Other lateral detector use material systems such as quantum dots or nanowires [23].

Alternative methods such as spray coating have been reported for fabricating P3HT:PCBM bulk heterojunction organic photodiodes. These photodetectors show dark in the range of 10^{-5} mA/cm² and an EQE of 76% (at -5V). In solution-processed devices, the reported dark current density is in the range of 10^{-3} mA/cm² down to 8×10^{-7} mA/cm² at -2V bias voltage [24-30].

1.4 Organic Semiconductor Imagers

Large area imagers using organic semiconductor technology have been reported. These imagers are either all organic or hybrid structures. The first all-organic active matrix sheet imager has an effective sensing area of 5×5 cm²; the resolution of the imager is 36 dots per inch, with total number of 5184 cells. Pentacene transistor backplanes and small-molecule organic semiconductor photodetectors are integrated using silver paste to form contacts. [31]. A 4x4 active matrix imager using solution

processed organic photodiode and organic transistor (OTFT) has also been reported. The integrated photodiode (OPD) is a lateral design, and is in plane to the OTFT [32]. A Vacuum-deposited molecular organic photodetector (OPD) integrated with a top gate, bottom-contact, pentacene-based organic thin film transistor (OTFT) for use as a switchable organic passive pixel sensor in focal plane imaging arrays is reported by Forest's group [33]. Solution-processed OPDs have been integrated with a CMOS backplane for a Hybrid CMOS imager [34]. An active pixel concept combined with an organic photodiode for an a-Si imaging devices is presented using a-Si backplanes [25]. The integration of photodiodes with oxide transistors to form a flexible imager have also been reported [35]. The use of organic semiconductor devices for X-ray was first presented by Blakesley et al. [36]

The above literature review shows a serious interest in the development of large area organic semiconductor devices at low cost, as a lightweight alternative to the existing large-area imager technology.

1.5 Thesis Motivation and Organization

The motivation of the present work is to fabricate low-cost, large-area, flexible digital imagers for X-ray imaging. These imagers are lightweight and immune to structural damage resulting from minor shocks and bumps while handling. These imagers can be coupled to a variety of highly efficient scintillators for high quality X-ray images.

In addition, we have developed a new technique to control the dark-current and photocurrent performance in a lateral photoconductor, with the advantage of applying high bias voltages to improve the imager performance when integrated to a backplane.

The organization of this thesis is as follows:

Chapter 1: Summarizes the existing organic semiconductor technology in reference to large area digital imaging in particular for indirect X-ray imaging.

Chapter 2: presents a brief background on organic semiconductor materials, devices and fabrication technology

Chapter 3: describes a novel, fully flexible large-area X-ray imager on a plastic substrate. Optical and X-ray measurements are performed, and the performance of the imager is evaluated.

Chapter 4: Explores an alternative approach to vertical photodetector design. A lateral organic multilayer photodetector design and a technique to tune the dark current performance of the photodetector is presented. The performance of the detector is further measured, both in darkness and in light.

Chapter 5: consider the effect of electrode spacing in a multilayer detector design with the use of an interface layer. It also shows the non-intuitive effect of channel spacing and device physics.

Chapter 6: concludes the thesis.

Chapter 2

Background

Organic semiconductor materials are mainly compounds composed of carbon and hydrogen atoms. In the past, organic materials were once treated as naturally occurring one that could not be synthesized artificially. However, work on the synthesis of organic semiconductors was first reported early in 1828, when Wöhler synthesized organic materials artificially (chemically) from inorganic compounds. At that time, these organic materials were known to be electrically insulating and since have been used primarily for encapsulation in the electronics industry.

In 1963, for the first time, conductivity was reported using iodine doped polypyrrol [37]. Later in 1977, high conductivity in chemically doped polyacetylene was reported and gave a new direction to researchers: conduction and the conduction mechanism in organic materials. Since then, researchers have explored and synthesized different organic materials, and have reported high conductivity and their use in the electronics industry.

This chapter presents a brief overview of organic semiconductor materials, devices and fabrication technologies.

2.1 Organic Semiconductors

Organic materials exhibiting semiconductor properties are known as organic semiconductor materials. These materials consist mainly of carbon and hydrogen atoms and can be classified into two basic categories: polymers and small-molecules (oligomers). The classification of organic semiconductor materials is based on the length of the carbon chain in the backbone molecule, that is, the number of carbon atoms present in the backbone of the organic semiconductor molecule.

Each carbon atom in an organic semiconductor molecule is linked to the adjacent carbon atom, forming a chain consisting of alternating single (σ only) and double (σ and π) bonds. This alternating single and double bond arrangement is named conjugation. Conjugation in organic semiconductor materials leads to two important properties:

- Band gap formation
- Splitting of energy levels in the range of organic semiconductors with delocalized charges

In an organic molecule, the carbon atoms are sp^2 hybridized. The three sp^2 -electrons form a covalent bond via σ molecular orbitals to the adjacent carbon atoms on either side of the chain and to the side groups (such as hydrogen atoms). The remaining electrons in the p_z orbital are covalently bonded via the π -molecular orbital, with the neighboring carbon atom on only one side. The electrons in the σ -bond are strong, have large binding energy and are localized, whereas the π -bonds are weak. The electrons in the π -orbital are delocalized and spread over the entire backbone of the organic semiconductor molecule.

The interaction of the p_z orbital of the two carbon atoms in a chain results in splitting the resultant and formation of two energy levels: The Highest Occupied Molecular Orbital (HOMO) and Lowest Unoccupied Molecular Orbital (LUMO). For simplicity and for understanding, HOMO and LUMO energy levels in organic semiconductors can be thought of as analogous to the edges of the conduction band and valence band in an inorganic semiconductor. The energy diagram of the interaction of two carbon atoms is shown in Figure 2.1. In figure 2.1 of the four electrons, two from each carbon atom fill the non-bonding orbital (nb), which is available for bonding to the rest of the chain. The interaction further results in a split sigma molecular orbital (σ_+ and σ_-) and a π molecular orbital (π and π^*).

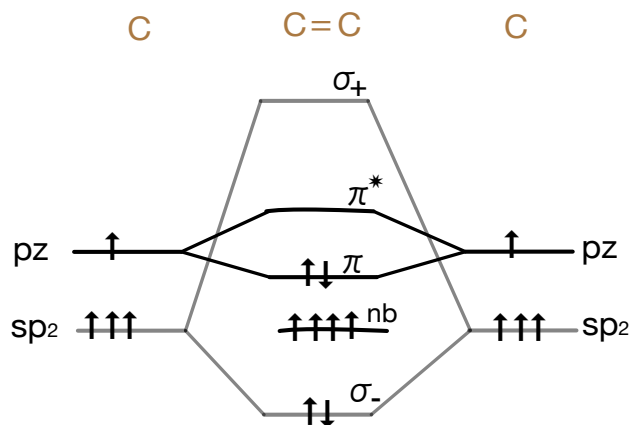


Figure 2.1 Energy Diagram of two carbon atoms with sp^2 and p_z orbital forming a non-bonding orbital, σ and π molecular orbital. The electrons in the orbital are filled according to Hund's rules for spins. The interaction of two carbon atoms ($c=c$) results in splitting of the p_z orbital in to π and π^* molecular orbitals [38]

In the case of organic semiconductors, the energy difference between σ and σ_+ is greater than 3.5 eV, whereas the energy difference between π and π^* molecular orbitals is approximately in the range of 1.5 to 3.5 eV, meaning that excitation of electrons from (σ and σ_+) requires large amounts of energy. The π to π^* molecular orbitals have a smaller energy difference in-between, so the excitation of electrons from π to π^* requires low energy and is easily possible. The energy difference between the π and π^* molecular orbitals is dependent on the degree of conjugation present in the molecule. The greater the conjugation, the smaller the energy difference will be [39]. For example, following Figure 2.2, with an increase in conjugation, the energy difference between the two energy levels is significantly reduced compared to ethylene, which has only one double bond.

The energy difference of 1.5 eV to 3.5 eV corresponds to photon energy in the visible range of the electromagnetic spectrum. The electron transition from π to π^* molecular orbitals results in absorption of visible light or emission in the visible range when an electron loses its energy and returns to normal state (π). The absorption and emission of light in a viable range is useful in many optoelectronic applications.

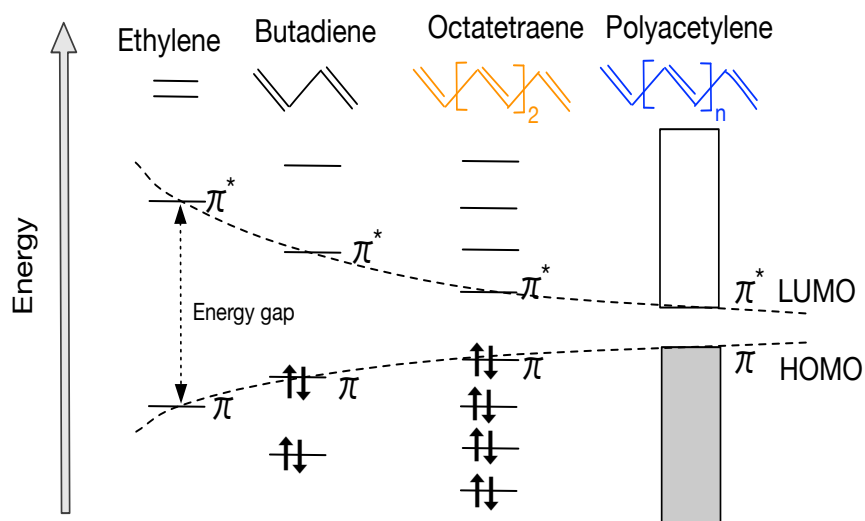


Figure 2.2 Schematic representation of the energy gap of Ethylene, Butadiene, Octatetraene and Polyacetylene, showing the energy band gap reduction with increased conjugation

2.1.1 Organic Semiconductor Materials

Organic semiconductor materials are mechanically soft. In organic semiconductor solids, the molecules are bounded via Van der Waals bonds, which are weak with less interaction between the

molecules. This weak intermolecular interaction results in amorphous solids (disordered), with no long-range molecular arrangement, in contrast to inorganic materials.

The amorphous nature of organic semiconductors makes the organic semiconductor films mechanically soft and flexible. These thin films can be deposited at low temperature, generally in the range of less than 150°C. This low temperature processability of organic semiconductor materials is useful for high throughput technologies such as printing spray coating [40], [41].

The organic semiconductor materials are classified in two main categories:

- Polymers
- Small-molecules.

The electronics and optoelectronic properties (mainly charge transport mechanisms) of both polymers and small-molecules are similar. The main difference between them is due to the length of the carbon chain in a molecule, and the side groups. These side groups alter the optoelectronic properties of the materials and also improve stability. Organic polymers hypothetically have infinite length carbon chains in their molecular backbones, whereas small-molecule organic materials have limited-length chains.

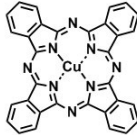
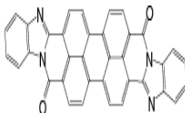
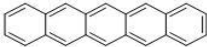
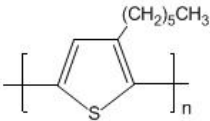
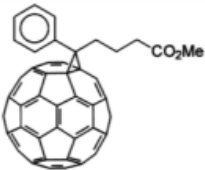
Organic semiconductor polymers are soluble and can be dissolved in an organic solvent. Polymer thin film can be processed using solution-processing techniques such as spin coating or printing. The structural properties of polymer thin films depend on the deposition techniques and the choice of solvent. Small-molecule organic semiconductors are mainly insoluble and require more sophisticated deposition techniques such as vacuum thermal evaporation. Thin films of small-molecules, when deposited, have more order in their structure than polymer thin films do. Small-molecule devices show superior performance compared to polymer-based devices [42]. However, many highly efficient polymers have recently been engineered and show equivalent or even better efficiency when used to fabricate devices.

Organic semiconductors in their neutral states are intrinsic with very poor conductivity. Increase the conductivity requires doping, which is performed either chemically or electrochemically. The concept of doping in organic semiconductor materials is very different than in inorganic semiconductor materials. Doping results in mobile carriers that, under the influence of an electric field, facilitate conduction. Doping can result in oxidation and reduction reactions. Reduction reactions give an n-type behavior, whereas oxidation leads to p-type behaviors. Oxidation is more

dominantly seen in organic semiconductors, meaning doped organic semiconductors are mostly p-type, with holes as the majority of carriers. The type n or p is further dependent on the charge injection level with reference to metal work function. Primarily, the HOMO and LUMO level of organic semiconductor define the p or n type characteristics. For example n-type materials have characteristics of high electron affinity.

The molecular structure of a few organic semiconductor polymer and oligomers is shown in Table 2.1. These organic material presented are mainly used in the work presented in this thesis.

Table 2.1 Example of organic semiconductor materials, molecular structure and HOMO, LUMO energy level with reference to vacuum

	Type	Material	Molecular Structure	HOMO	LUMO
Small-Molecule	p-Type	Copper Phthalocyanine (CuPc)		5.2 eV	3.5 eV
	n-Type	3,4,9,10 perylene-tetracarboxylic bisbenzimidazole (PTCBI)		6.1 eV	5.2 eV
	p-Type	Pentacene		5 eV	3 eV
Polymers	p-type	Poly (3- hexylthiophene-2, 5- diyl) (P3HT)		4.9 eV	2.7 eV
	n-Type	6,6-phenyl-C61- butyric acid methyl ester (PCBM)		5.37 eV	3.15 eV

2.2 Organic Semiconductor Photodetector

Like inorganic semiconductor photodetectors, organic semiconductor photodetectors are sensors whose output current or voltage varies in response to an incident light input. The basic mechanism of detection by organic photodetectors is similar to that of an organic photovoltaic device. However, to facilitate photo-generated charge collection, an external voltage is applied across the detector input. This external voltage enhances the electric field inside the device, which improve carrier generation and or collection. The output currents, not the power are the main interest in an organic photodetector.

Organic semiconductor photodetectors can be classified as:

- Photodiodes
- Photoconductors
- Phototransistors

Photodiode and photoconductors are both two terminal devices, and phototransistors have an addition third terminal named the gate terminal.

In a phototransistor, the channel current is modulated as a result of gate bias and or the incident light. Photodiodes and photoconductors can have a vertical design or a lateral one. For a vertical design, the active semiconductor material is sandwiched between two metal contacts, and the device is fabricated vertically. The lateral designs have in-plane electrodes either on the top of the semiconductor layer or on the bottom.

Vertical detector designs are very similar to organic photovoltaic designs. These designs have been extensively studied and optimized to achieve low dark-currents and fast collection. However, a few challenges remains, such as a higher dark-current than in inorganic semiconductor devices and the requirement that one of the electrodes be transparent. The other, less-studies lateral design has been examined mainly to clarify the generation and transport in the photoactive medium. In a lateral design, the inter-electrode spacing is in the range of μm as compared to nm in the case of vertical design. Thus the detector bandwidth is low.

In a photodiode detector, the detectors are operated in reverse bias, where the dark current is low and the ratio of photo to dark current is at maximum. In an ideal situation, a single photon generates an electron hole pair then contributes to the photocurrent Thus, ideally the EQE of these photodiodes

cannot be greater than 100%, whereas the EQE of photoconductors can be greater than 100% when an injecting contact is used.

Figure 2.3 represents the structure and the basic operational mechanism of an organic semiconductor photodetector

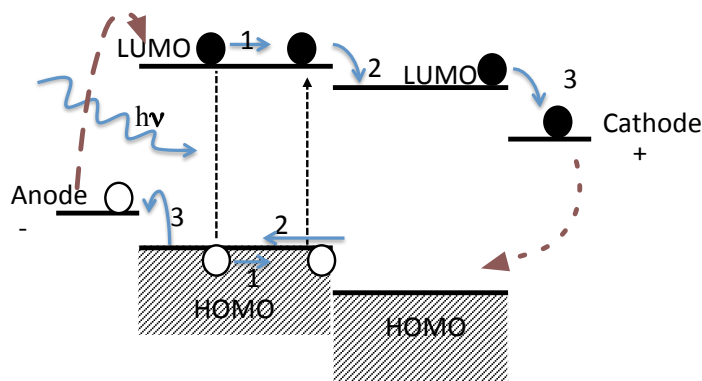


Figure 2.3 Detection mechanism in a lateral organic semiconductor heterojunction

For organic semiconductor photodetectors, the detection principle is to increase conduction under illumination. The detector mechanism can be divided into the following steps:

- Exciton formation: when a photon is absorbed in an organic semiconductor, a bonded electron hole pair (exciton) is formed.
- Separation of electrons and holes
- Charge transport and charge collection at the electrodes
- Injection of charges, which generates dark current
- Charge recombination (losses)

2.2.1 Dark Current (Charge Injection)

Dark current in a photodetector is due to carrier injection (both holes and electrons) and thermal generation. In the case of organic semiconductor photodetectors dark current is generally the result of charge carrier injection. The injection of carriers happens at the interface, where the charges overcome the injection barrier, i.e., the energy difference between the Fermi-level and the HOMO (or LUMO)

energy level of the organic semiconductor. The injection can be through either one or more of the following modes.

- Field-assisted thermionic injection. The carriers from the metal contacts are thermally excited to overcome the resultant potential barrier due to the superposition of the image charge potential and external electric field
- Tunneling of carriers from the metal electrodes to the organic semiconductor. The tunneling mechanism is explained by the Fowler Nordheim (FN) tunneling mode
- Hopping of charges from the metal Fermi level into the localized organic semiconductor, as with the thermo-activated hopping injection model

In all the above mechanisms, the charge injection is dominated by the interface properties. These interface properties have been extensively studied and engineered to improve organic device performance [39].

The dark current performance of organic semiconductor sensors can be improved with the addition of charge blocking layers between the metal-organic interfaces or with the selection of the right work function metal. The choice of stable good conducting materials is limited. The blocking layers are of organic or inorganic semiconductor materials selected based on the HOMO and LUMO levels. The blocking layer limits injection of one kind of carrier when it facilitates the collection of the other kind. Therefore, the blocking layer can act as hole blocking to electron blocking.

2.2.2 Charge Transport

Organic materials exhibit semiconductor properties due to the presence of a conjugated system in their molecular backbone carbon chain. The p_z orbital interaction of sp^2 hybridized atoms in an organic molecule or chain results in a system of π -bonds. The π -bonds are relatively weak with low binding energies. Therefore, the electrons in π -bonds are loosely bounded and delocalized inside the molecule. These π -electrons are largely responsible for the electro-optical properties of the organic semiconductor materials [43].

Organic semiconductor solids are amorphous, disordered structures. These materials have strong electron-phonon coupling, with charges localized on a single organic molecule. The amorphous nature of organic semiconductors results in conjugated segments of different lengths. Due to the different lengths, the resulting interaction energies cannot be well defined into two discrete energy

levels. Instead, the resulting energy levels are an approximation of a Gaussian function, as shown in Figure 2.4. The Gaussian function approximation is based on the observed shape of the absorption spectrum, which is Gaussian [44].

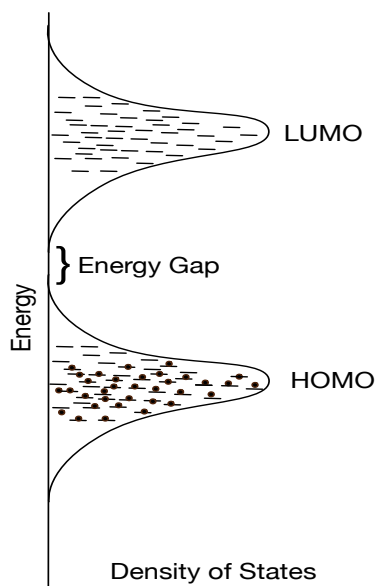


Figure 2.4 LUMO and HOMO Energy level, Gaussian function approximation

The charge transport in organic semiconductor solids can be explained using microscopic and macroscopic approaches. The microscopically approach consider that the carrier (polarons) hopping between the two molecules is a result of thermactivated lattice vibrations. The charge hopping in between the molecules can be localized by defects, or potential wells. L.D. Landau proposed one hopping model explanation. Second approach is treat organic semiconductors as a assembly of disordered hopping sites in which the carrier can drift under the influence of an external electric field. The Poole Frenkel model is used to explain the electric field dependence of charge carrier drift mobility [38].

2.2.3 Hopping Transport

Hopping transport is typically the main conduction mechanism for charge transport in organic semiconductors (disordered materials). Hopping transport is the phonon assisted tunneling of a charge carrier from an occupied localized state to a nearby unoccupied localized state [45] [46]. Hopping

transport takes place near The Fermi level. Miller and Abrams' hopping model describes the transition rate (W_{ij}) from an occupied state i with an energy ε_i to an unoccupied state j with an energy ε_j [47]. Miller and Abrams' model is based on the assumption, that single phonon jump form site to site at a low rate of doping, as described by the following equation:

$$W_{ij} = \nu_0 \exp(-2\gamma R_{ij}) \begin{cases} \text{Exp} \left[-\frac{(\varepsilon_i - \varepsilon_j)}{K_B T} \right] & \varepsilon_i < \varepsilon_j \\ 1 & \varepsilon_i > \varepsilon_j \end{cases} \quad (2.1)$$

where ν_0 is the attempt-to-jump rate (a pre-factor), γ is the inverse localization length, T is the absolute temperature, K_B is the Boltzmann constant, and R_{ij} is the distance between two states. The first exponential gives the tunneling probability between each state, which is determined by the special distance between the two states. The second exponential shows the temperature dependence of the tunneling state when an energy barrier is present. This model is applied with the assumption that the conjugated segments act as isolated localized states. Thus, the presence of phonons will aid the charge carriers to overcome the energy barrier between the two states. This phenomenon can be observed with the decrease in carrier mobility with a decrease in temperature.

Miller and Abrams' hopping model has been further extended into the Variable Range Hopping (VRH) model, makes the assumption that the localized states are spread over the entire energy gap.

2.2.4 Excitons (Photogeneration)

When an organic semiconductor is optically excited, a localized electron and hole pair is generated. Due to the strong localization of the occupied and unoccupied states in organic semiconductor materials, the Photo-generated electron and hole stay localized on a single molecule. The localized electron-hole pair is known as an exciton.

The three types of excitons that can be formed in bulk material are as follows:

- Frenkel excitons
- Wannier-Mott excitons
- Charge transfer excitons or excimer excitons

Organic semiconductors due to localized states, have much shorter radi and high binding energy than the inorganic ones.

Frenkel excitons have smaller radii of about 5 Å, and are located on molecules. In the case of organic semiconductors, Frenkel electron-hole pairs have strong coulombic interaction due to the absence of strong dipoles. The binding energy of a Frenkel exciton is approximately equal to 1eV.

Wannier-Mott excitons are mostly found in inorganic materials. A Wannier-Mott exciton has a separate electron and hole, and radius of around 10 Å. Wannier excitons have efficient coulombic screening and are not created on the same single molecule. Typically, the binding energy of Wannier exciton is around 0.1eV.

Self-trap excitons, charge transfer excitons or excimer excitons are formed due to the presence of deep traps in the material or a molecular deformation. Excimer excitons are created when the charge transfer time of an exciton is greater than the time of molecular lattice deformation. In charge transfer exciton, the holes and electrons are present on adjacent molecules.

The three excitons are represented in Figure 2.5.

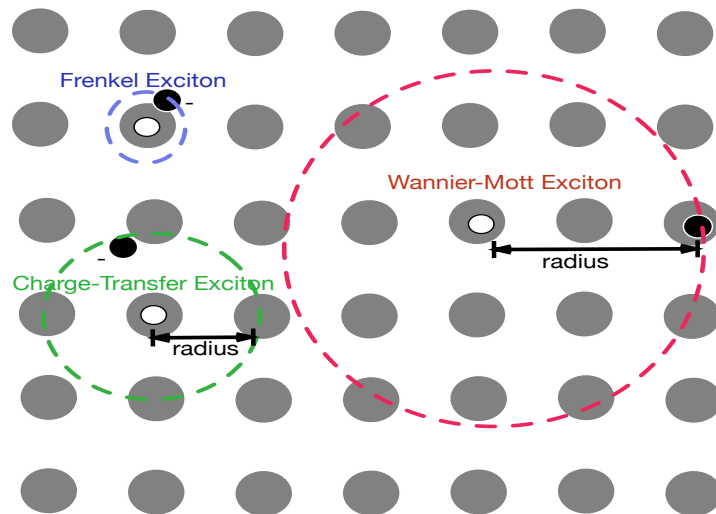


Figure 2.5 Schematic representation of the various types of excitons in semiconductors and insulators. Frenkel exciton (Blue) is small radius. Large radius (Red), Wannier-Mott exciton commonly found in inorganic semiconductor materials. Intermediate radius (green) charge transfer (CT) exciton [48]

The exciton diffusion in an organic bulk is a thermally activated hopping process that can be described by one of three mechanisms: Cascade energy transfer, Förster energy transfer, Dexter energy transfer.

2.3 Organic Semiconductor Large-area Digital Imagers

A digital imaging detector is an array of pixels in a two-dimensional arrangement with readout electronics. Each pixel in an imager has a photodetector and TFT circuit (switching, amplification). An organic semiconductor digital imager has an organic photodetector (OPD) integrated to the readout Thin Film Transistor (TFT) circuit. Imagers can be classified into two main categories: passive matrix and active matrix.

A passive matrix is a simple assembly of cross bar OPD arrays. The architecture is very simple but is prone to many readout issues such as inter pixel cross talk. Active matrix imagers are the most used in digital imaging. In an active matrix imager, each pixel has an OPD integrated with a TFT. The active matrix imagers are further categorized as passive pixel and active pixel active matrix.

The passive pixel model (figure 2.7) is a simpler design where an OPD is integrated with a single readout switch TFT. The linearity of the output is thus highly dependent on the detector's linearity. The passive pixel design experiences high electronic noise, and its readout time depends on the on-pixel capacitance and transistor's on-resistance. For the passive pixel design given in figure 2.7, the TFT is the readout switch with an ON resistance typically in the Mega-ohms for amorphous semiconductors. Taken together with the capacitance of the detector element (i.e. the OPD capacitance), the readout speed of the PPS pixel can be determined to be around 5 to 10 RC time constants.

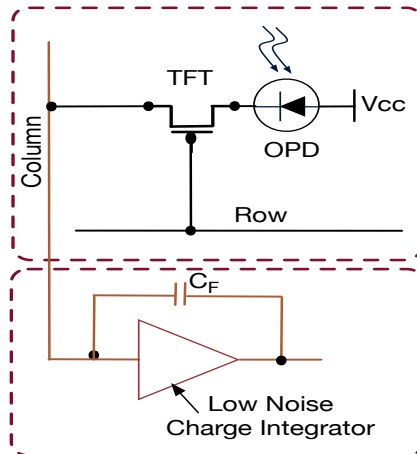


Figure 2.6 An passive pixel design.

Active pixel design (Figure 2.7) has a on-pixel amplifier built in for on-pixel amplification. This design has the advantage of low noise and reduced external readout circuitry. The active pixel design can be current programmed or voltage programmed. Several other designs such as hybrid active pixel design, and RVCO pixels, have also been reported in literature [49].

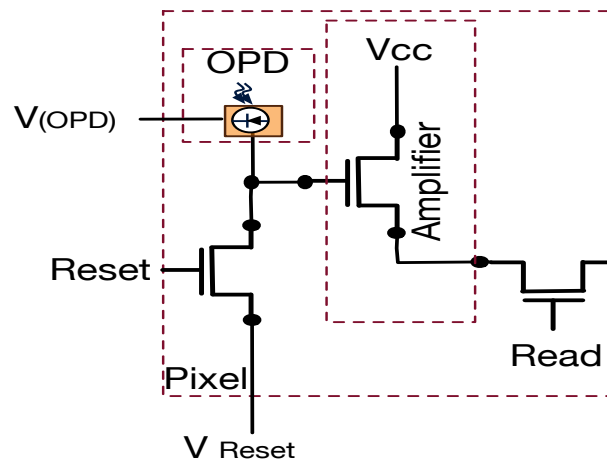


Figure 2.7 An active pixel design using three transistors

Using an organic semiconductor photodetector, both active pixel and passive pixel designs appear in the literature [25] [50] [28].

2.4 Organic Semiconductor Fabrication

Organic semiconductor devices are fabricated at low temperatures. The fabrication technique for organic semiconductor devices can be broadly categorized into two main classes:

- Vacuum Thermal Sublimation
- Solution Processing

The Processing techniques are adapted dependent on the type of organic semiconductor materials. Small-molecule organic semiconductors are difficult to dissolve in a solvent however they can be sublime when heated. Therefore, thin films of small-molecule materials are deposited using a thermal sublimation process. The films of these materials are deposited under high vacuum, which is generally in the range of 10^{-6} or above. High vacuum deposition avoids the presence of oxygen, moisture and any other contaminations that could react with and degrade the organic material films. Thickness monitors (crystal oscillators) are used to read-out the film thickness. The organic material holder is heated using direct current (DC) power. Sublimed material gets deposited on the substrate placed above the sources, with or without a shadow mask. The temperature of the substrate temperature is about room temperature. Substrate heaters can be used to control the substrate temperate during thin film deposition.

Figure 2.7 shows a block diagram of the vacuum thermal-evaporation system. The two chambers are shown: an upper one where the sample is placed and a lower main chamber where the heating sources, thickness monitor sensor, and shutter are present. A gate lock separates the two chambers. The two-chamber system allows loading of material without breaking the vacuum at the device side.

The rate of deposition of organic semiconductor material is dependent on the amount of DC power applied by to the heating sources. Normally, low deposition rates are set to have a uniform film with low surface roughness [51], [45].

In the case of an organic semiconductor polymer, the polymer material can be dissolved in a solvent. A film of polymers can processed using solution processing techniques such as spin coating, inkjet printing, etc. The processed film's quality depends on many parameters. For example in the case of spin coating, the spin speed is important, in addition to the solvent wetting properties and viscosity of the solution [51] [45].

Although solution processing is a simpler technique than vacuum thermal evaporation, with vacuum thermal evaporation, the films' thickness and morphology can be more easily controlled [39]. This is one of the reasons that the small-molecule devices show better performance than the polymers.

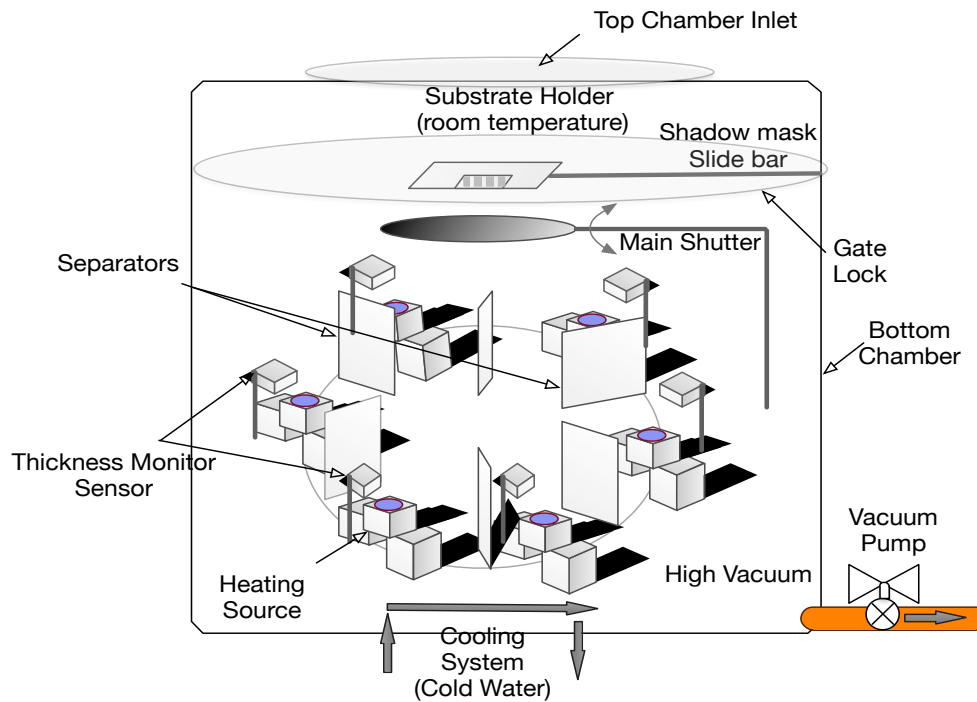


Figure 2.8 Block diagram representation of a thermal evaporator system

Chapter 3

Flexible X-ray Imager

This chapter presents a large area X-ray imager using that uses organic semiconductor technology. A vertical organic semiconductor photodetector is integrated into an organic semiconductor thin film transistor's backplane to form a large area imager for X-ray radiology. The fabricated imager is mechanically flexible and solution processed, except the metal layers.

The chapter also demonstrates the use of low-cost organic semiconductor technology to fabricate large-area X-ray imagers for future modalities in medical imaging. This work has been conducted at HOLST Center, Eindhoven, The Netherlands. The article is included under Elsevier Ref License number 3282881222389.

3.1 Introduction

Large area imagers, in particular imagers for medical X-ray imaging are based on flat panel a-Si technology. Flat panel digital imagers in X-ray imaging has shown considerable improvement in the quality of extracted images in comparison to the traditional analog detectors. Further, the image extracted from flat panel digital imagers is in the form of digital data, which can be processed using computational techniques, and image-processing algorithms can be applied to extract information and to enhance image quality. Digital medical-imaging technology promises reduced doses of harmful X-ray, as well as improved image quality. At present the large-area industry uses a-Si technology to produce these panels, which requires high processing temperatures, generally in the range of 300°C. Specialized substrates that can sustain temperature above 300°C are needed to fabricate better a-Si devices. At present highly temperature-resistant glass substrates are most commonly used by the industry [52], but the use of glass substrate adds a considerable weight and also makes the panels structurally fragile, and consequently sensitive to minor mishandling and not portable. In order to make these detectors robust and portable an additional mechanical assembly is used. Other than the heavy and fragile nature of these flat panel X-ray detectors, patients going through an intraoral radiology scans consider the process uncomfortable.

Making the detectors curved and flexible can significantly improve the comfort level of patients being scanned. To do so, the glass substrate must be replaced with a flexible and mechanically strong plastic substrate, one that can withstand the a-Si processing conditions (temperatures above 300°C).

Low cost plastic cannot withstand such high temperatures, and so cannot be used as a substrate material.

Organic semiconductor technology is one low cost alternative to a-Si technology. Organic semiconductor devices can easily be fabricated at low temperatures (less than 150°C). Simple and bulk production large-area fabrication techniques such as printing or spray coating, etc., are used to fabricate organic semiconductor devices. Organic devices (backplane using organic TFTs) fabricated on a plastic substrate make the overall structure flexible, and more important, lightweight. These organic detectors can be coupled to an X-ray phosphor screen, which is flexible and can be used for X-ray imaging. Currently, flexible imager technology does not exist, but is an area of active research interest.

To demonstrate a flexible lightweight X-ray imager, we have monolithically integrated a vertical organic photodiode with an organic TFT in an array to form an imager with a pixel density of 127ppi. Both the organic photodetector and the TFTs are solution processed (except the metal). For high-volume low-cost production, solution processing is the preferred low-cost technology. Organic imagers are processed on a low-cost plastic substrate, i.e., Polyethylene Naphthalate (PEN) foil of 25 μm thickness coupled with a 300 μm thick scintillator. The overall thickness of the imager is under 500 μm , including the encapsulation barrier layers.

3.2 Experiment

The backplanes used in the integration have been acquired from HOLST and are characterized for uniformity, solvent compatibility and electrical characteristics. These backplanes use a 25 μm thick freestanding foil supplied by DuPont Teijin Films as a starting substrate. The foil is laminated on a silicon carrier to provide a rigid support that is easy to handle, and making it possible to use standard off-the-shelf fabrication tools such as spin-coaters and photolithography tools for further cost savings. Once all the processing steps are performed, the foil can be easily delaminated from the carrier without altering the TFT or OPD performance. The Silicon carrier can later be reused. Polyethylene Naphthalate (PEN) is chosen as the substrate material. The crystalline form of PEN foil is highly resistant to chemicals and can easily withstand temperatures below 200°C.

Each detector array has 32 rows and 32 columns, with pixel sizes of 1x1 mm² and 200x200 μm^2 , respectively. Figure 3.1 shows the array layout.

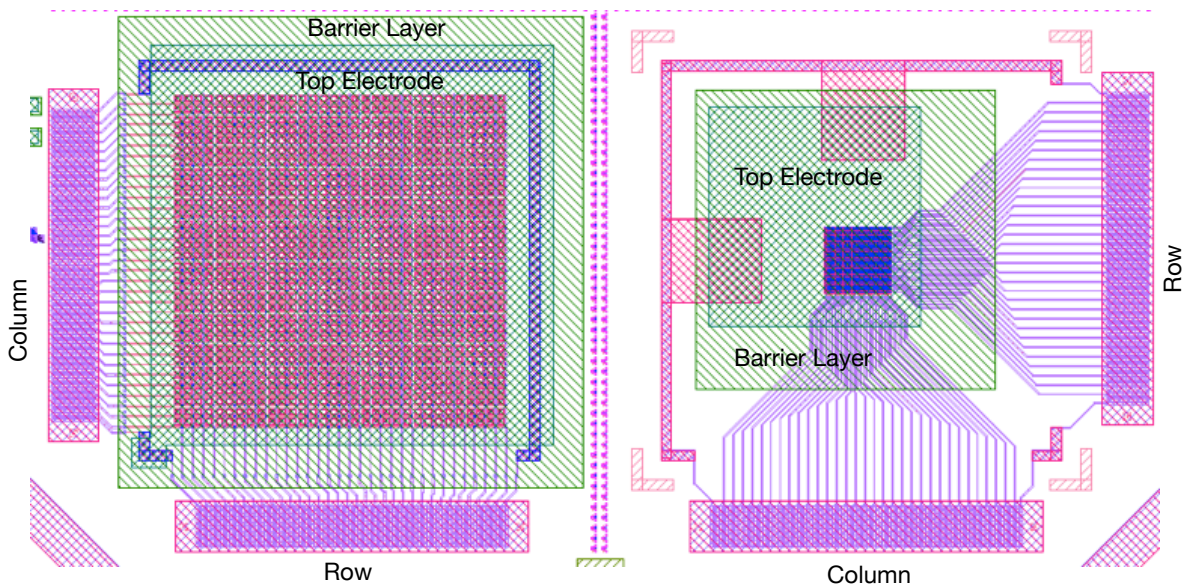


Figure 3.1 Design lay out of 32-row and 32-column array, with $1 \times 1 \text{ mm}^2$ pixel size (left) and $200 \times 200 \text{ }\mu\text{m}^2$ pixel size (right).

Figure 3.2 displays a cross-section of the pixel array layout. Each pixel has a bottom gate TFT with a channel length of $5 \text{ }\mu\text{m}$ and channel width of 140 and $70 \text{ }\mu\text{m}$. The large pixels (area, $1 \times 1 \text{ mm}^2$) have a $140 \text{ }\mu\text{m}$ channel length TFT, and the small pixels (area, $200 \times 200 \text{ }\mu\text{m}^2$) consist of 70 nm wide channel TFTs. Different channel widths are chosen such that the TFTs do not limit the OPD currents, particularly at higher light intensities.

Organic TFT consists of pentacene as the active channel material. The soluble precursor of pentacene is used and spin coated. When heated it converted into polycrystalline thin film of functional pentacene [4]. Polycrystalline pentacene film is 50 nm thick, and is patterned using RIE to reduce electronic cross talk between adjacent OTFTs. SU-8 insulator material is used as a gate dielectric (350 nm thick). The TFTs are covered with a protective interlayer dielectric (SU-8) of $1.7 \text{ }\mu\text{m}$ thicknesses. The interlayer is used to passivity pentacene the sidewalls and cover the edges of the pixel anode. The Anode's pixel window opening is made at the interlayer dielectric above the Gold(Au) pixel pad, which defines the area of the photodiode.

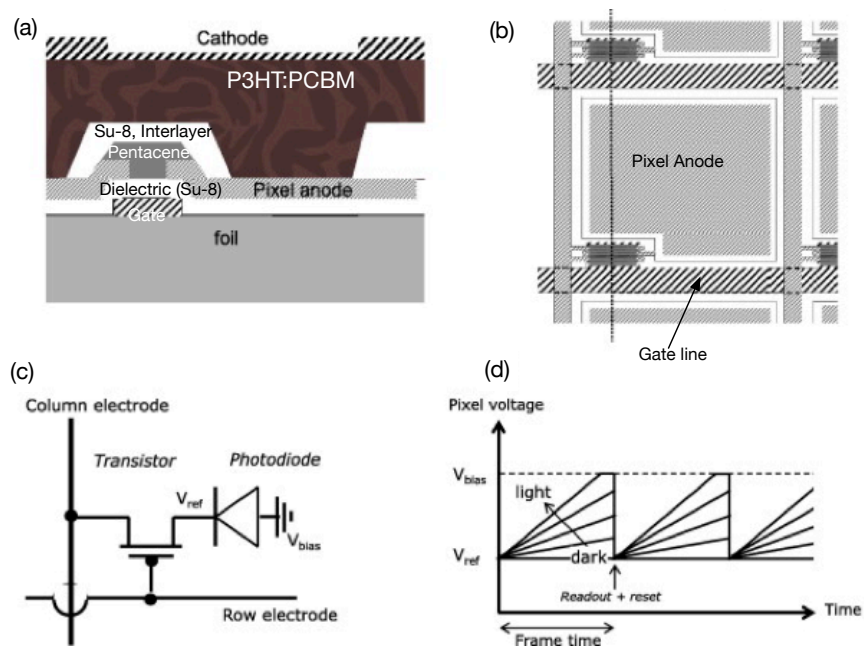


Figure 3.2 Cross section of pixel (a), and top view (b). Schematic circuit representing a single pixel with integrated OTFT and OPD (c). Voltage on a pixel node versus time for different light intensities, during one frame time (d).

Integration of OPD with the OTFT backplane involves a series of solution-processing steps. To verify the effect of solvents on the OTFT performance, solvent compatibility tests are performed. Water and dichlorobenzene are the two main solvents used. The OTFT output characteristics are measured before and after applying solvent. As a first step, the TFTs are immersed in DI water and heated up to 100°C several times. The OTFT output characteristics are recorded before and after. Next the OTFTs are tested with dichlorobenzene at a temperature of 140°C, and output characteristics before and after are measured. Important OTFT parameters such as gate-current, voltage-dependent drain current at gate bias and threshold voltage are measures. Figure 3.3 and figure 3.4 shows the OTFT characteristics curves before and after solvent compatibility tests. No degradation occurs in the OTFT performance, and so it can be concluded that solvents do not degrade the OTFT performance and can be safely used in the solution process for the other layer above it.

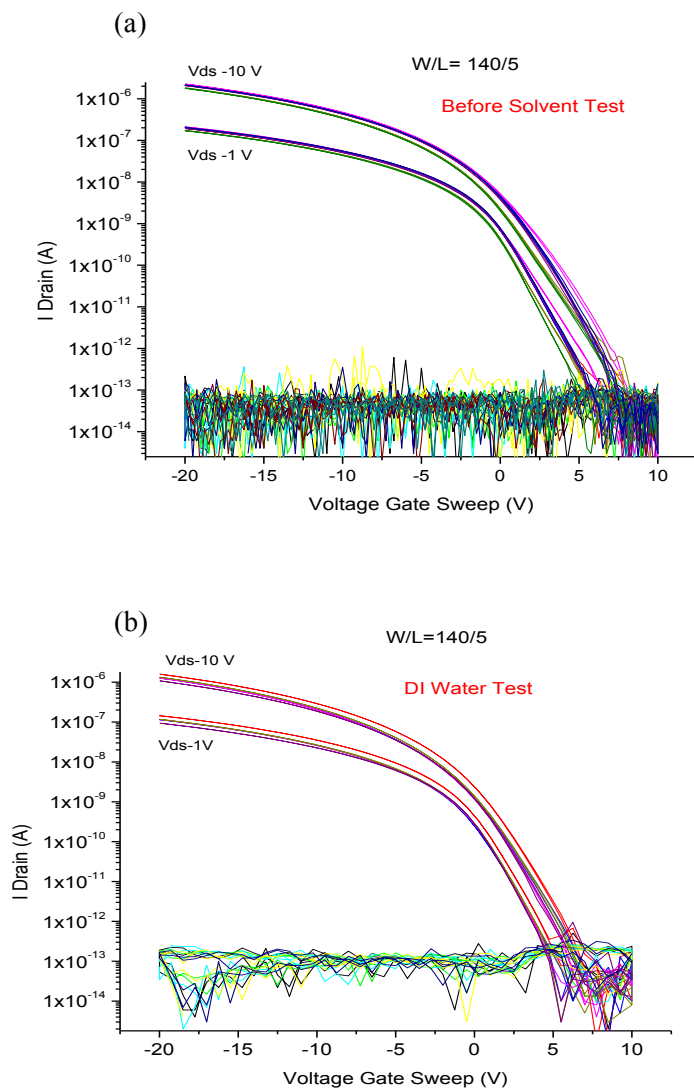


Figure 3.3 Effect of Water on the backplane OTFTs: Plot of gate voltage vs. drain current at drain source voltage of -10V and -1V, before (a) and after (b)

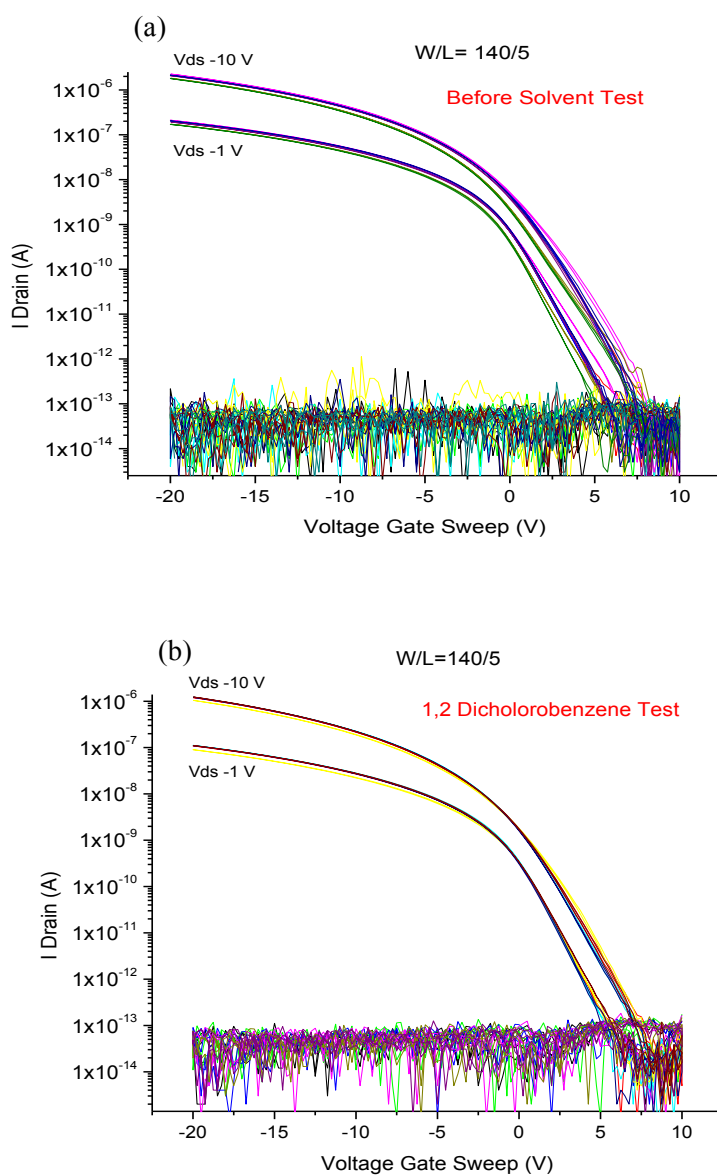


Figure 3.4 Effect of Dichlorobenzene on the backplane OTFTs: Plot of gate voltage vs. drain current at drain source voltage of -10V and -1V, before (a) and after (b).

The organic semiconductor active layer consists of a blend of poly(3-hexylthiophene)(P3HT) and [6,6]-Phenyl C₆₁ butyric acid methyl ester (PCBM). Thin films of P3HT:PCBM are solution processable and show promising light sensitivity and high responsivity in the green wavelength [53], [54] [55], making them suitable for integration with a popular scintillator (CsI:TI) for indirect X-ray detection.

Vertical organic photodiode geometry is used and a multilayer design is implemented above the pixel OTFT anode. Multilayer layer OPD is shown in Figure 3.5.

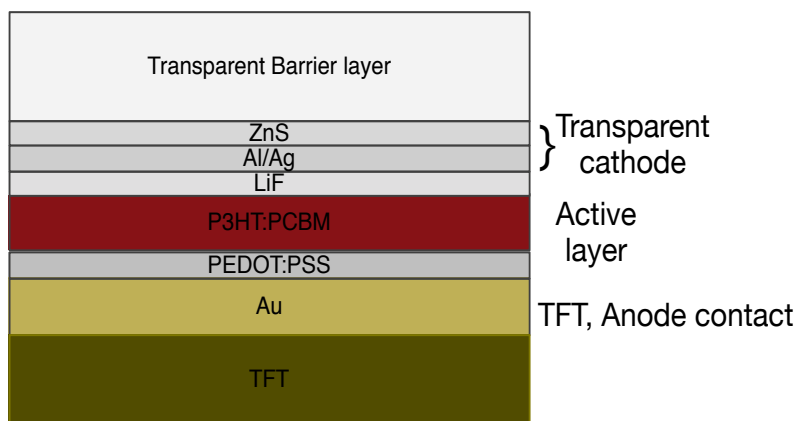


Figure 3.5 Cross-sectional layout OPD on TFT anode, including transparent cathode stack and barrier layer

A 20-30 nm thick layer of a low conductive undiluted aqueous suspension of poly(3,4-ethylenedioxythiophene) poly(styrenesulfonate) (PEDOT:PSS), (Baytron CH-8000) from the HC Stack is inkjet printed above the pixelated anode. The printed layer is annealed for 30 min at 200 °C in a vacuum. Next, a thin film of P3HT:PCBM is deposited. A 50% weight solution of P3HT and PCBM is first dissolved in dichlorobenzene (ratio 1:1). The solution is stirred overnight at 75°C, the filtered and spin coated above PEDOT:PSS to obtain a bulk heterojunction layer of 450 nm thickness. After deposition, the samples are, annealed for 5 min at 140 °C in nitrogen. Next to the heterojunction layer, a thin layer of 0.5 nm LiF is thermally evaporated. The top contact is defined using a stack made of thermally evaporated 2 nm Aluminum (Al), 10 nm silver (Ag) and 30 nm of ZnS. The top contact is semitransparent for the X-ray scintillator emission wavelength. The addition of a 30nm ZnS layer improves the light coupling, in particular at the 530 nm wavelength with an effective transmission of 76%.

Oxygen and moisture are the two key factors involved in the degradation of organic semiconductor materials; therefore the OPDs are encapsulated using a thick barrier layer on the top above the cathode, and to limit moisture diffusion from the bottom, a 150 nm thick AlO_xN_y layer is deposited on the back side of the PEN substrate. A barrier layer previously reported and developed for OLED

technology is used in this case [56]. The barrier layer is a 20 μm thick organic printed layer sandwiched between two 100nm low-temperature plasma deposited amorphous hydrogenated silicon nitride (a-SiNx:H) layers. The barrier layer is optically transparent.

Transistor characteristics are recorded at room temperature in ambient atmosphere using an Agilent 4155B semiconductor parameter analyzer. Discrete photodiodes of different areas are characterized in terms of their dark current, sensitivity and linearity with green-emitting (525 nm) LED arrays with calibrated and uniform light output over an area of $> 10 \text{ cm}^2$. In order to investigate the behavior under X-ray illumination a scintillator was placed on top of the transparent humidity barrier covering the arrays. A Tl-doped cesium iodide (CsI:Tl) of 300 μm thickness and a mass density of about 100 mg/cm^2 was used on a fiber optic plate (FOS-HL, Hamamatsu). This scintillator has a rather broad light emission, with a maximum at about 550 nm. X-rays are produced by a medical X-ray tube (Philips SRM2250 ROT) with a tungsten anode driven by a Philips Super80CP generator. X-ray illumination is used in continuous mode with a 70 kVp high voltage and 6 mA beam current. Without any external beam filtration, the X-ray energy spectrum resembled a beam quality, which is known as RQR5 in radiology. The mean energy of X-ray quanta is about 40.0 keV. Seventy-five percent (75%) of the impinging X-ray energy was calculated to be absorbed by the scintillator layer. The dose rate at the distance of the arrays is measured with an ionization chamber dose meter (PTW Unidos). Images are recorded with a 150 msec integration time. The long integration time implies there is no significant TFT leakage in our arrays. Dynamic characterization of the array is not included here.

3.3 Results and Discussion

The electrical schematic of one sensor pixel is shown in Figure 3.2 (c). The row electrode is connected to the gate of the TFT, while the column electrode and anode of the Organic Photo Diode (OPD) are connected to its source and drain. The flat panel sensor is scanned one row at a time, in a way similar to that in active-matrix displays. The photodiode is reverse biased to $V_{\text{ref}} = -2 \text{ V}$. Figure 3.2(d) shows the voltage versus time on the pixel node between the organic photodiode and the readout TFT, for the case of several different continuous illumination levels. Photons absorbed in the Bulk Heterojunction (BHJ) layer of the diode create electron-hole pairs. The electrons and holes are separated by the electric field generated by the reverse bias on the diode and collected at the terminals. The resulting photocurrent discharges the diode capacitance and reduces the reverse bias across the diode. The voltage on the pixel node rises toward V_{bias} during the frame time. During one

frame time (t_F), all the rows are sequentially selected by applying a voltage that changes the TFTs from the non-conducting to the conducting state. In this line selection time (t_L), the readout TFT transfers the charge from the photodiode capacitance to the data line and resets the voltage across the photodiode capacitance to its original value of -2 V. The readout charge is proportional to the number of photons absorbed in the photodiode. External electronics amplify the readout charge from each pixel and multiplex the data signals from the array into a video signal, representing the 2D image.

Pentacene TFT characteristics are shown in Figure 3.6 (a). The average field-effect mobility is $0.2 \text{ cm}^2/\text{V}$ at a gate bias of -20 V. The average OFF current is $130 \pm 37 \text{ fA}$ at a gate voltage of 10 V, while the ON current is $0.3 \pm 0.09 \text{ mA}$ at a gate voltage of -20 V. The current modulation, measured between a gate bias of 10 V and -20 V, therefore exceeds 10^6 . A photograph of a fully processed TFT array on plastic is shown in Figure 3.6 (b). The initial yield of the TFTs is $\sim 99\%$, and device failure occurs mainly because of current leakage through the gate dielectric layer. A blend of regioregular poly(3-hexylthiophene) (P3HT) and [6,6]-phenyl C61 butyric acid methyl ester (PCBM) is used as a photoactive layer. When completed with a semi-transparent common cathode, the result is a top-illuminated photodiode array between the pixel pad as anode and the semi-transparent cathode. Discrete photodiodes of 12.5 mm^2 were characterized in terms of their dark current, sensitivity and linearity with a calibrated and uniform light output over an area of $>10 \text{ cm}^2$ using a green-emitting (525 nm) LED. Photocurrents as a function of illumination level at a -2 V bias are shown in Figure 3.6 (c). From the photocurrents we estimate an external quantum efficiency, EQE, of around 60%, using $\text{EQE}(\%) = 1240 \times J (\mu\text{W}/\text{cm}^2) / \lambda (\text{nm}) \times I (\text{W}/\text{m}^2)$. The photocurrent follows a power law relation (power index of 0.97) with the incident light intensity Figure 3.6 (d). This closeness to linear intensity dependence allows the incident light intensity to be represented directly by the photocurrent, with negligible deformation. The (linearly extrapolated) sensitivity of the photodiode is $\sim 0.32 \text{ A W}^{-1}$, very similar to the value of 0.33-0.39 A/W reported by Tedde et al. [24]. At a power density of $70 \text{ mW}/\text{cm}^2$, the current increases by about three orders of magnitude. The rectification ratio of the dark current at bias voltages of $\pm 2 \text{ V}$ is 7.5×10^5 . This value is comparably higher than the values of $\sim 1 \times 10^5$ and $\sim 1 \times 10^4$ reported by Ramuz et al. [27] and Baierl et al. [57] [34], respectively. Next, we investigated the performance of the P3HT-PCBM photodiodes integrated with the pentacene TFTs in the arrays on plastic. The ON-current of the TFT ($L/W = 140 \mu\text{m}/5 \mu\text{m}$) in the $1 \times 1 \text{ mm}^2$ array amounts to $0.3 \mu\text{A}$, while the OFF-current is in the fA range. The pixel current (a combination of transistor and photodiode currents) of 1024 pixels was measured in the dark and upon light exposure.

With the selected TFT switched on (gate voltage of -20 V), the average dark (or background) pixel current is 9.6 nA.

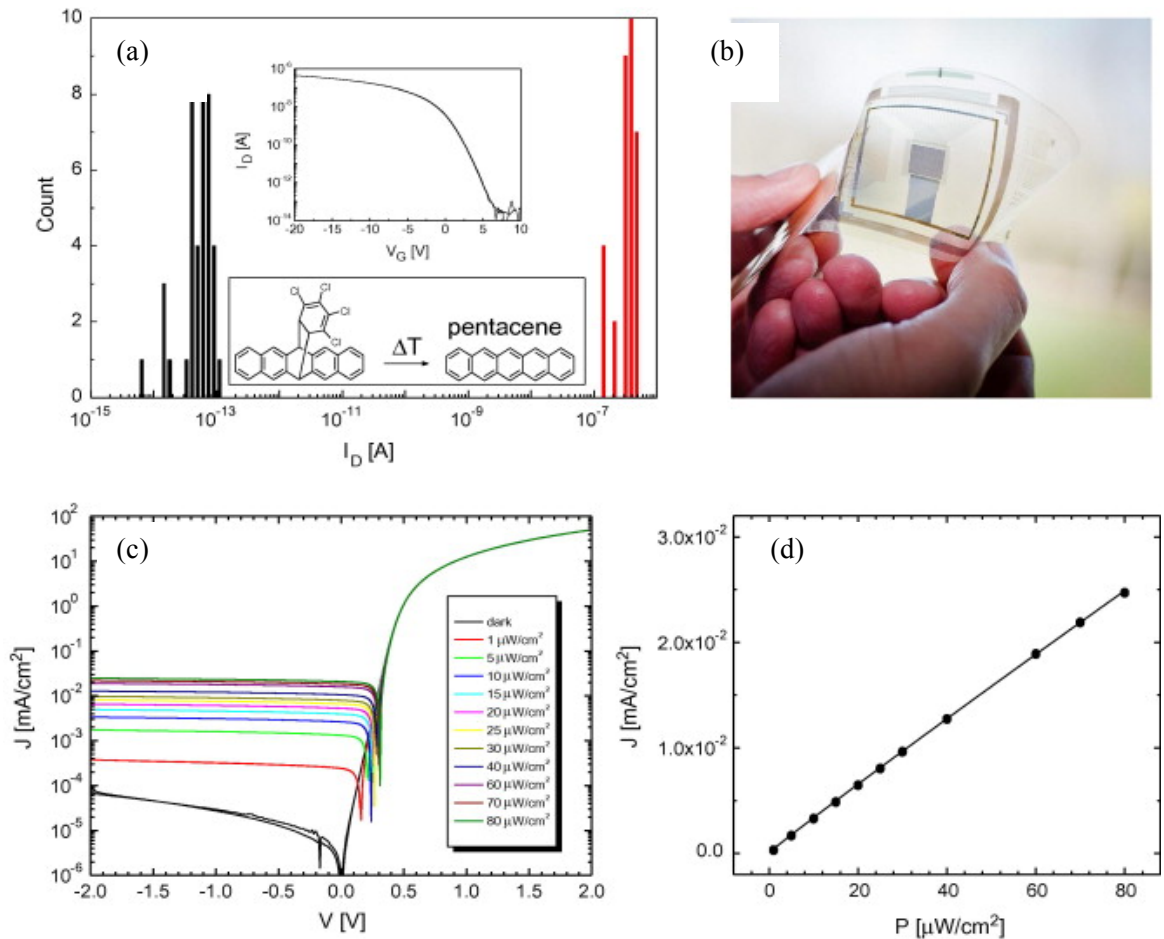


Figure 3.6 OTFT current of 40 transistors measured at +10V and -20V: OFF current (black) and ON current (red). The inset shows the transfer characteristics for a typical organic TFT fabricated with the complete image sensor process on a PEN plastic substrate, as well as the molecular structure of the precursor pentacene that is converted to pentacene by a thermal annealing step. The transistor channel length and width are 5 and 140 μm , respectively (a). Photograph of a flexible TFT array plus fan-out circuitry (b). Current–voltage characteristics of a large-area (12.5 mm²) organic photodetector in the dark and under illumination at several different intensities (incident wavelength is $\lambda = 525 \pm 3$ nm) (c). Plot of current density at -2 V vs. light intensity, plus linear fit (d).

Under ambient ‘office’ lighting conditions the pixel current increases by a factor of ~ 13 - 127 nA (Figure 3.7 (a)). As the value of 127 nA is still much lower than the current drive of the TFT, the pixel current is determined by the photodiode, also under relatively bright illumination conditions. The narrow current density distribution indicates high uniformity and follows a Gaussian shape. The derived standard deviation are 3.65 nA and 4.93 nA, for the background and photocurrent, respectively. A captured photo-image is shown in Figure 3.7 (b). The image was obtained by placing a macroscopic object, a key in this case, on top of the sensor array to cast a shadow on the photodiodes underneath. The image was captured under ambient (indoor) lighting conditions. The column electrodes are driven at -20 V during the line selection time and 10 V during the hold time. The accuracy and sensitivity of the raw image is determined mainly by the (variation in) dark current and uniformity of the photodiode characteristics. Like the discrete diodes, the integrated diodes show a close to linear sensitivity (Figure 3.8). This sensitivity allows for ambient light detection without further correction, and X-ray images at low radiation doses after dark current and gain correction.

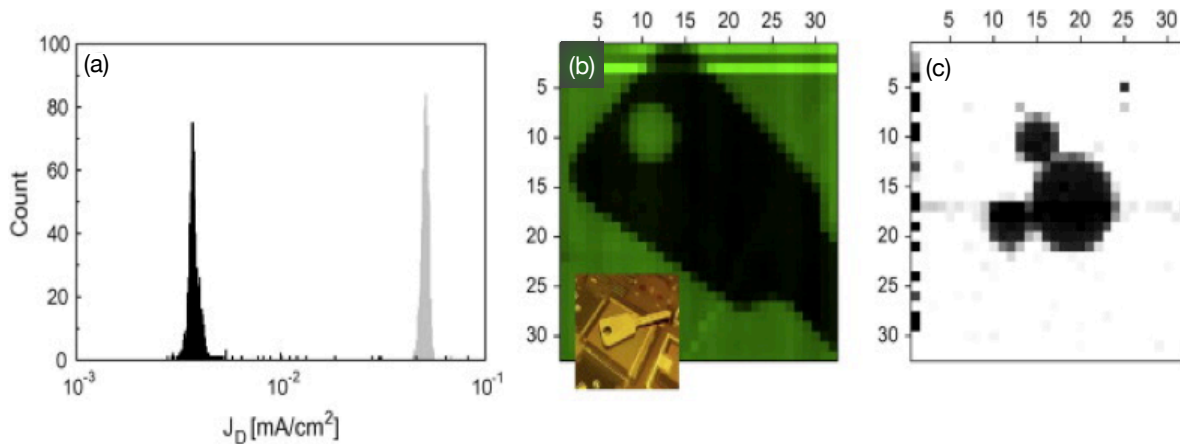


Figure 3.7 Characteristics of the 25 ppi array. (A) Histogram of background current (black) and photocurrent (grey) of 1024 pixels. (B) Recorded photo-image. A key was placed on the array (see inset). (C) X-ray image of 3 circular lead objects (with radii of 5 mm and 3 mm, respectively) recorded with a dose of 1.2 mGy s^{-1} . In all cases, the transistors were biased at a gate voltage of -20 V or $+10$ V, and the common cathode was biased at -2 V.

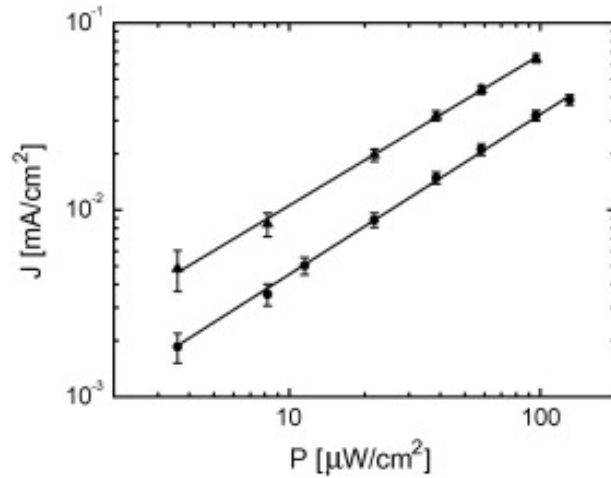


Figure 3.8 Pixel current density at -2 V as a function of light intensity for the 25 ppi (circles) and 127 ppi photodetector array (triangles). The (linear) slopes of the $1 \times 1 \text{ mm}^2$ and $200 \times 200 \mu\text{m}^2$ pixels are 0.86 and 0.81, respectively. When calculating the current density, the effective diode array is used because the TFT current is negligible.

The thin OPDs efficiently absorb visible light, whereas X-rays are weakly absorbed, similar to the case of a-Si diodes. X-ray sensitivity is therefore achieved by placing a scintillator, CsI:Tl, on the sensor array. We estimate that the spacing between the top surface of the array and the fibre optic plate with the scintillator is less than $2 \mu\text{m}$, given their low surface roughness. This implies that the optical gap between the P3HT-PCBM film and bottom surface of the scintillator is determined by the $20 \mu\text{m}$ thick top encapsulation film. The scintillator absorbs the incident X-rays and emits light centered around 550 nm that is sensed by the organic photodetector array, a principle that is well known and used in today's commercial products. Using this approach, static X-ray images were recorded using a typical radiology X-ray spectrum with a mean energy of 40 keV and with a dose rate ranging from 0.27 mGy s^{-1} to 1.2 mGy s^{-1} . Simulations of the used X-ray spectrum result in a number of 18900 X-ray photons per $\mu\text{Gy} \cdot \text{mm}^2$. Considering the known light output of the scintillator per absorbed X-ray energy of 66 photons/keV [58], an absorption of 75% of the X-rays in the scintillator, and an estimated optical coupling loss factor of 0.7 , it was calculated that the photodiodes were exposed to a light intensity of $1.1 \mu\text{W cm}^{-2}$ at a dose rate of 1.2 mGy s^{-1} . The image is corrected for the dark background and the gain differences among the pixels. The image in Figure 3.7(c) is shown without any spatial filter correction for line and pixel defects. It depicts three circular lead discs that were placed on top of the scintillator screen.

Figure 3.9 shows an X-ray image of a lead object with slits of different widths that fully covered the array. Aside from demonstrating good imaging properties, the image contains relatively few defects, indicating that the fabrication process is reasonably robust. After extended X-ray exposure doses, the dark photocurrent was measured again. No significant changes were observed (Figure 3.10), illustrating that the organic semiconductors are not significantly affected by exposure to 0.5 Gy, in line with previous X-ray degradation studies. [59], [60].

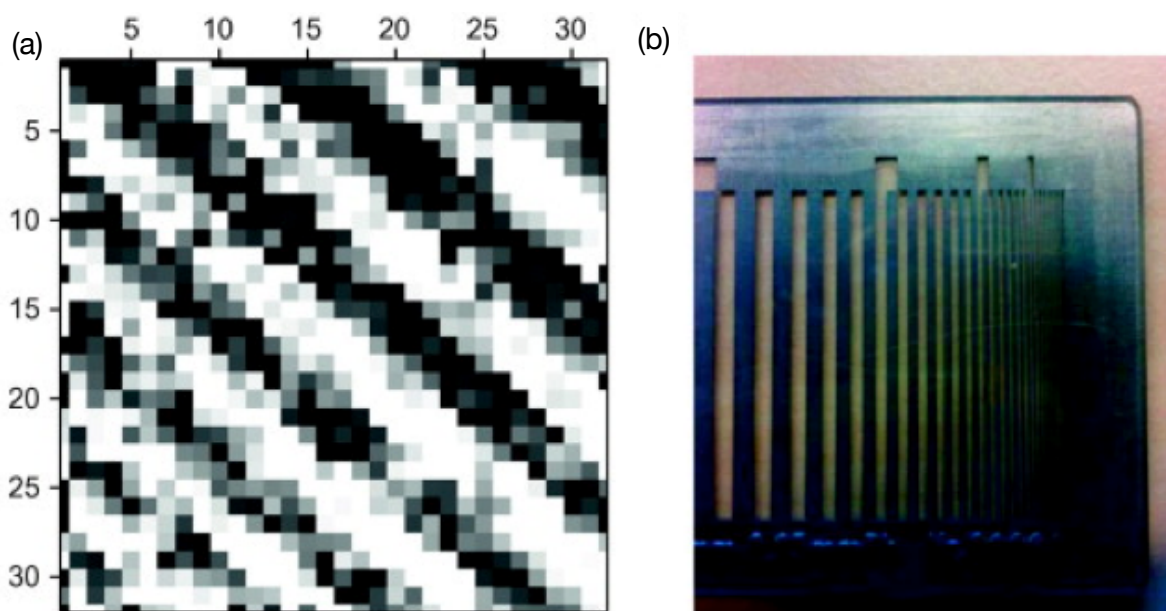


Figure 3.9(A) X-ray image of a lead object with slits (lines and spaces of varying dimensions). The lead object was placed such that the pattern of lines and spaces becomes progressively wider from the left bottom corner to the right upper corner of the array. (B) Photograph of the actual object, imaged in (A).

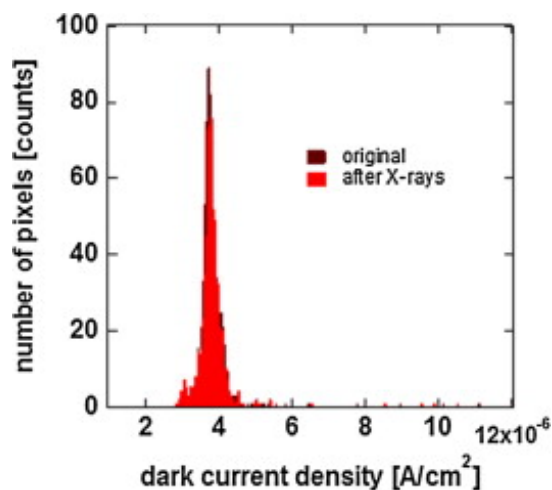


Figure 3.10 Histogram of measured photocurrent of 25 ppi array before and after exposure to heavy X-ray dose (estimated total dose 0.5 Gy).

Figure 3.11 shows the characteristics of the 127 ppi array. With increasing resolution, the use of a continuous photoactive layer introduces the possibility that charge created at one pixel can migrate to neighboring ones. The extent of this electrical crosstalk depends on the lateral conductivity, the potential difference between the pixels and frame rate, amongst geometrical factors. Figure 3.11(b) shows the recorded photo-image of the 127 ppi array that is exposed with a checkerboard pattern. Because the checkerboard is not aligned with the underlying pixel structure, some pixels are fully exposed, some are partially exposed, and some are not exposed. Although individual pixels can be discerned due to background current variation, the checkerboard pattern with dimensions of 1.6x1.6 mm² is faithfully reproduced with good edge fidelity. Next, approximately ten pixels of 200x200 mm² are exposed fully or partially (Figure 3.11(c)) by placing the array under a thin metal foil containing a small pinhole. Figure 3.11(d) shows the measured photocurrent of the exposed pixel region. The photocurrents of the exposed pixels are a factor of 10 higher than the background signal, with no significant crosstalk between neighboring pixels. The background (dark) current density of the small pixels is higher than that of the larger pixels (Figure (3.8)). This trend is opposite that reported by Baierl et al. [34], indicating that this is not fundamental to BHJ photodiodes. The increasing background current with decreasing pixel size in our arrays can have several origins. One possible reason could be that during the measurements, the TFT OFF-currents and/or dark photocurrents have increased and become relatively more important in the high-resolution array. We rule out this explanation, as we observed no increase in background current before, during and after operation. A

plausible explanation is that at the pixel edge the P3HT:PCBM layer separating the cathode from the conducting PEDOT:PSS is much thinner, resulting in excessive current leakage for smaller pixels. This is currently under investigation. A possible solution would then be to use a double bank pixel structure.

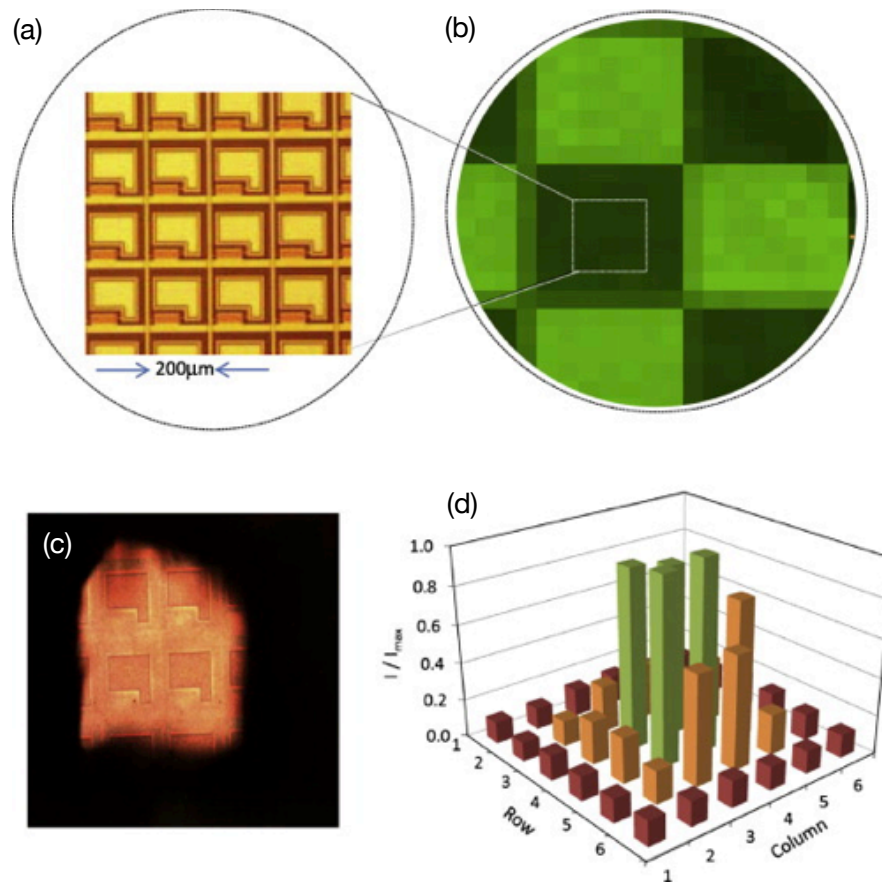


Figure 3.11 Characteristics of the 127 ppi array. (a) Top view micrograph of $200 \times 200 \mu\text{m}$ sensor pixels in 127 ppi backplane array. Row and column electrodes, active TFT area and pixel electrode are clearly visible. (b) Photo-image recorded by illuminating the detector array through a metal mask with square holes of 1.6 mm in a checkerboard pattern. Pixels in the lighter parts are exposed, pixels in the darker parts are not exposed. (c) Micrograph of ~ 10 pixels in array that are fully or partially exposed through a pinhole in metal, and its photo-image. (d) Photo-images were recorded by biasing the transistors with a gate voltage of -20 V or $+10 \text{ V}$ during selection and non-selection, respectively, and the common cathode at -2 V .

3.4 Conclusion

In summary, active-matrix photodetector arrays deposited onto plastic substrates have been fabricated. The backplane and photodetector are composed of solution processed, organic semiconductors. In contrast to commercial image sensor technologies, the photo-sensitive layer is continuous, greatly simplifying the manufacturing process. By characterizing the arrays with different pixel sizes, we showed that low light intensity differences of $\sim 1 \text{ mW cm}^{-2}$ can be resolved. Furthermore, X-ray images can be recorded at dose levels down to 0.27 mGy s^{-1} , i.e., in the range normally used in medical applications. This sensitivity is currently limited by (the non-uniformity of) the dark current of the photodiodes. Integrating other photoactive materials with lower dark currents [28] [34] [61]; increasing the pixel fill factor close to unity by employing a field shield design; and eliminating possible current leakage paths using alternative pixel edge designs would improve the performance of the large area image sensors further. In the following chapter, a lateral photodetector architecture is presented that aims to address the challenges associated with vertical organic photodetectors.

Chapter 4

Lateral Organic Semiconductor Photodetector

The first part of this chapter presents a lateral multilayer photodetector design that uses small-molecule organic semiconductor materials (CuPc and PTCBI). The second part, shows the use of an insulator material, such as polystyrene, can dramatically improve the dark current performance of the organic photoconductor without compromising the device's speed. The sensor can be operated the sensor under high bias to achieve significant improvements in the critical parameters for image sensors such as the photo-to-dark current ratio, sensitivity, dynamic range, and transient speed. This work has potential to expedite the adoption of organic semiconductor technology for a variety of digital imaging applications, especially in the field of low cost, portable biomedical equipment.

4.1 Introduction

Two photodetector geometries studied using organic semiconductor materials are lateral and vertical. Vertical photodetector design is similar to Organic Photovoltaic (OPV) design and has caught the majority of research groups' and industry's attention. Materials, processes and theories have been developed for the vertical design, to tune and obtain high performance devices. Vertical photodetector designs promise higher quantum efficiency; however, the associated dark current is still an order higher in magnitude than the existing state-of-the-art detectors commercially available using a-Si technology. So far, the best vertical photo detectors using small-molecule organic semiconductor materials are reported to have dark current densities in the range of 10^{-7} A/cm² at -5V, with an external quantum efficiency of 60.1% at green wavelength [18]. These detectors show a high selectivity to green wavelength, which allow their use in coupled scintillator-based systems for indirect X-ray imaging application. These photodetectors require transparent conducting electrodes along with other blocking layers, making them complex in design.

The other detector design is the Metal Semiconductor Metal design or MSM design which consists of lateral in-plane electrodes. The conduction path in an MSM detector is considered to be lateral, and the detection mechanism is photoconduction. In a lateral organic photoconductor structure, the organic semiconductor layer acts as both a charge generation and transport layer. With the incident

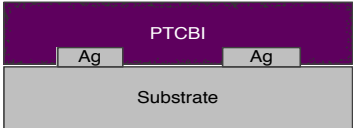
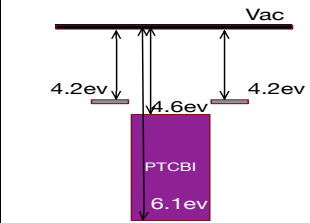
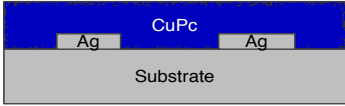
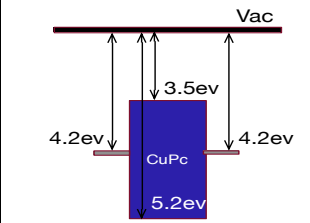
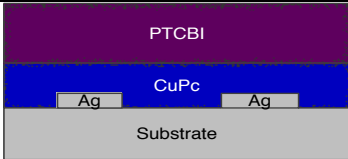
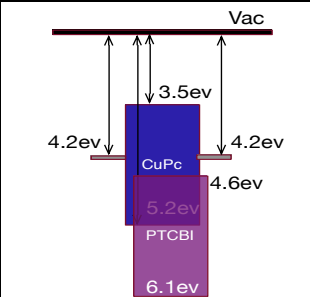
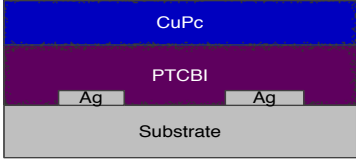
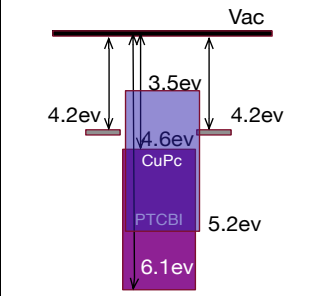
light, exciton are generated in the organic semiconductor's active layer. The photo-generated excitons are separated into corresponding electrons and holes with the assistance of an electric field (due to the applied voltage bias) in the bulk material and at-grain boundaries of the bulk material. Concentration of charges due to photogeneration is increased under illumination, and the channel become less resistive.

Lateral photodetector designs do not require a transparent electrode, and light can enter from the top in the case of bottom contact and from the bottom in case of top contact structures. The photoactive film is not covered and is exposed. The current in a lateral detector is dependent on the amount of charge injected from the metal and the channel length, which is defined by the spacing between the two contact electrodes. These detectors report lower quantum efficiency than vertical photodetectors, and a fill factor of less than 100%. Due to their simple design, they are easily integrated with backplane TFTs. In addition, low capacitance, low dark current, and a simple design with low electronic noise are useful features of lateral photoconductors in sensor applications.

4.2 Dual Layer MSM Photoconductor

In order to evaluate the effect of dual-layer heterojunctions on photodetectors, single and bilayer organic semiconductor photoconductor were fabricated. The Small-molecule organic semiconductor Copper Phthalocyanine (CuPc) and 3,4,9,10 perylenetetracarboxylic bisbenzimidazole (PTCBI), well known donor acceptor materials were used to form the single and dual-layer devices. The device cross-sectional layout and the band diagram are given in Table 4.1.

Table 4.1 Single and double layer devices, cross-sectional layout and energy diagram

Device number	First layer	Second layer	Structure	Band Diagram
Device 1	CuPc			
Device 2	PTCBI			
Device 3	CuPc	PTCBI		
Device 4	PTCBI	CuPc		

The devices (1 to 4) use silver metal as their electrodes metal. The electrodes are deposited using a shadow mask with a channel length of 22 μm and width of 1.5 mm on a glass substrate. All metal and organic layers are deposited using a vacuum thermal evaporator at a base pressure of 10^{-6} Torr. A current voltage (I-V) characteristic of each device is investigated using an Agilent 4156

semiconductor parameter analyzer. The devices are tested in nitrogen flow environment and at room temperature.

4.2.1.1 Results and Discussion

The current voltage characteristics of the single layer devices PTCBI and CuPc are investigated in the dark and under illumination. White light with a power intensity of $10\text{mW}/\text{cm}^2$ is used to illuminate both devices. The dark current of the PTCBI and CuPc only devices are measure as 1 pA and 0.2 nA , respectively at 10 V of applied bias ($0.5\text{V}/\mu\text{m}$), as shown in Figure 4.1.

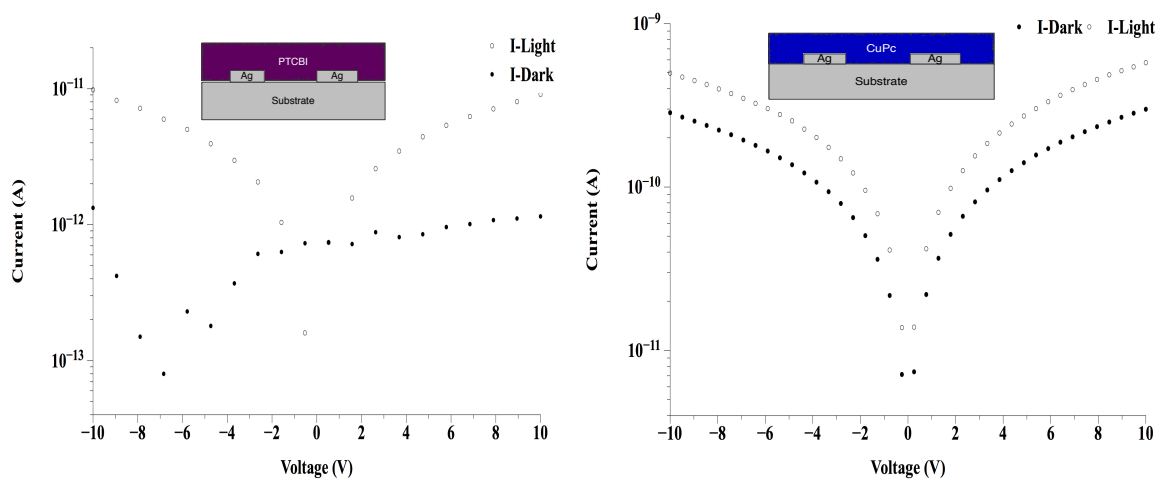


Figure 4.1 Single layer device photo current and dark current at different voltage biases, PTCBI-only device (a), CuPc only device (b)

The dark current in the PTCBI only device is due to the injection of carrier under an applied external bias. Electrons are injected from the metal's negatively biased contact into the PTCBI LUMO. The potential difference between the metal work function and the LUMO energy level of the PTCBI acts as a potential barrier for electron injection. When light is illuminated, photons are absorbed in the PTCBI layer and generate excitons. These photo-generated excitons are then separated into electrons and holes. The exciton separation takes place in the bulk layer and at the metal semiconductor interface. The increase in current under light is due to the excess of Photo-generated electron and holes.

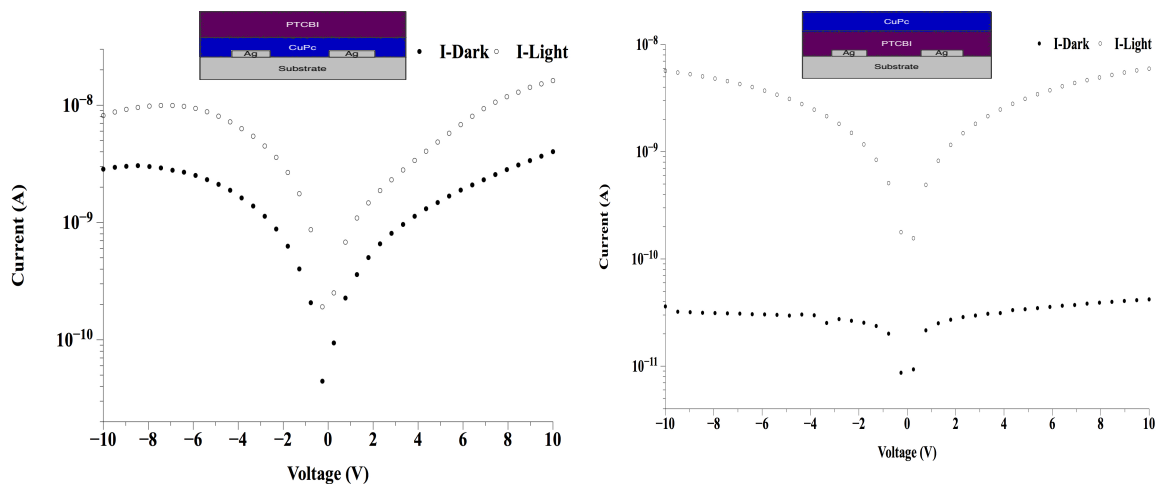


Figure 4.2 Dual layer device photo current and dark current at different voltage biases, CuPc bottom and PTCBI on top (a), PTCBI bottom and CuPc on top (b).

In the case of a bilayer design with CuPc on the bottom and PTCBI on the top, the dark current is higher than for the PTCBI-only device, and ten times higher than for the CuPc only device. The increase in dark current is due to the presence of heterojunction interface that acts as a less resistive path for the injected charges. Next, the dark current bilayer heterojunction device with PTCBI as its bottom layer and top CuPc is measured (device 4). The device showed a significant increase in photocurrent and a photo-to-dark current ratio of 100 at 1-mW/cm² illumination. The dark current of device 4 is approximately 20pA at 8V of applied bias (0.4V/um), which is close to the dark current value of PTCBI-only device.

Here it is important to mention that both the bilayer devices (device 3 and device 4) have comparable photocurrents in the range of 10 nA, whereas the dark currents are comparable to those of the corresponding single-layer devices. The above results indicate that in a bilayer heterojunction interface the dark current is dependent on the organic metal interface, whereas the photocurrent is mainly a function of the heterojunction interface.

4.3 Lateral Photodetector Design with Interface Layers

4.3.1 Introduction

In this work, we have established for the first time the use of polystyrene thin film to significantly reduce the dark current in a lateral multilayer organic semiconductor photodetector. A thin layer of polystyrene as an interface layer is added in between the metal electrodes and the organic semiconductor layer. This layer improves the photosensor performance by significantly reducing the dark current while maintaining a high photo-to-dark current ratio for a range of applied bias voltages and illumination intensities. The incorporated polystyrene thin film in a lateral organic semiconductor photodetector design reduces the dark current to two-orders of magnitude as compared to state-of-the-art organic photodetectors.

The fabricated device presented here is a bottom contact geometry with 5 μm -spaced symmetric electrodes, and it has a lateral bilayer organic semiconductor design [62], it yielded a measured photo-to-dark current ratio of 120, with an applied electric field bias of 4 V/ μm . The organic photodetector design with interface layer that we propose has a dynamic range and sensitivity comparable to the detectors reported using organic semiconductor technology [3], [63], and it paves the way for widespread adoption of organic semiconductor detectors into the mainstream.

4.3.2 Method and Materials

4.3.2.1 Fabrication

We fabricated the lateral multi layer photodetector on a 0.2 mm thick, 3 inch circular Corning glass substrate. The substrate was first cleaned using RCA-1 and loaded in a metal DC sputter, then a thin film of Aluminum (Al) metal is deposited at a base pressure of 2.0×10^{-7} Torr. Lateral in-plane interdigitated Al metal electrodes are patterned using conventional photolithographic techniques. The patterned wafer is loaded into the vacuum thermal evaporator where Polystyrene (PS) 1,200 g/mole molecular weight is thermally evaporated. Afterwards, Copper Phthalocyanine (CuPc) and 3,4,9,10 perylenetetracarboxylic bisbenzimidazole (PTCBI) thin films are deposited. The device geometry and structure are shown in Figure 1, inset. CuPc was purchased from S.W. Sands and PTCBI was purchased from LumTech; no further purification of these materials was performed. These materials are evaporated using a shadow mask at a rate of 0.1 nm/sec to achieve a desired thickness of 50 nm

PTCBI and 30 nm CuPc in a vacuum of 3×10^{-6} Torr. The devices are kept for measurement in a nitrogen flow environment at room temperature.

4.3.2.2 Measurements

Measurements are made using the Agilent semiconductor parameter analyzer model 4156C. Devices are connected using a set of Signatone low noise triax probes. Blue (480 nm), Green (525 nm), Red (650 nm) LEDs are used as optical excitation sources. These LEDs are driven using a DC 2400 Agilent source meter. A calibrated silicon photodetector (Newport photo diode 918D) with a power meter (Newport model 1931-C) is used to measure the optical power of the LEDs. Each LED is placed 4 cm above the photodetector. An in-house optical diffuser is used to obtain a uniform spread of light. Ocean Optics spectrometer (model QE-65000) is used to measure the emission wavelength of each light source after it passes through the optical diffuser.

Transient measurements are performed using the green LED (525nm) operated by a square waveform generator (Tektronix AFG3102 Dual channel function generator) set at 5Hz with a 50% duty cycle. The photodetector is biased using an external power supply (Keithley Model 6430 source meter). The output of the photodetector is feed to a low-noise transimpedance (current) amplifier (Model EG&G 5182). The transimpedance amplifier is operated using rechargeable NiMH batteries to reduce the noise. The AC output of the transimpedance amplifier is then connected to an oscilloscope (Tektronix Model TDS2014, 100MHz, 1GS/sec) to read out the transient behavior of the photodetector.

4.3.3 Results and Discussion

In order to demonstrate the use of polystyrene to reduce the dark current in a lateral organic semiconductor photodetector, we used a bottom contact Metal Insulator Organic Semiconductor Insulator Metal (MIOSIM) design. The bottom contact structure was chosen as it is most easily integrated with the current thin film transistor (TFT) backplane process [21]. We used the well-investigated small-molecule organic semiconductors Copper Phthalocyanine (CuPc) and 3,4,9,10 perylenetetracarboxylic bisbenzimidazole (PTCBI) and the insulator material polystyrene. The structural and electronic properties of CuPc and PTCBI organic semiconductors have been deeply investigated [14], [16], [22], [64-69]. CuPc and PTCBI can be thermally evaporated, giving the advantage of good control of the device fabrication process, in particular on the thickness, uniformity and surface roughness of the thin film [45].

4.3.3.1 Absorbance

The UV-Visible absorption spectrum of each thin film on glass (Figure 4.3(a)) is measured on a daughter sample fabricated together with the actual device. The polystyrene (PS) thin film has less than 5% absorbance for a wavelength range from 300 to 850 nm. The CuPc and PTCBI thin films show absorption peaks at 540 and 625 nm, respectively, in agreement with values reported in the literature. [16]. The absorption spectrum of the PTCBI, CuPc bilayer with PS and without PS shows identical absorption, which further verifies that PS has no absorbance for a wavelength range from 300 to 850 nm. CuPc and PTCBI have a wide absorption spectrum both in visible and ultraviolet (UV) as shown in Figure 4.3(a). The band offset between the HOMO and LUMO of the two materials is greater than the binding energy of the Photo-generated excitons [45]. Figure 4.3(b) shows the energy diagram representation of the MIOSIM photodetector, and schematic diagrams highlighting the conduction path in dark and in light are shown in Figure 4.3(c).

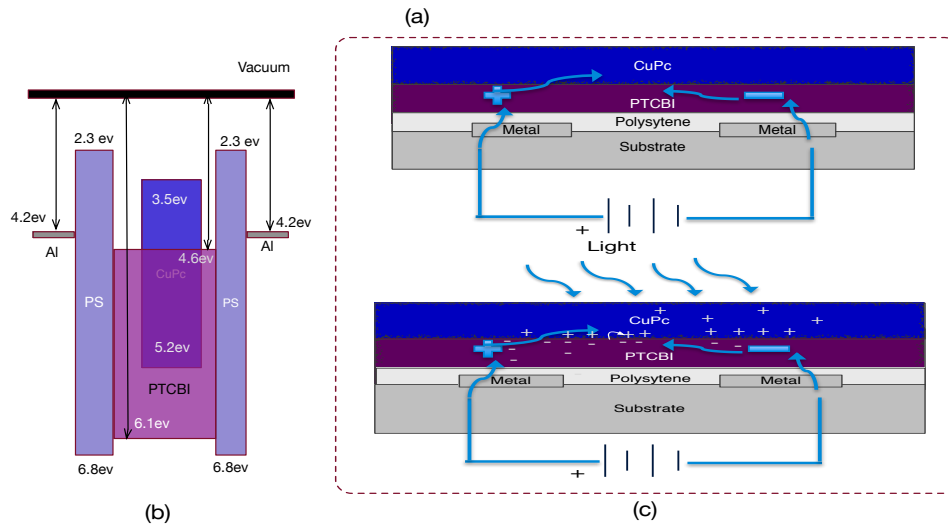
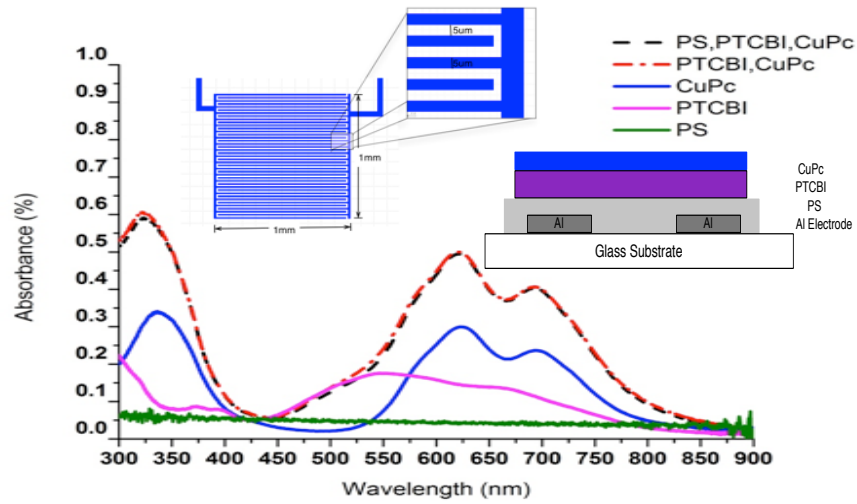


Figure 4.3 (a) Absorbance as a function of wavelength of thin film of polystyrene (50nm), CuPc (30nm) PTCBI (50nm) and combined three-layer polystyrene (50nm): CuPc (30nm): PTCBI (50nm). Inset shows the lateral interdigitated electrodes patterned on glass, with an electrode spacing of 5 μm , and overall area of 1 mm^2 with active area of $5.0 \times 10^{-3} \text{ cm}^2$, device cross sectional layout: Aluminum metal electrodes with length of 5 μm , 1 mm width channel, 5 μm wide metal electrode; thermally evaporated Polystyrene (PS); 50 nm, PTCBI; 30nm CuPc. (b) Energy diagram of the photodetector. (c) Device cross sectional layout explaining the dark and the photoconduction.

4.3.3.2 IR-Measurement

IR measurements were performed both on the thermally evaporated PS layer and the base material to verify the evaporated polystyrene film. The film was measured on glass using germanium crystal.

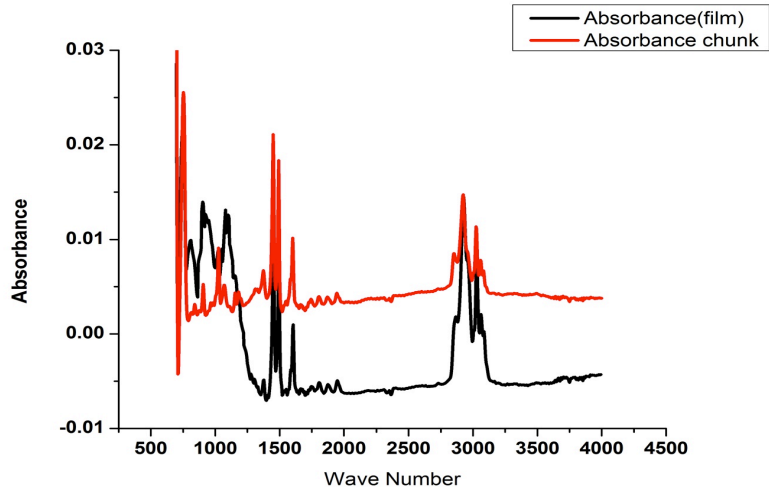


Figure 4.4 IR-spectrum of polystyrene thin film and polystyrene base material.

4.3.3.3 Current Voltage Characteristics

The current-voltage characteristics of the lateral bilayer organic semiconductor-based photodetector without polystyrene (Metal Organic Semiconductor Metal Design) and with polystyrene thin films of different thickness between metal contacts and active heterojunctions (MIOSIM design) are shown in Figure 4.5. Clearly, with the introduction of a thin film of PS, the dark current is reduced in the latter device. For a PS film 10 nm thick, the dark current at an applied voltage bias of 15 V (3 V/ μm) decreased from 2.4 to 0.5 nA. It is further observed that, for detectors with polystyrene thickness values of 50 and 100 nm, the dark current was further reduced to 140 and 90 pA, respectively.

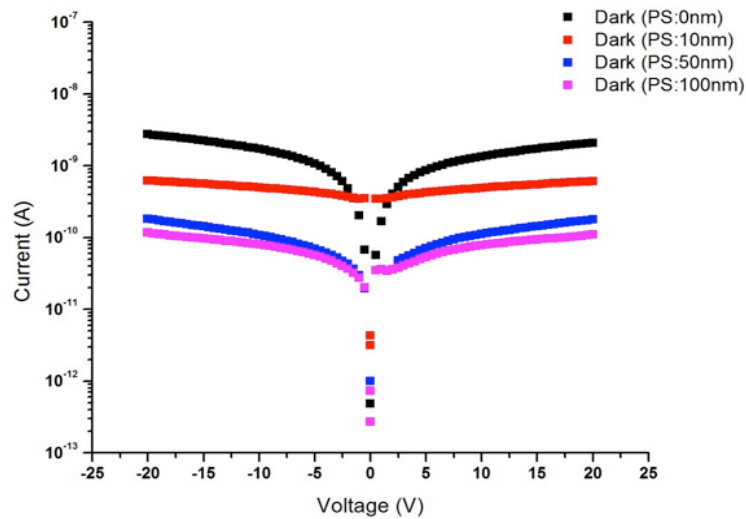


Figure 4.5 I-V Response: under dark with no polystyrene and with polystyrene of thicknesses of 10, 50, 100 nm, showing a significant reduction in dark current.

The dark current in the organic semiconductor photodetector is primarily due to the injection of charge carriers from the metal side into the first organic semiconductor layer (i.e., PTCBI layer) at a set bias voltage, and also due to the thermally generated charge carriers inside the organic semiconductor layers. The addition of the PS layer in between the metal electrodes and the organic semiconductor layer forms an energy barrier (shown in figure 4.3(b)), which limits the charge injection and therefore reduces the photodetector dark current. At room temperature the number of thermally generated charge carriers is small therefore the dark current due to thermal generation is small and can be neglected typically.

4.3.3.4 Interface Layer: Conduction

In order to understand the mechanism responsible for the dark and photo current inside the device, two daughter samples are fabricated. The first sample consists of a PS layer (50 nm thick) without an organic semiconductor active layer (Figure 4.6) whereas the second sample consisted of PS layer (50 nm thick) without organic semiconductor active layer but with an additional 15 nm thick aluminum top contact (Figure 4.7). With these two samples, a DC potential is applied across the two electrodes. In the case of the first sample, there is no significant lateral conduction observed under dark and in

white light ($1\text{W}/\text{cm}^2$) conditions (figure 4.6). However, the current voltage characteristics of the second sample showed that upon application of a 5 V electrical bias across the lateral electrodes, polystyrene starts to conduct showing that the conduction path in the MIOSIM device is vertical instead of lateral (Figure 4.7). If a careful compliance current is set, the sample can be operated repeatedly without bringing it to a permanent breakdown. No photo response is observed under illumination with white light (Figure 4.7).

Polystyrene (PS) is known to be a non polar insulator with no intrinsic surface states [70]. The donor level for hole transport is located at 6.80 eV vs vacuum level, and the acceptor level for electron transport is located at 2.3 eV. The optical absorption edge of PS is approximately 4.43 eV. For PS, the literature reports on field-dependent charge transport: at low electric fields, transport is governed by the Poole-Frenkel model, whereas at higher fields, space charge limited currents (SCLC) are observable [71].

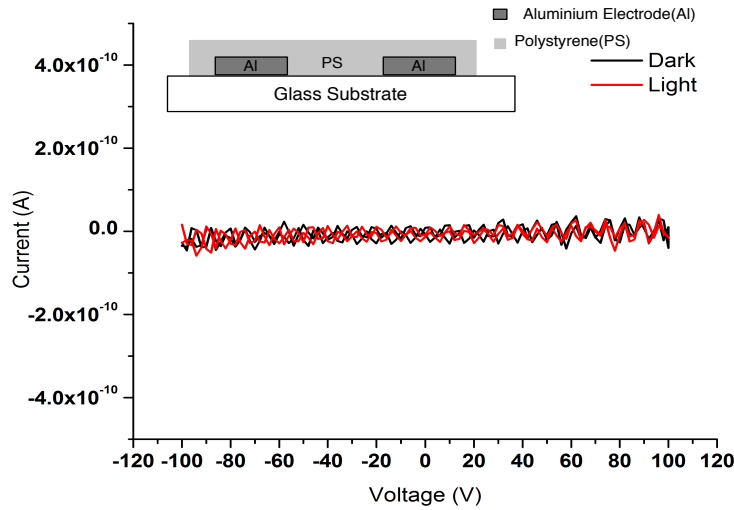


Figure 4.6 Current voltage characteristics of polystyrene only device under dark and $1\text{ W}/\text{cm}^2$ of white light. No conduction in lateral $5\text{ }\mu\text{m}$ channel is observed in dark either or light.

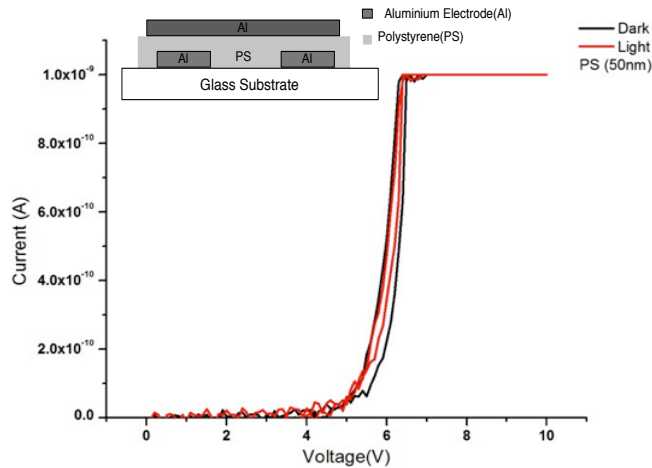


Figure 4.7 Current voltage characteristics of polystyrene with aluminum top electrode under dark and 1 W/cm^2 of white light, showing conduction at a threshold voltage at 5 V across the lateral electrodes in lateral $5 \mu\text{m}$ channel with no observable photo response.

4.3.3.5 Photo and Dark Current Characteristics

Figure 4.8 shows the photo and dark current characteristics as a function of the applied electrical bias with no PS (Figure 4.8(a)), 10 nm- (Figure 4.8(b)), 50 nm- (Figure 4.8(c)) and 100 nm-thick (Figure 4.8(d)) polystyrene film. The current vs voltage curves show a symmetric photoconductive behavior with no open circuit voltage. The curves are similar to those typical of a photo field-effect transistor (FET) with an embedded photogate [72-74]. The symmetry in the output characteristics (i.e., measured current in both positive and negative bias voltages) is due to the use of metal contacts with the same work function and to the symmetric structure of the device. The photocurrent decreases slightly with the addition of PS in between the metal electrodes and the active layer. This slight decrease in the photocurrent is due to the potential barrier built up at the PS-PTCBI interface and to the electric potential drop across the PS layer. The drop in potential across the active layer (PTCBI, CuPc bilayer) reduces the drift current through the device, thus leading to a reduced collection of Photo-generated charges. On the other hand, it allows for higher bias voltages to be applied to the device. At higher bias voltages, the field inside the active layer increases, thus facilitating the collection of photo-generated charges and increasing the photocurrent and photo-generation efficiency (the ratio of the number of photo generated charges to the number of photon incidents,

generating an electron hole pair). The PS layer also critically limits the injection of charges from the metal electrode into the semiconductor, which reduces the dark current albeit with a slight reduction of the photocurrent. The net effect is positive, i.e., a significant improvement in the photo-to-dark current ratio, as the on-off ratio of the photodetector (Figure 4.9). The photo to dark current ratio of the lateral detector is dependent on the applied bias, photo illumination intensity, and absorbance of the organic layers. In case of high dark current, the photo to dark current ratio is small. Using PS as interface layer we have improved (six times) the photo-to-dark current ratio (i.e., from 20 with no PS to 120 with 50 nm of PS) under the green light 525 nm wavelength. This ratio can be further improved by using a thick organic film and a high external bias voltage or using a high-intensity light source.

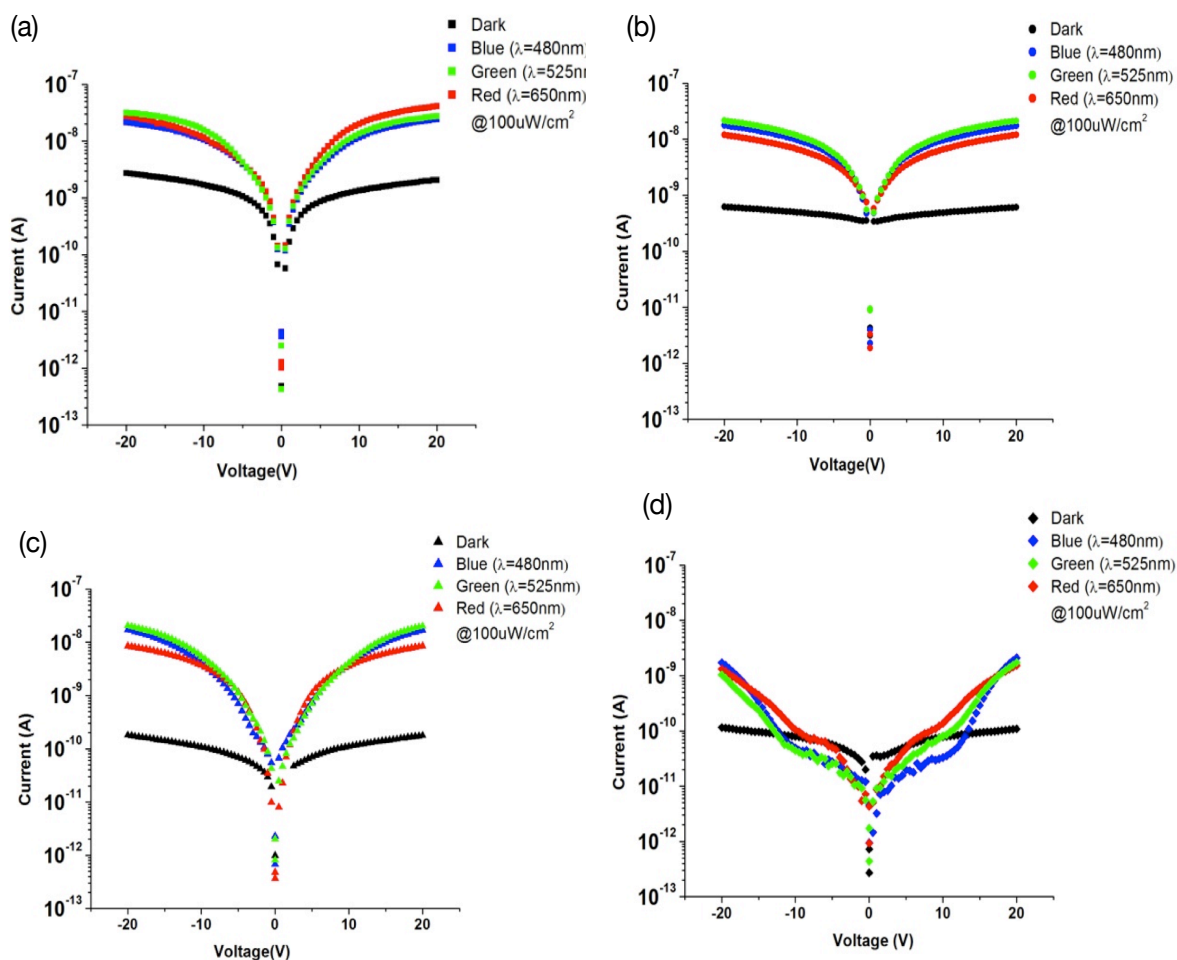


Figure 4.8 Current-Voltage characteristics of the lateral MIOSIM with no PS (a), 10 nm PS (b), 50 nm PS (c), 100 nm PS (d). The photocurrent is measured under illumination power of $100 \mu\text{W}/\text{cm}^2$ using a Green (525 nm), Blue (480 nm) and Red (650 nm) LED light source.

The active layer (CuPc, PTCBI) consists of a bilayer heterojunction where light illuminates on the photo detector from the top. Photons are absorbed in the active layers and generate excitons either in the CuPc or PTCBI layers based on the absorption coefficient of either material, at the incident wavelength. The energy offset in between the lowest unoccupied molecular orbital (LUMO) or highest occupied molecular orbital (HOMO) of CuPc and PTCBI is greater than 0.9 eV. This value is much greater than the exciton binding energy (about 0.2 eV) which makes the separation of excitons into electron and hole pairs energetically favorable. [45], [64], [65] The excitons diffuse to the interface, leading to the generation of electrons in the LUMO of PTCBI and holes in HOMO of the

CuPc. The energy offset at the interface in between the HOMO and LUMO forms a potential well. This potential well acts as a localized trap and limits the recombination of the Photo-generated carriers. The electrons and holes accumulated at the interface increase the Photo-generated carrier concentration and the channel current under bias. The PS layer obviously has no absorption as shown in Figure 4.3(a) and no photogeneration as shown in Figure 4.5 and Figure 4.6. The conduction through PS is due to the vertical trap-assisted Space Charged Limited Conduction (SCLC), with assistance from the bias-induced electric field [71]. As noted earlier, PS is a non-polar material, and the existence of the dipole effect at the metal/PS interface can be safely ignored, as can be the relocation of the metal work function.

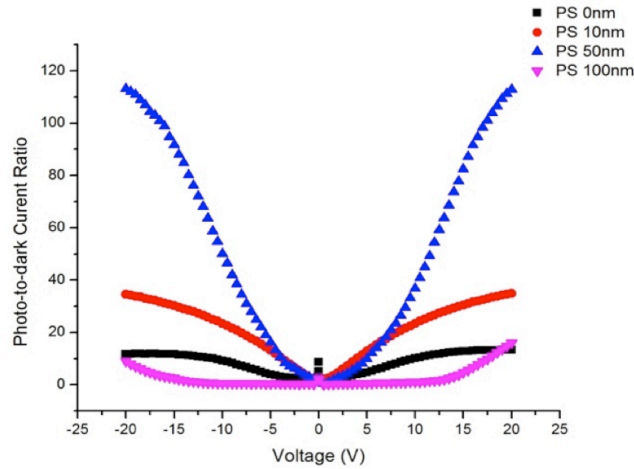


Figure 4.9 Plot of photo-to-dark current ratio versus applied voltage for a $100 \mu\text{W}/\text{cm}^2$ green (525 nm) light for samples with 10nm, 50 nm, 100 nm thick PS and without PS.

4.3.3.6 External Quantum Efficiency

The External Quantum Efficiencys (EQEs) of the photodetector with no PS, and 10 nm, 50 nm and 100 nm of PS are shown in Figure 4.10(a-d). The EQEs are calculated at an excitation wavelength of 480, 525 and 625 nm, under an illumination power of $100 \mu\text{W}/\text{cm}^2$ for a range of voltage biases (0 to 20V). The detector with 10 nm of PS has an EQE of 9.8%, and the detector with 50 nm of PS has an EQE of 9.57% at a wavelength of 525 nm.

The EQE and photo-to-dark current ratio of the 50nm PS detector at a bias voltage up to 120 V using a low illumination power of $3.6\mu\text{W}/\text{cm}^2$ are shown in Figure 4.11. When calculated at a high bias voltage and lower illumination power (as is typically with large-area digital medical detectors),

the EQE reaches up to 42%, which is comparable to the EQE of vertical organic photodetectors [3]. To the best of our knowledge, the EQE of lateral detectors using a PTCBI and CuPc bilayer has never been reported. Other lateral designs have reported maximum EQEs of 12% at 525 nm using TPD and PTCBI bilayers and 10% for a a-Si MSM photoconductor at (525 nm) [22] [75]. For amorphous silicon with an insulating layer, an EQE of 65% was reported [76].

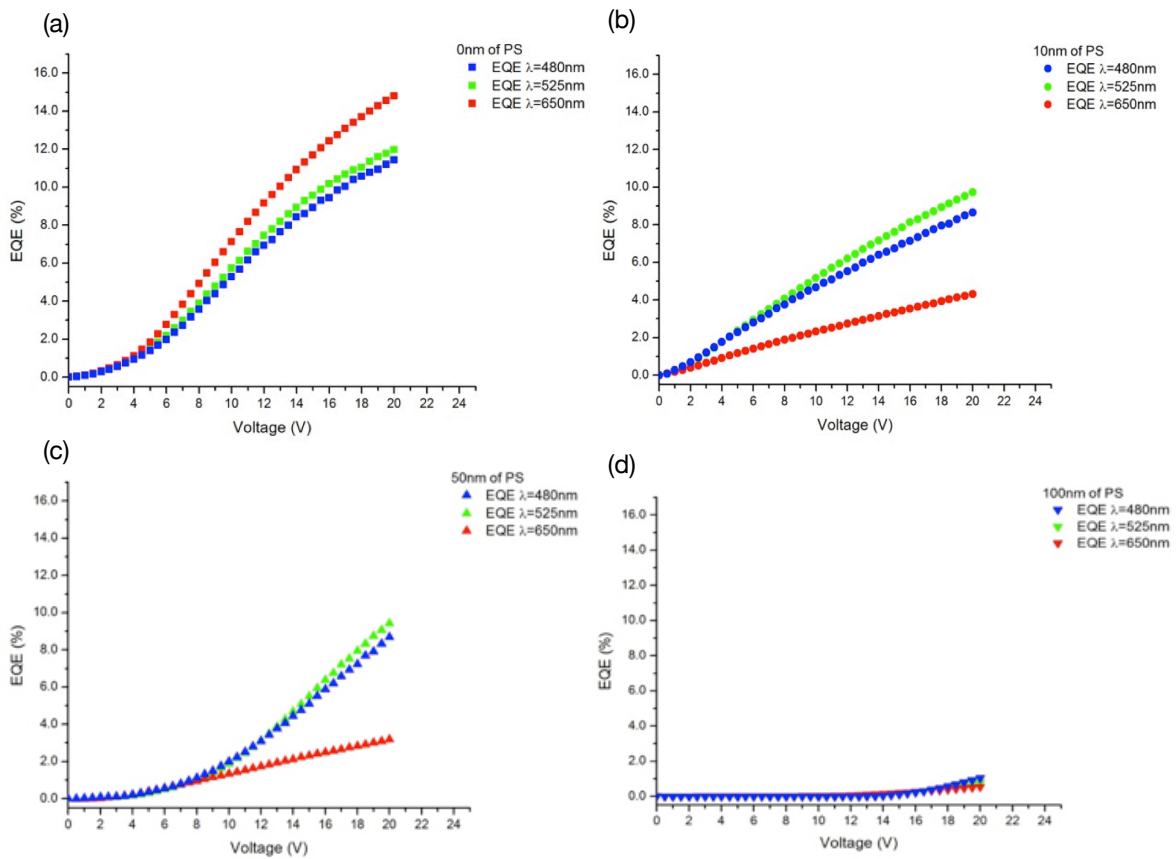


Figure 4.10 (a) EQE as a function of applied voltage with no PS; (b) EQE as a function of applied voltage with 10 nm of PS; (c) EQE as a function of applied voltage with 50 nm of PS; (d) EQE as a function of applied external voltage with 100 nm of PS.

Note that the detector we have reported with 50 nm PS absorbs only 15% of the incident light at 525 nm wavelength, as shown in Figure 4.3(a). Thus only 15% of the incident light contributes to the detector's EQE. If more of the incident light is absorbed in the organic bilayer, the EQE can in principle be considerably higher. This work does not include the optimization of the photodetector's

EQE, since the focus of the study on is a novel technique to improve the dark current performance of the photodetector and thus the ability of the detector to sense lower light levels.

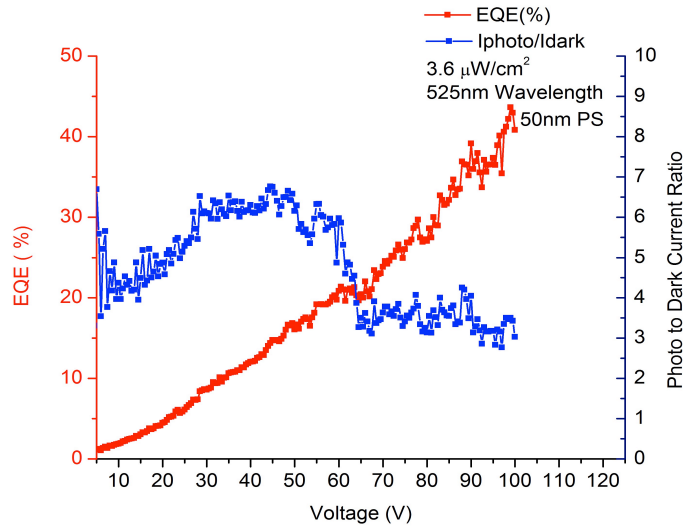


Figure 4.11 Photo-to-dark current ratio and external quantum efficiency as a function of applied bias using 525 nm wavelength LED at an illumination power intensity of $3.6 \mu\text{W}/\text{cm}^2$.

4.3.3.7 Linearity

In figure 4.12(a), I-V curves for the 50 nm thick PS layer detector are shown at different light intensities, and Figure 4.12(b) shows a 50 nm PS layer device being operated at different bias voltages and different light intensities to highlight linearity.

The photocurrent at applied biases of 5 V, 10 V, 15 V and 25 V, is analyzed for linearity. The results presented in Figure 4.12(b) shows that the detector has a linear response for a range of intensities i.e., $3.6 \mu\text{W}/\text{cm}^2$ to $380 \mu\text{W}/\text{cm}^2$.

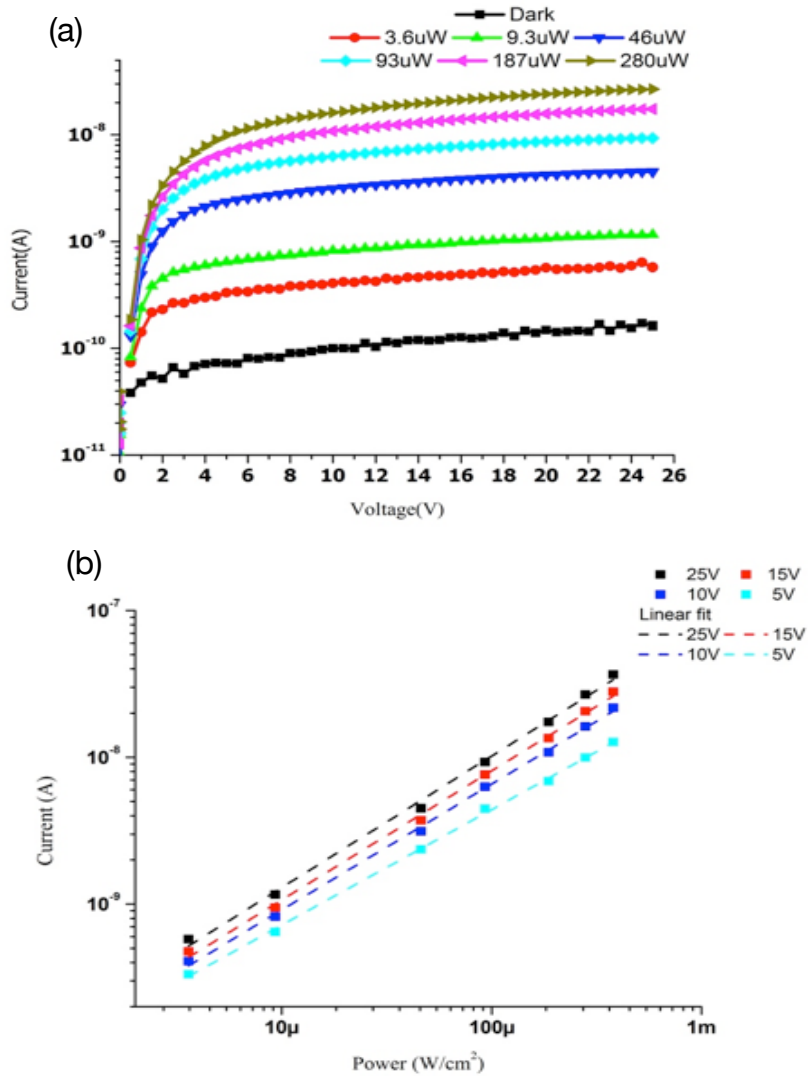


Figure 4.12 (a) I-V Response of 50 nm PS detector at range of illumination intensities; (b) Linearity plot, photo current as a function of light power using a 525 nm LED source at 5 V, 10 V 15 V 25 V external bias voltages

4.3.3.8 Detector Speed

To investigate the effect of the polystyrene interface layer on photodetector speed, transient measurements are performed. Figure 4.13(a) shows the block diagram of the transient measurement setup used. The detector is illuminated using a Green LED (525 nm), illumination intensity of $100 \mu W/cm^2$, operated using a square wave (50% duty cycle) signal. The switching frequency is set at 5 Hz. Figure 10(b) show the oscilloscope output of each detector (D1-D4). Using a transit time at 10%

and 90% of the steady state value, detectors rise and fall times are calculated, as summarized in Table 4.2.

Table 4.2 Table summarizes the rise and fall times of D1, D2, D3 and D4 photo detectors

Device	Polystyrene Thickness (nm)	Rise Time	Fall Time
D1	No PS	42.02msec	50.11msec
D2	10nm	40.30msec	46.24msec
D3	50nm	30.72msec	52.33msec
D4	100nm	26.41msec	56.41msec

As shown in Table. 4.2, the detector with PS has a faster response than to the detector without PS. The detector without PS has a rise time of 40.2 msec and fall time of 50.11 msec, and the detector with 50 nm of PS has a rise time of 30.72 msec and fall time of 52.33 msec. The difference in the transient response is explained as following: the addition of PS layer results in a relatively large capacitance between the metal contact and the organic semiconductor layers. This capacitance appears in series with the organic semiconductor active layer channel capacitance. As a result both the overall capacitance of the photodetector and the photodetector rise time are expected to decrease as observed. The rise time of the photodetector is measured when the LED is switched on. Under illumination, the photoconductivity of the organic active channel layer increases which means a decrease in the channel resistance and a subsequent lowering of the rise time.

Further we know that the junction capacitance (due to PS layer) is inversely proportional to the thickness of the PS layer. Thus for a fixed bias voltage and a fixed illumination intensity the photodetectors with 100nm thick PS show a shorter rise time as compared to the photodetector with 50nm, 10nm and no PS. Therefore the shorter rise time is due to both lower device capacitance and smaller photodetector channel resistance. The fall time is measured under dark. In dark the channel resistance is much greater which results in a longer fall time.

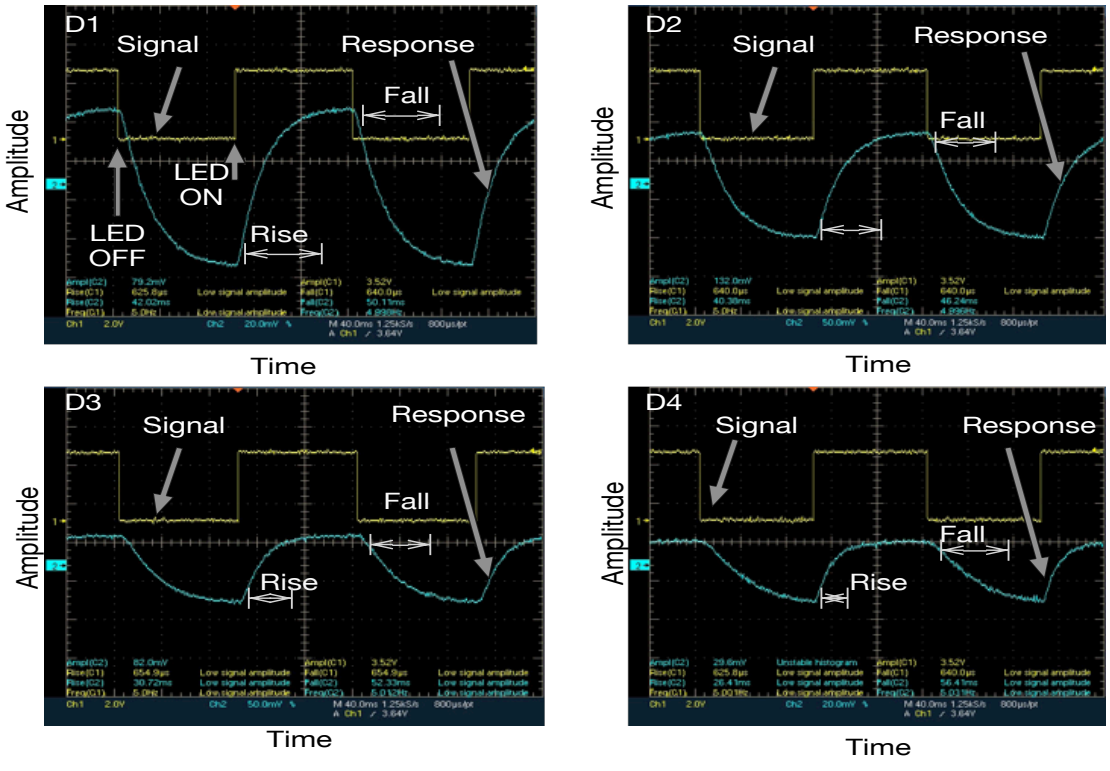
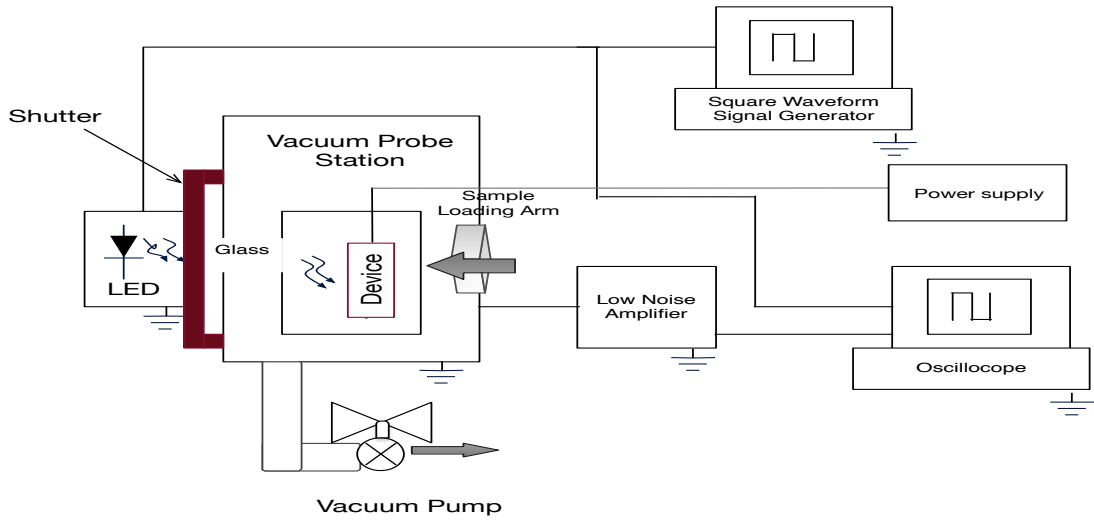


Figure 4.13(a) Block diagram of the test setup used to measure the transient response of the photodetector; (b) Graphs presenting the voltage input to illuminate the LED and the output voltage response of the detectors D1, D2 D3 and D4 vs time.

4.3.3.9 Transient Measurements

The transient response of the photodetector is shown in Figure 4.14

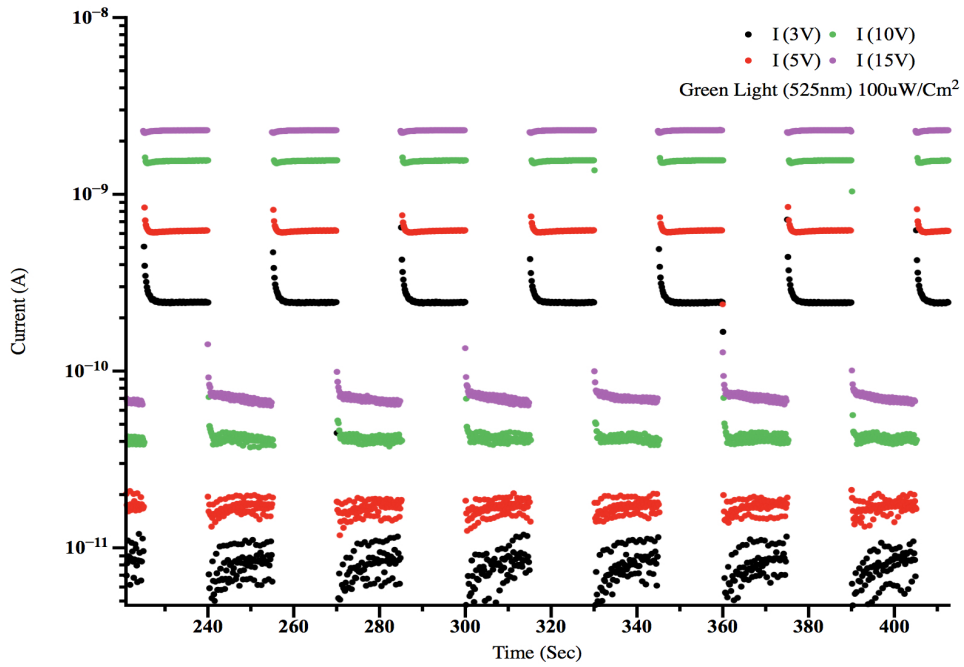


Figure 4.14 Transient response for 500 second run show detector following the input signal. The on and off current do not change over time.

Next a detector with 40 nm -PTCBI, 50 nm-PS and 30 nm-CuPc is fabricated and its current voltage characteristics, Transient response are given in Figure 4.15 and Figure 4.16. Table 4.3 summarizes the rise and fall time of the photodetector at different voltages.

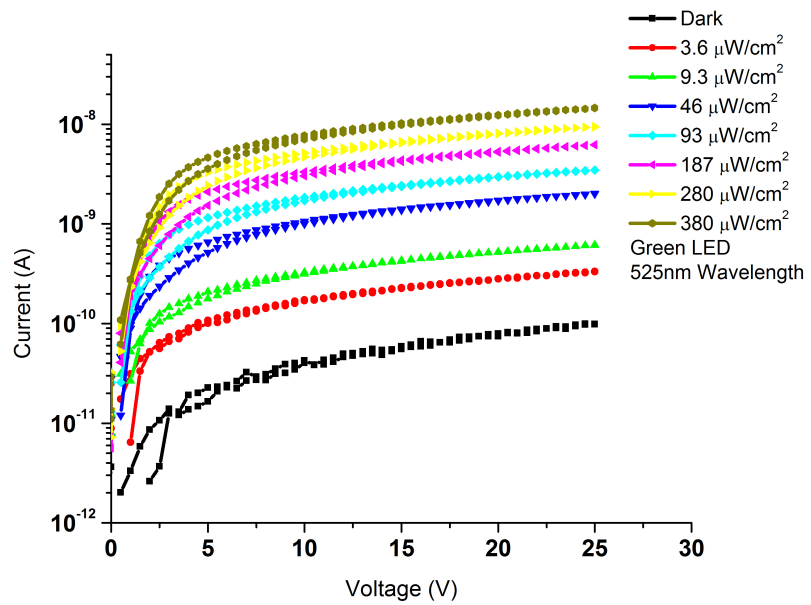


Figure 4.15 A lateral photodetector with 40 nm-PTCBI, Current Voltage characteristics under different illumination of light

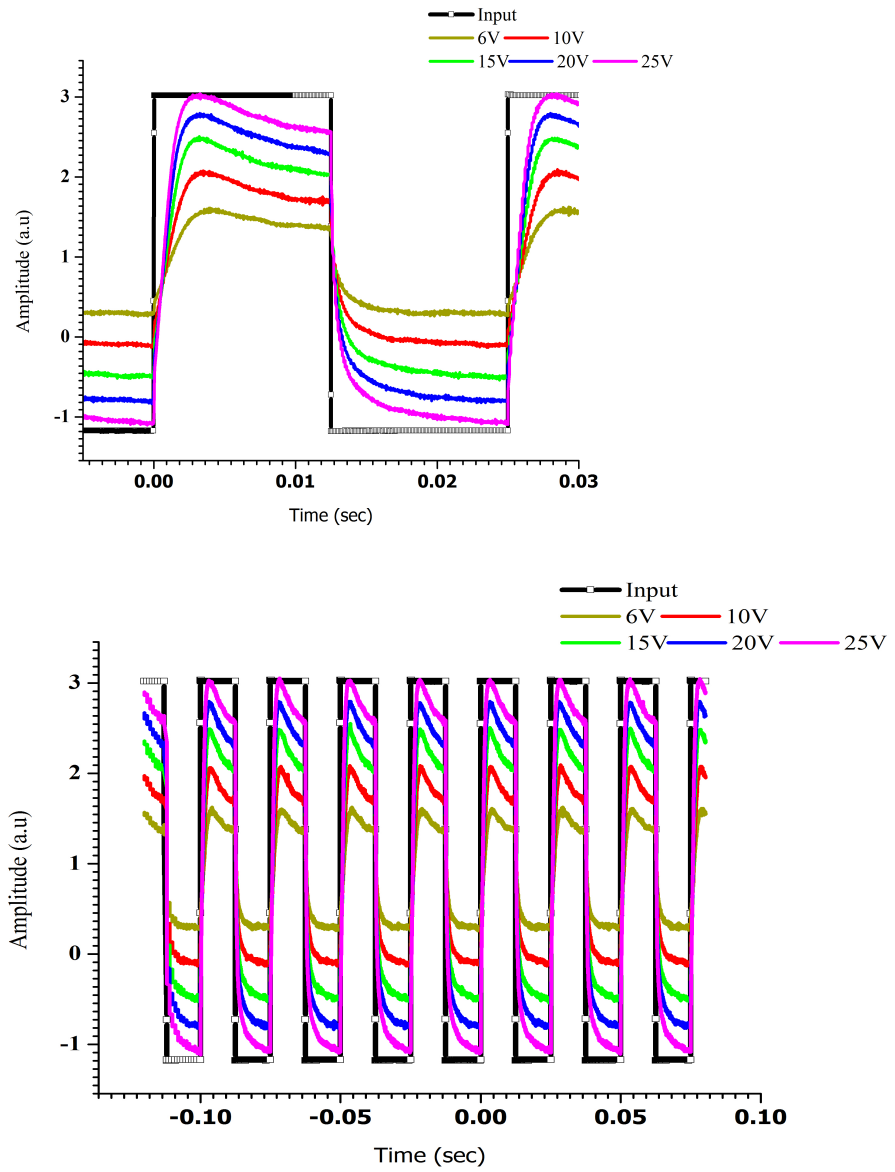


Figure 4.16 Lateral photodetector with 40nm -PTCBI, transient, rise time and fall time under different bias voltages

Table 4.3 Photodetector with 40nm of PTCBI, summary of rise time and fall time of photodetector at different applies biases

Voltage	Rise Time	Fall time
6V	1.78 mSec	1.96 mSec
10V	1.8 mSec	2.2 mSec
15V	1.46 mSec	2.11 mSec
20V	1.37 mSec	1.97 mSec
25V	0.968 mSec	1.97 mSec

As shown in Table. 4.3, the photodetector shows a lower rise time at a larger bias voltage. However the fall time does not change significantly with an increase in the applied voltage bias.

The transient measurements are performed at a fixed illumination power density. The rise time is measured when the device is illuminated i.e., the input LED is turned on. The fall time is measured in dark, when the LED is turned off. During illumination (LED is on) the number of photogenerated charges in the organic semiconductor layer increases and therefore increase the organic semiconductor channel photoconduction, which decreases the overall channel resistance. In addition at a greater bias voltage and increase in the number of carriers the semiconductor mobility increases resulting a channel with less resistance. Therefore, the rise time, which is a function of detector capacitance and resistance (RC), is less at a greater bias voltage. In the dark (LED is off) the channel conductivity does not change and so the fall time of the detector does not show voltage dependence.

In case of digital imagers a fast detector is required for fast speed operation. However in case of a pixel circuit the speed is dependent on the on pixel overall capacitance (including sensor capacitance and the capacitance due to the additional capacitor added to storage charge) and the resistance (that includes the load and the line resistances). It should be noted that because the lateral OPD inherently has a lower capacitance than a vertical OPD, a typically faster response time is observed for the lateral device.

4.3.3.10 Capacitance

The capacitance of the lateral photodetector measured in dark and in green light is given as a function of frequency.

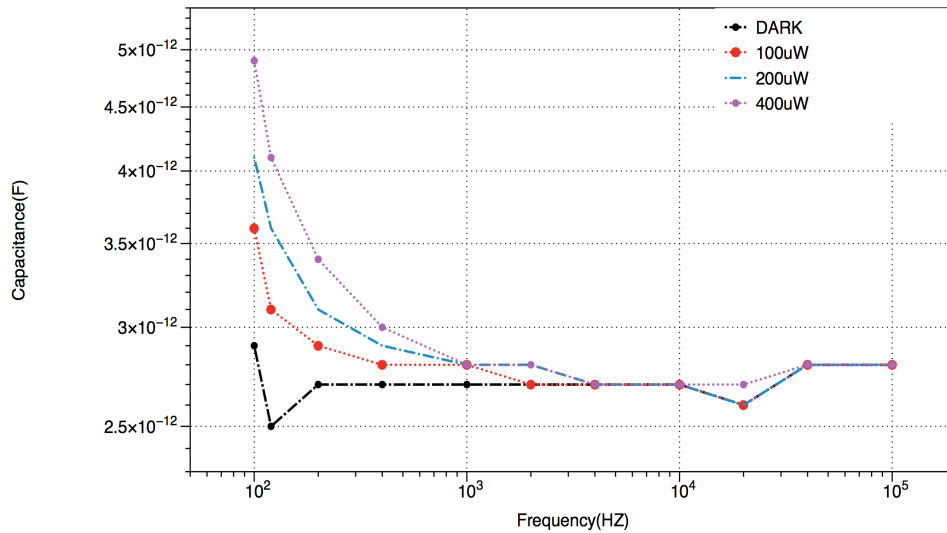


Figure 4.17 Capacitance as a function of frequency at different intensities of green light

4.3.4 Conclusion

In conclusion this chapter has reported a novel approach for tuning the dark current in a lateral organic semiconductor bilayer photodetector, based on the use of a non-polar insulator layer. Specifically, we have shown that introducing a thin film of polystyrene significantly reduces the dark current in a lateral photodetector based on a PTCBI CuPc bi-layer. An advantage of this design is the option to apply greater bias fields for improved speed and photo-responses as necessitated, for example, in large-area, indirect diagnostic, X-ray medical imagers. This thesis demonstrates for the first time, a lateral organic photodetector capable of detecting light intensities as low as $3.6\mu\text{W}/\text{cm}^2$, which is comparable to state-of-the-art vertical organic devices. Higher responsivity can be achieved by optimizing the semiconductor and insulator-layer thicknesses. This approach has the potential to open a new alternative for building low-cost portable diagnostic equipment, in particular for early diagnostics and improved health-care.

Chapter 5

Effect of Spacing in MIOSIM Photodetectors

This chapter explores the effect of electrode spacing in a bottom contact multilayer lateral metal-insulator-organic semiconductor-insulator-metal (MIOSIM) photosensor. Results show that the dark and photo current of the lateral MIOSIM photosensors are independent of the lateral spacing between the electrodes, which is in stark contrast to previously reported lateral organic photosensors. The conduction path for both the photo and dark current in the reported lateral MIOSIM photo sensor appears primarily to be due to vertical charge injection from the metal electrodes into the organic semiconductor layer through a polystyrene intermediate interface layer. More interestingly, the dark and photo current remains constant for a range of optical illumination intensities and biasing voltages.

5.1 Introduction

Lateral photosensor device designs incorporating both inorganic and organic semiconductors have been reported in the past using a metal-semiconductor-metal (MSM) design [22], [23], [62], [73]. The most recent reports, though, deviate from traditional MSM designs and fall into two categories: based on the use of a semiconductor bilayer to create an internal electric field for better charge collection or based on the use of an interface layer between the semiconductor layer and electrical contacts to reduce injection currents for lower dark currents. The former approach is reported extensively for organic materials [22], [23], and more recently, for an inorganic bilayer of amorphous silicon [77]. The latter approach to reducing injection currents, however, was pioneered by our group and was first demonstrated for a single layer of inorganic amorphous selenium [78]. Here, in the context of a bilayer organic device fabricated with an interface layer, we report, for the first time, the non-intuitive effect of channel spacing on device current.

Results indicate that the dark current in our MIOSIM device is independent of the lateral gap between the contact electrodes. We believe that the interface layer we employed (polystyrene here) defines the dark current through the vertical conduction path between the metal contact and organic semiconductor bilayer. Under light illumination, the density of the photo-generated charge in the channel increases, leading to a photocurrent that is greater than the dark current. The photocurrent eventually saturates for a given illumination level, regardless of device biasing voltage above a certain threshold.

5.2 Method

5.2.1 Design and Fabrication

A lateral bottom contact multilayer photosensor is fabricated using an organic semiconductor, 3,4,9,10 perylenetetracarboxylic bisbenzimidazole (PTCBI), as a charge transport layer and a photoactive exciton generating layers, Copper phthalocyanine (CuPc), as the charge separation layer. The molecular structure of CuPc and PTCBI are shown in Figure 5.1(c)&(d). A Cross-section schematic of the device used in our study is shown in Figure 5.1(a).

First 40 nm of aluminum metal is DC-sputtered on a clean glass substrate at a base pressure of 2×10^{-6} Torr. Lateral in-plane interdigitated aluminum metal electrodes are then patterned using conventional photolithography. Then, 50nm Polystyrene (PS) interface layer, PTCBI and CuPc are deposited at a rate of 1 \AA/s using thermal evaporation in vacuum at a base pressure of 2×10^{-6} Torr. Infrared spectroscopy is used to study and verify that the evaporated interface layer is PS.

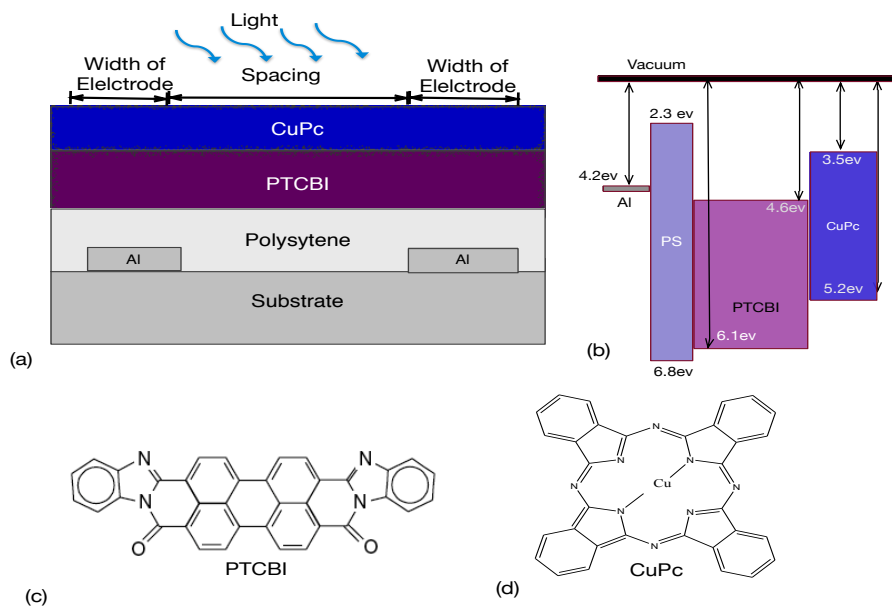


Figure 5.1(a) Schematic crosssection of lateral bilayer organic semiconductor; PS is used as interface layer in between metal contacts and organic semiconductor bilayer. (b) Energy diagram representation. (c) Molecular structure of PTCBI, (d) Molecular structure of CuPc

5.2.2 Measurement

All current-voltage measurements are performed under vacuum using Agilent B1500 source measuring units (SMU). A high power, RGB-LED from LUMEX Corporation is used as the optical source. The LED is powered using one of the 4 SMU channels of the Agilent B1500 semiconductor parameter analyzer with a controlled current and voltage to obtain a fixed output optical power. The optical power incident on the sample is measured using a calibrated Silicon photodetector (Newport photo diode 918D) with a power meter (Newport model 1931-C). Each LED is placed 4 cm above the photo sensor. An in-built optical diffuser in front of the LED allows a uniform spread of light over a large area (>5 cm radius). An Ocean Optics spectrometer (model QE-65000) is used to measure the emission wavelength, and during all measurements, the device is kept in vacuum at room temperature. The measurement set up is shown in figure 5.2.

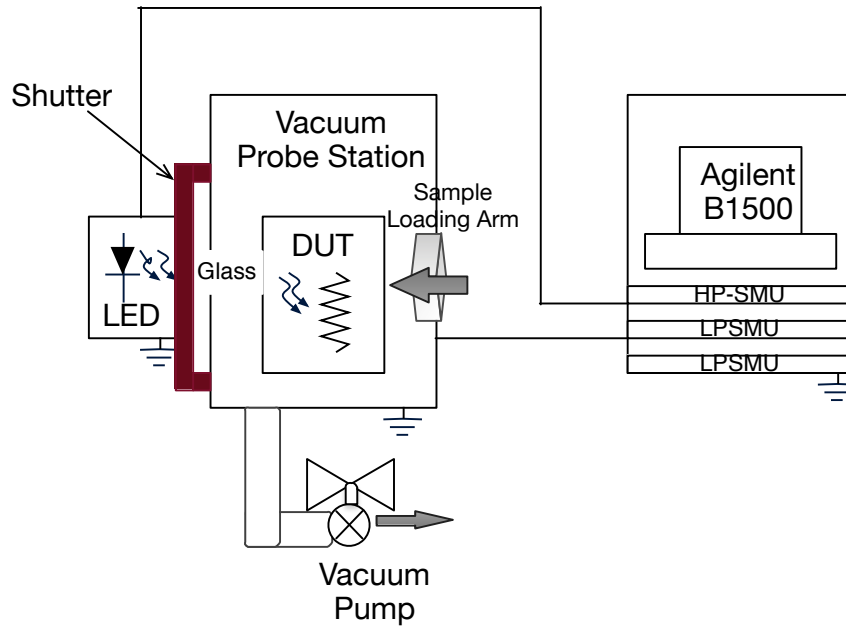


Figure 5.2 Block diagram of the measurement setup used to characterize the devices

5.3 Photodetector performance

Figure 5.3(a) shows the measured photo and dark currents of a lateral organic semiconductor bilayer photodetector using different thickness of PS interface layer at different applied voltage biases. The dark current performance of the photodetector is improved with the use of a PS interface layer. The detector with 50nm PS shows a dark current density of 180 pA/mm^2 . The detector with no

PS has a dark current density of 2.73 nA/mm^2 . The detector with no PS has a dark current density 15 times larger than the detector with the PS interface layer. However, the photocurrent of the detector with the 50 nm PS layer is 1.5 times lower than the detector without PS. It must be emphasized that even with a slight decrease in photocurrent, the photodetector with the PS layer shows a considerable improvement in the photo to dark current ratio, the key performance metric for sensors as shown in Figure 5.3(b), where low dark current and high photo-to-dark current ratios are critical for photodetectors used in most digital imaging applications.

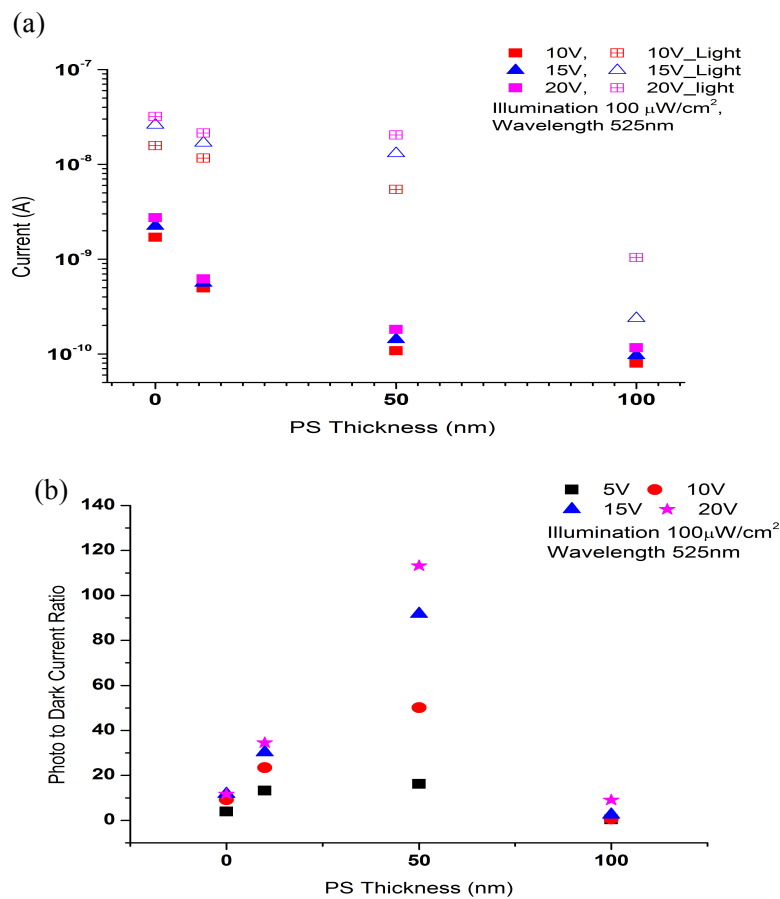


Figure 5.3 (a) Measured photo and dark current for MIOSIM photodetector without-PS, 10nm, 50nm and 100nm of PS at 10V, 15V and 20V applied voltage bias. (b) Photo to dark current ratio at without PS and with different PS thicknesses at different bias voltages

The measured external quantum efficiency (EQE) of the detectors fabricated is listed in Table 1. Here, the EQE is calculated at a 20 V bias under an illumination wavelength of 525 nm and an illumination power of 100 $\mu\text{W}/\text{cm}^2$. When the EQE is calculated at the lower illumination power typical of low light level imaging applications such as in large area digital medical detectors, the results improve and are shown in Table 2 below.

Table 5.1 EQE of lateral organic bilayer photodetector without-PS and with different thicknesses of PS at 5 V, 10 V, 15 V and 20 V applied bias voltages

External Quantum Efficiency (%) At 20V applied bias, 100$\mu\text{W}/\text{cm}^2$ illumination power and 525nm wavelength				
Voltage	No PS	10 nm PS	50 nm PS	100 nm PS
5V	1.48	2.46	0.49	
10V	6.61	5.25	2.5	0.01
15V	11.19	7.64	6.07	0.06
20V	13.78	9.81	9.57	0.4

Table 5.2 EQE at low illumination power

External Quantum Efficiency (%) At 20V applied bias, 10 $\mu\text{W}/\text{cm}^2$ illumination power and 525nm wavelength				
Voltage	No PS	10 nm PS	50 nm PS	100 nm PS
5V	8.64	11.89	0.49	0.06
10V	12.11	15.22	2.39	0.11
15V	13.60	16.80	9.89	0.05
20V	14.45	17.57	11.72	1.82

The EQE can further be increased using a combination of thicker organic bilayers, a thicker PS layer and a higher electric field. Also note that the detector reported with 50 nm PS absorbs only 15%

of the impinging light at a 525 nm wavelength, as shown in figure 3. Since the PS layer does not absorb in the wavelength range 300nm to 850 nm and taking into account the reflection and transmission losses, the resulting device photocurrent is attributed to just 15% of light that is absorbed in the organic active bilayer, which determines the EQE of the detector. If more of the impinging light was absorbed in the organic bilayer, the EQE could in principle be considerably higher. Again, the purpose of this work is not to optimize the layer thickness, rather we are presenting a technique to tune the dark current performance of a lateral bilayer organic semiconductor that warrants further investigation and optimization.

5.3.1 Polystyrene: Conduction

To understand the conduction through the PS layer, two daughter-sample devices are prepared: Sample 1 has lateral aluminum electrodes with a channel lengths of 5 μm and 50 nm of PS; Sample 2 is identical to Sample 1, with an additional metal layer of Aluminum (15 nm) deposited on top of the PS layer. For each sample, voltage is applied across the lateral in-plane electrodes, and the lateral channel current is measured both in dark and under light (white light with an optical power density of 100 mW/cm^2). Sample 1 is measured at an applied voltage bias of 5.2 V (i.e., around 62.5 $\text{V}/\mu\text{m}$) where soft breakdown of the PS occurred. This breakdown is expected because the vertical conduction gap in PS is only 50 nm. In Sample 2, the voltage could be increased up to 100 V on either electrode, but no breakdown current was observed. This finding is also expected because there is no vertical conduction path and because of the 5 μm gap in the PS layer between the metal electrodes. In addition, no photo-generated current is observed in either sample. If the source current is limited, Sample 1 can be operated between a higher resistance low current insulating mode and a bias stress induced leakage with higher injection currents [79]. The high field conduction through PS can be explained as electrons being elevated to the conduction band where they hop between trap states, under the influence of an external electric field [71], [80-84]. The above measurement implies that for 50nm thick PS at an applied bias of 5.2 V and above, conduction through the PS layer is possible. Here, the PS insulator layer acts like a voltage dependent series resistor under low bias voltage.

Furthermore, the PS absorbance data from a 50 nm PS thin film on a glass substrate is used to verify that absorbance is less than 5% over a range of 400 nm to 700 nm incident source wavelength (Figure 5.4).

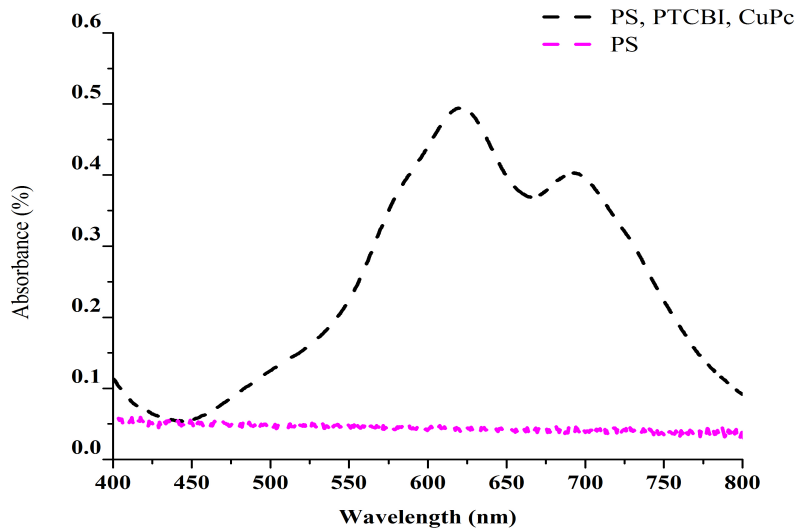


Figure 5.4 Measured absorbance spectrum (400nm to 800nm wavelength) of all three layers (plotted in black) and only PS.

5.3.2 Effect of Electrode Spacing

To investigate the Lateral photosensor design, the bilayer MIOSIM structure Al/PS(50 nm)/PTCBI(50 nm)/CuPc(30 nm) is studied at different combined electrode widths and channel spacing between electrodes. In each case, the overall device area is kept constant (i.e., 1 mm²). Table 2 shows the device parameters being varied.

In Figure 5.5 we see clearly that in the case of dark measurement (i.e., under no light) there is no significant dependence of dark current on the channel length or electrode width. Considering the photosensor D1 and D5, both of these device sets have 50 nm of PS in between the metal contacts and a bilayer comprising 50 nm of PTCBI and 30nm CuPc on top. The overall area of each device is 1x1 mm². As shown in Figure 4, the dark current is not significantly dependent on the electrode spacing in between the interdigitated comb electrodes.

The current voltage responses of sensors D1 and D5 are measured at an optical power density of 400 μW/cm² (green light 525 nm wavelength). The photocurrents of devices D1 and D5 are identical,

indicating a similar weak dependence of photocurrent on the electrode spacing. Consequently, both D1 and D5 have similar photo-to-dark current ratios. To investigate this effect further, we fabricated devices D2, D3 and D4 with different electrode spacing and electrode widths, while keeping the overall sensor area as $1 \times 1 \text{ mm}^2$ as shown in Table 5.3.

Table 5.3 Devices dimensions, electrode width and electrode length

Device	Electrode Spacing (m)	Electrode Width (μm)	Electrode Length (mm)
D1 (5x10)	5 μm	10 μm	1mm
D2 (5x5)	5 μm	5 μm	1mm
D3 (15x10)	15 μm	10 μm	1mm
D4 (10x10)	10 μm	10 μm	1mm
D5 (10x5)	10 μm	5 μm	1mm

The current voltage response is measured under dark and light (525 nm wavelength) at $400 \mu\text{W}/\text{cm}^2$ optical power, and the results are included in Figure 5.5.

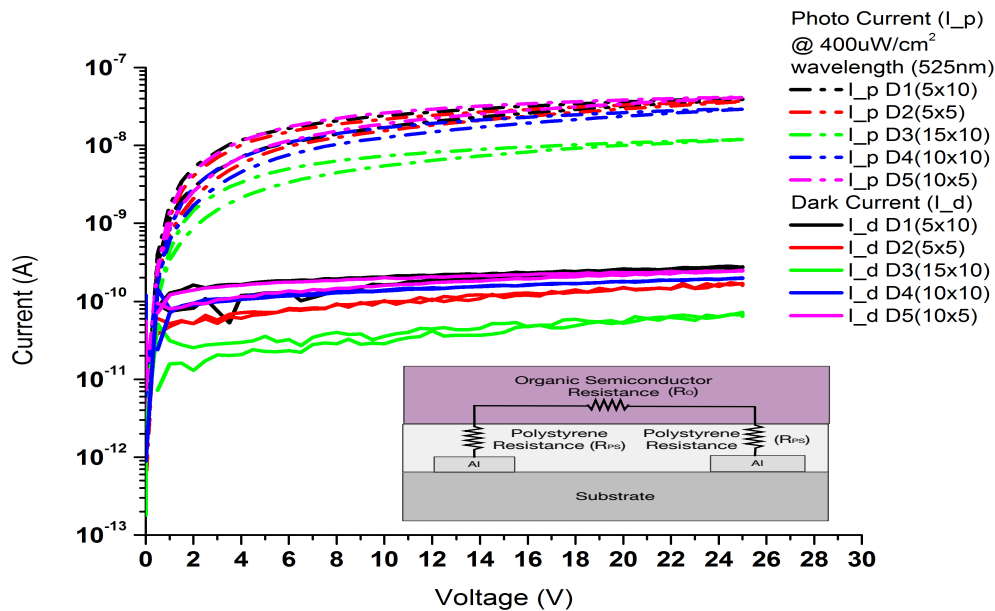


Figure 5.5 Current Voltage characteristics of Device 1 to 5 (D1 to D5) in dark (continuous line) and light (dotted line), illumination power density $400 \mu\text{W}/\text{cm}^2$, 525nm wavelength, Device area 1mm^2 .

Devices D1, D3, and D4 have $10 \mu\text{m}$ of electrode width and channel lengths of $5 \mu\text{m}$, $15 \mu\text{m}$, and $10 \mu\text{m}$, respectively. For device D1 and D4, the measured photo and dark current show no dependence on the electrode spacing. However, in case of Device D3, which has $15 \mu\text{m}$ of channel length, the photo and dark current are lower than those of the other two devices (D1 and D4); however, the photo-to-dark current ratio does not change. We believe this is due to a larger contribution of the channel resistance to the overall device resistance as shown in Figure 4 inset. A simple manner of understanding this is that the longer channel length increases the relative contribution of channel resistance when compared to the vertical contact resistance through the PS at each electrode.

For the shorter channel length devices, particularly Devices D2 (5×5) and D5 (10×5) with the same electrode width and different channel lengths, identical photo and dark currents are observed verifying the hypothesis of no dependence of photo and dark current on electrode spacing. Thus, the experimental results suggest that the conduction channel through PS in the reported MIOSIM structure with the specific bilayer material and thicknesses is vertical for channel lengths at $10 \mu\text{m}$ or less. For devices with longer channel lengths, if the bilayer thickness and/or material is changed (for

example, to yield a lower channel resistance), then the PS layer may again define the dark and photocurrent response. The value of this insight is that the MIOSIM device provides an additional design parameter, the PS layer.

Considering the thickness of the PS (50nm) insulator layer, it is assumed that charge tunneling through the insulator is not likely because the layer is too thick [85]. So the dark current is probably due to (1) the conduction of injected charges into the randomly distributed defect states present at the metal insulator interface and the bulk of the insulator material and (2) the excess charges that overcome the energy barriers between the metal work function and conduction energy of the insulator. It is observed from the Dark I-V characteristics of the device that the dark current reaches a steady-state condition at a certain threshold bias (V_t). At V_t , it is likely that all the deep traps get filled and due to low conductivity of the organic layers a space charge limited condition is achieved that balances out the injection to the opposing potential buildup at the electrodes (resembling the charging of a capacitor).

5.4 Mathematical Analysis

Mathematically, the current density of a MIOSIM photosensor is the sum of the dark and photo current density under the applied external voltage bias, as given in Eq.1.

$$J_{\text{Device}} = J_{\text{Dark}} + J_{\text{Photo}} \quad (1)$$

The photosensor photocurrent saturates after threshold voltage (V_t), above which all the free electrons and holes are removed from the semiconductor. Assuming no charge injection and no recombination, the photocurrent can be written in the form of the standard drift equation [46] shown in Eq.2

$$J_{\text{Photo}} = qG_{\text{Opt}}L, \quad (2)$$

Where q is the electronic charge, G_{opt} is the net optical generation rate of the electron-hole pair, and L is the channel length[86]. Since there is no recombination and injection, the carriers contributing to the photo current have a drift length $d_{h,e} \geq L$ under steady state.

The drift length of the hole and electron is given by $d_{h(e)} = \mu_{h(e)}\tau_{h(e)} E$, where $\mu_{h(e)}$ is the charge carrier mobility of hole or electron, $\tau_{h,e}$ is charge carrier life time, and E is the electric field. In the heterojunction design, the light absorption leads to the production of excitons, which later dissociate at the heterojunction (PTCBI-CuPc) and are transferred to the PTCBI and CuPc layer. Due to spatial separation of these electrons and holes, back transfer is not possible, leading to long-lived carriers

From the literature [87] [19], we know that in lateral photosensor geometry, the dominant region governing the generation and recombination of carriers is near or above one of the device electrodes. For example, in the case of bottom hole transport layer (HTL) and top exciton generation layer (EGL) bilayer photosensor design, the HTL above the cathode electrode is dominantly contributing to photocurrent [87] [19]. In our MIOSIM photodetector design, PTCBI is the electron transport layer, next to the interface layer (PS), we expect that the dominant space charge limited region will be at the anode electrode (positively biased). In this case, we can assume that the Photo-generated electrons contributing to the photo current will have a drift length equal to the thickness (x_{PTCBI}) of PTCBI ($d_e = x_{\text{PTCBI}}$), and overall channel length (electrode spacing) becomes less important (i.e.; $L = x_{\text{PTCBI}}$) as given in Eq. 3. The saturated photo current from Eq. 2 can therefore be written as

$$J_{\text{Photo}} = qG_{\text{Opt}}x_{\text{PTCBI}} \quad (3)$$

where

$$L = x_{\text{PTCBI}} = \mu_e\tau_e E \quad (4).$$

The applied voltage potential (V) will drop (V_{PS}), mostly across the interface layer (PS), due to its high resistance and to a lesser extent across the PTCBI layer (i.e., $V - V_{PS}$). So the electric field in PTCBI is given by $E = (V - V_{PS})/x_{PTCBI}$. Using this relationship, we can rewrite Eq. 4

$$x_{PTCBI} = \mu_e \tau_e (V - V_{PS})/x_{PTCBI} \quad (5)$$

Substituting Eq. 5 in Eq. 3, the space charge independent photocurrent of the device can be written as Eq. 6

$$J_{Photo} = qG_{Opt}(\mu_e \tau_e)^{1/2} (V - V_{PS})^{1/2} \quad (6)$$

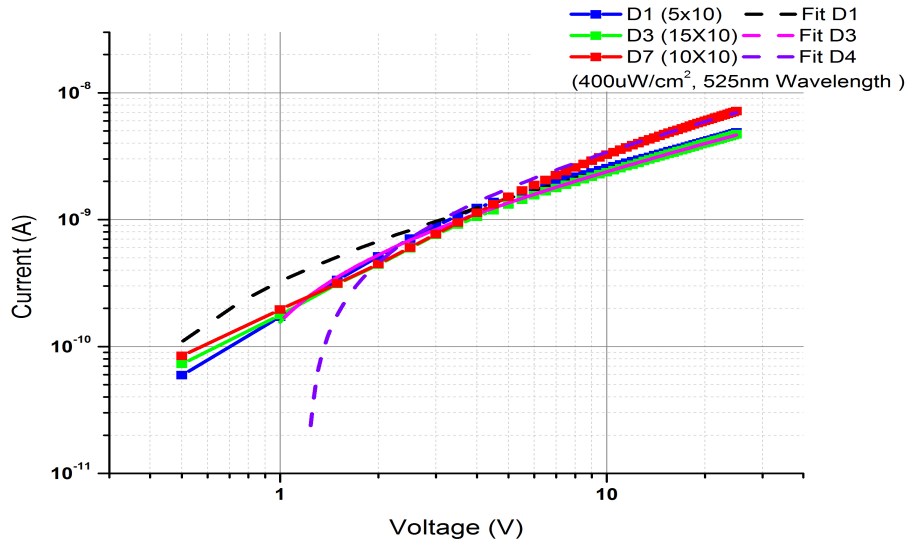


Figure 5.6 Log-log plot for sensor (D1, D3 and D4) photocurrent vs voltage (solid plot) at light power of $400 \mu W/cm^2$ and nonlinear fit plots (dotted plot)

In the above equation (Eq.6), it is important to mention that the photocurrent is dependent on the square root of the voltage, which has been reported previously for vertical devices or for bulk heterojunction lateral devices[88], [89]. Here, the square root of voltage dependency is observed in a

lateral bilayer heterojunction MIOSIM device. In order to verify the square root dependence of the photocurrent, we plotted the photocurrent vs voltage for devices D1, D3 and D5 on a log-log scale. A non-linear fit for voltages above V_t is performed using equation ($I = A + BV^c$), as shown in Figure 5.6. We calculated a non-linear fit parameter with a value ranging from 0.63 to 0.69 which is close to the expected value of 0.5. The deviation in results are potentially due to assumptions made in deriving Eq.6, for example, one dimensional transport, no recombination in the channel, and no charge injection from the metal contact into the semiconductor layers.

5.5 Conclusion

In summary, results from measurements show that the vertical injection from the metal through the insulator defines the current in a MIOSIM photo sensor rather than the channel length between the injecting electrodes as reported previously for similar devices. Currents are highly dependent on the thickness of the EGL, which also serves as the charge transport layer. Thus, the EGL primarily defines the photocurrent in this lateral MIOSIM device, which is in contrast to what is reported for other lateral photosensor devices where the gap between the electrodes (i.e., the channel length) is a critical factor. To achieve higher device efficiency and low dark currents, it is critical to tune the thickness of the active layer and insulator, respectively.

Chapter 6

Summary and Contributions

6.1 Summary

The existing large area medical X-ray, digital detector systems use a-Si flat panel detectors. These flat panels are fabricated on glass substrates that are heavy, fragile and expensive. Replacing glass with low cost plastic can significantly reduce the over all weight of the detector and provide added benefits such as mechanical flexibility and low cost compared to the existing state-of-the-art detectors. Low cost plastic cannot sustain high temperatures; therefore, the existing a-Si technology cannot be adapted to process large-area panel on low-cost plastic substrate. As an alternative, organic semiconductor technology can be used to realize flexible, lightweight, and low-cost X-ray imagers.

The first part of this thesis has shown the possibility of using organic semiconductor solution process technology to fabricate large-area active-matrix digital imagers. These imagers are fabricated on a flexible substrate composed of, Polyethylene Naphthalate (PEN) foil. Vertical organic semiconductor photodiodes are monolithically integrated with an active matrix solution processed organic thin film transistor backplane. The integrated OPD backplane is coupled to a scintillator, and X-ray images are extracted using an external readout. The integrated backplane require a continuous transparent top electrode. The need for transparent electrodes adds additional complexity to the design. The continuous conducting anode adds considerable electronic noise to the imager. The sensitivity of the imager is mainly limited, mainly due to the high dark current of the vertical photodiodes. In order to address the challenges associated with the vertical photodetector design, an alternative design is proposed, consisting of lateral multilayer photodetector structure.

The lateral photodetector design uses a heterojunction donor and acceptor interface structure. The heterojunction interface improves the photo-performance of the photodetectors by providing an energetically favorable space for Photo-generated excitons to separate and a low resistive channel generated by the diffusion and dipole interface region. The dark current performance of the photodetector is improved by using a a non-polar insulation-interface layer, polystyrene. The addition of a polystyrene layer permits the application of a high bias voltage without increasing the photodetector's dark current. The presented detector shows a reasonable response time, high photo-to-dark current ratio, low dark current, and high EQE. Furthermore, the lateral photodetector with interface layer has a high dynamic range and improved sensitivity that is ideal for detecting low

intensities of light in the range of a few $\mu\text{W}/\text{cm}^2$. Low light sensitivity is critically important; for instance, in indirect X-ray detectors, the scintillator's optical output is low. The proposed detector has a linear response to incident light (green light wavelength). Further, the transparent electrode is not needed, and the lateral detector can be easily integrated with the backplane circuit, either on the top of the TFT or in a coplanar fashion.

We have also investigated the effect of channel spacing in a lateral multilayer organic semiconductor photodetector design, using an interface layer, and have shown the non intuitive effect of channel spacing on the photodetector photo and dark current. The conduction mechanism is found to be vertical instead of lateral, meaning that the dark and the photocurrents of the lateral photodetector are not dependent on the channel length but on each film's vertical thickness. Lastly, due to the non-dependence of the channel length, the fill factor of the lateral photodetector can be considered comparable to that of the vertical photodetector design.

6.2 Contributions

This work has shown the potential of using organic semiconductor technology in large-area digital imaging. A few of the major contribution are as follows:

- To provide a practical demonstration of a flexible large area digital imager for X-ray imaging. A vertical photodiode detector is integrated with a TFT backplane, and the performance of the fabricated imager is evaluated. This work has been conducted at HOLST Center, and Philips Research, in Eindhoven, The Netherlands, and the results have been reported in the form of a publication in *Organic Electronics Journal* (2013) and *SPIE Photonics Europe conference (2014)*, which I coauthored.
- To overcome the challenges associated with the vertical photodiode for its use in imager. We have reported an organic semiconductor lateral bilayer photodetector using CuPc and PTCBI organic materials. We have shown that the use of single layer and multilayer devices and established a methodology to improve lateral photodetector performance. This part of the work has been reported at the *SPIE Medical Imaging Conference* (2011).

- To improve lateral detector performance a interface layer is introduced. The use of a interface layer to improve photodetector performance and the effect of using a poorly conducting interface layer is reported at the *MRS conference* (2014).
- To present detail study of the interface layer, including photodetector performance, lateral channel length effect on the lateral photodetector dark and photocurrents. This research has been reported in *IEEE transaction of Electron Devices* as two separate articles. These articles are under review (2014).

A manuscript is in preparation that addresses the use of a thin photoconductive active layer to improve detector speed.

Bibliography

- [1] F. Li, A. Nathan, Y. Wu, and B. S. Ong, *Organic Thin Film Transistor Integration*. John Wiley & Sons, 2013, p. 268.
- [2] X. Tong and S. R. Forrest, “An integrated organic passive pixel sensor,” *Organic Electronics*, vol. 12, no. 11, pp. 1822–1825, Nov. 2011.
- [3] G. H. Gelinck, A. Kumar, D. Moet, J.-L. van der Steen, U. Shafique, P. E. Malinowski, K. Myny, B. P. Rand, M. Simon, W. Rütten, A. Douglas, J. Jorritsma, P. Heremans, and R. Andriessen, “X-ray imager using solution processed organic transistor arrays and bulk heterojunction photodiodes on thin, flexible plastic substrate,” *Organic Electronics*, vol. 14, no. 10, pp. 2602–2609, Oct. 2013.
- [4] G. H. Gelinck, H. E. A. Huitema, E. van Veenendaal, E. Cantatore, L. Schrijnemakers, J. B. van der Putten, T. C. Geuns, M. Beenhakkers, J. B. Giesbers, and B.-H. Huisman, “Flexible active-matrix displays and shift registers based on solution-processed organic transistors,” *nature materials*, vol. 3, no. 2, pp. 106–110, 2004.
- [5] S. Kasap, J. B. Frey, G. Belev, O. Tousignant, H. Mani, J. Greenspan, L. Laperriere, O. Bubon, A. Reznik, G. DeCrescenzo, K. S. Karim, and J. A. Rowlands, “Amorphous and Polycrystalline Photoconductors for Direct Conversion Flat Panel X-ray Image Sensors,” *Sensors*, vol. 11, no. 12, pp. 5112–5157, Dec. 2011.
- [6] A. Noel and F. Thibault, “Digital detectors for mammography: the technical challenges,” *European radiology*, vol. 14, no. 11, pp. 1990–1998, 2004.
- [7] M. Binda, D. Natali, M. Sampietro, T. Agostinelli, and L. Beverina, “Organic based photodetectors Suitability for X- and Γ -rays sensing application,” *Nuclear Inst. and Methods in Physics Research, A*, vol. 624, no. 2, pp. 443–448, Dec. 2010.
- [8] Q. Chen, T. Hajagos, and Q. Pei, “Conjugated polymers for radiation detection,” *Annu. Rep. Prog. Chem., Sect. C: Phys. Chem.*, vol. 107, p. 298, 2011.
- [9] C. W. Tang, “Two-layer organic photovoltaic cell,” *Appl. Phys. Lett.*, vol. 48, no. 2, p. 183, 1986.

- [10] J. Wang, H. Wang, X. Yan, H. Huang, and D. Yan, "Organic heterojunction and its application for double channel field-effect transistors," *Appl. Phys. Lett.*, vol. 87, no. 9, p. 093507, 2005.
- [11] K.-J. Baeg, M. Binda, D. Natali, M. Caironi, and Y.-Y. Noh, "Organic Light Detectors: Photodiodes and Phototransistors," *Adv. Mater.*, vol. 25, no. 31, pp. 4267–4295, Mar. 2013.
- [12] H. Wang and D. Yan, "Organic heterostructures in organic field-effect transistors," *NPG Asia Mater*, vol. 2, no. 2, pp. 69–78, Apr. 2010.
- [13] S. H. Park, A. Roy, S. Beaupré, S. Cho, N. Coates, J. S. Moon, D. Moses, M. Leclerc, K. Lee, and A. J. Heeger, "Bulk heterojunction solar cells with internal quantum efficiency approaching 100%," *Nature Photon*, vol. 3, no. 5, pp. 297–302, Apr. 2009.
- [14] P. Peumans, V. Bulovic, and S. R. Forrest, "Efficient, high-bandwidth organic multilayer photodetectors," *Appl. Phys. Lett.*, vol. 76, no. 26, pp. 3855–3857, 2000.
- [15] W.-W. Tsai, Y.-C. Chao, E.-C. Chen, H.-W. Zan, H.-F. Meng, and C.-S. Hsu, "Increasing organic vertical carrier mobility for the application of high speed bilayered organic photodetector," *Appl. Phys. Lett.*, vol. 95, no. 21, p. 213308, 2009.
- [16] P. Peumans, A. Yakimov, and S. R. Forrest, "Small molecular weight organic thin-film photodetectors and solar cells," *J. Appl. Phys.*, vol. 93, no. 7, p. 3693, 2003.
- [17] D.-S. Leem, K.-H. Lee, K.-B. Park, S.-J. Lim, K.-S. Kim, Y. Wan Jin, and S. Lee, "Low dark current small molecule organic photodetectors with selective response to green light," *Appl. Phys. Lett.*, vol. 103, no. 4, p. 043305, 2013.
- [18] K.-H. Lee, D.-S. Leem, J. S. Castrucci, K.-B. Park, X. Bulliard, K.-S. Kim, Y. W. Jin, S. Lee, T. P. Bender, and S. Y. Park, "Green-Sensitive Organic Photodetectors with High Sensitivity and Spectral Selectivity Using Subphthalocyanine Derivatives," *ACS Appl. Mater. Interfaces*, vol. 5, no. 24, pp. 13089–13095, Dec. 2013.
- [19] Z. E. Ooi, K. Chan, C. Lombardo, and A. Dodabalapur, "Analysis of photocurrents in lateral-geometry organic bulk heterojunction devices," *Appl. Phys. Lett.*, vol. 101, no. 5, pp. 053301–053301–5, 2012.

- [20] J. W. Kingsley, S. J. Weston, and D. G. Lidzey, "Stability of X-ray detectors based on organic photovoltaic devices," *Selected Topics in Quantum Electronics, IEEE Journal of*, vol. 16, no. 6, pp. 1770–1775, 2010.
- [21] A. C. Niemeyer, I. H. Campbell, F. So, and B. K. Crone, "High quantum efficiency polymer photoconductors using interdigitated electrodes," *Appl. Phys. Lett.*, vol. 91, no. 10, p. 103504, 2007.
- [22] J. C. Ho, A. Arango, and V. Bulovic, "Lateral organic bilayer heterojunction photoconductors," *Appl. Phys. Lett.*, vol. 93, no. 6, p. 063305, 2008.
- [23] T. P. Osedach, S. M. Geyer, J. C. Ho, A. C. Arango, M. G. Bawendi, and V. Bulovic, "Lateral heterojunction photodetector consisting of molecular organic and colloidal quantum dot thin films," *Appl. Phys. Lett.*, vol. 94, no. 4, p. 043307, 2009.
- [24] S. F. Tedde, J. Kern, T. Sterzl, J. F u rst, P. Lugli, and O. Hayden, "Fully spray coated organic photodiodes.," *Nano letters*, vol. 9, no. 3, pp. 980–983, Mar. 2009.
- [25] S. Tedde, E. S. Zaus, J. Fürst, D. Henseler, and P. Lug li, "Active pixel concept combined with organic photodiode for imaging devices," *IEEE Electron Device Letters*, vol. 28, no. 10, pp. 893–895, 2007.
- [26] T. Agostinelli, M. Campoy-Quiles, J. C. Blakesley, R. Speller, D. D. C. Bradley, and J. Nelson, "A polymer/fullerene based photodetector with extremely low dark current for X-ray medical imaging applications," *Appl. Phys. Lett.*, vol. 93, no. 20, p. 203305, 2008.
- [27] M. Ramuz, L. Bürgi, C. Winnewisser, and P. Seitz, "High sensitivity organic photodiodes with low dark currents and increased lifetimes," *Organic Electronics*, vol. 9, no. 3, pp. 369–376, 2008.
- [28] T. N. Ng, W. S. Wong, M. L. Chabiny, S. Sambandan, and R. A. Street, "Flexible image sensor array with bulk heterojunction organic photodiode," *Appl. Phys. Lett.*, vol. 92, no. 21, p. 213303, 2008.
- [29] S. Valouch, C. Hönes, S. W. Kettlitz, N. Christ, H. Do, M. F. G. Klein, H. Kalt, A. Colmann, and U. Lemmer, "Solution processed small molecule organic interfacial layers for low dark current polymer photodiodes," *Organic Electronics*, vol. 13, no. 11, pp. 2727–2732, Nov. 2012.

- [30] L. Chen, P. Degenaar, and D. D. Bradley, "Polymer transfer printing: application to layer coating, pattern definition, and diode dark current blocking," *Adv. Mater.*, vol. 20, no. 9, pp. 1679–1683, 2008.
- [31] T. Someya, Y. Kato, S. Iba, Y. Noguchi, T. Sekitani, H. Kawaguchi, and T. Sakurai, "Integration of organic FETs with organic photodiodes for a large area, flexible, and lightweight sheet image scanners," *Electron Devices, IEEE Transactions on*, vol. 52, no. 11, pp. 2502–2511, 2005.
- [32] I. Nausieda, K. Ryu, I. Kymissis, A. Ibitayo Tayo Akinwande, V. Bulovi, and C. G. Sodini, "An Organic Active-Matrix Imager," *Electron Devices, IEEE Transactions on*, vol. 55, no. 2, pp. 527–532.
- [33] C. K. Renshaw, X. Xu, and S. R. Forrest, "A monolithically integrated organic photodetector and thin film transistor," *Organic Electronics*, vol. 11, no. 1, pp. 175–178, Jan. 2010.
- [34] D. Baierl, L. Pancheri, M. Schmidt, D. Stoppa, G.-F. Dalla Betta, G. Scarpa, and P. Lugli, "A hybrid CMOS-imager with a solution-processable polymer as photoactive layer," *Nature Communications*, vol. 3, p. 1175, 2012.
- [35] R. Lujan and R. Street, "Flexible X-ray Detector Array Fabricated With Oxide Thin-Film Transistors," *Electron Device Letters, IEEE*, vol. 33, no. 5, p. 688, 2012.
- [36] J. C. Blakesley, P. E. Keivanidis, M. Campoy-Quiles, C. R. Newman, Y. Jin, R. Speller, H. Sirringhaus, N. C. Greenham, J. Nelson, and P. Stavrinou, "Organic semiconductor devices for X-ray imaging," *Nuclear Inst. and Methods in Physics Research, A*, vol. 580, no. 1, pp. 774–777, Jan. 2007.
- [37] B. Bolto, R. McNeill, and D. Weiss, "Electronic conduction in polymers. III. Electronic properties of polypyrrole," *Australian Journal of Chemistry*, vol. 16, no. 6, pp. 1090–1103, 1963.
- [38] P. Stallinga, *Electrical Characterization of Organic Electronic Materials and Devices*. Wiley Online Library, 2009.
- [39] F. So, *Organic Electronics*. CRC Press, 2010, p. 581.
- [40] C. D. Dimitrakopoulos and D. J. Mascaró, "Organic thin-film transistors: A review of recent advances," *IBM Journal of Research and Development*, vol. 45, no. 1, pp. 11–27, 2001.

- [41] G. Yu, G. Srdanov, J. Wang, H. Wang, Y. Cao, and A. J. Heeger, "Large area, full-color, digital image sensors made with semiconducting polymers," *Synthetic Metals*, vol. 111, pp. 133–137, 2000.
- [42] H. Klauk, U. Zschieschang, J. Pflaum, and M. Halik, "Ultralow-power organic complementary circuits," *Nature*, vol. 445, no. 7129, pp. 745–748, Feb. 2007.
- [43] C. Tang, H. Xu, F. Liu, Y.-J. Xia, and W. Huang, "Isolated large π systems in pyrene–fluorene derivatives for intramolecular through-space interaction in organic semiconductors," *Organic Electronics*, vol. 14, no. 3, pp. 782–789, 2013.
- [44] D. Hertel and H. Bässler, "Photoconduction in Amorphous Organic Solids," *ChemPhysChem*, vol. 9, no. 5, pp. 666–688, Mar. 2008.
- [45] W. Brütting, *Physics of Organic Semiconductors*, 1st ed. Wiley-VCH, 2006, p. 554.
- [46] S. L. Chuang, *Physics of Optoelectronic Devices*. Wiley-Interscience, 1995, p. 736.
- [47] A. Miller and E. Abrahams, "Impurity Conduction at Low Concentrations," *Phys. Rev.*, vol. 120, no. 3, pp. 745–755, Nov. 1960.
- [48] S. R. Forrest, "Ultrathin organic films grown by organic molecular beam deposition and related techniques," *Chem. Rev.*, vol. 97, no. 6, pp. 1793–1896, 1997.
- [49] M. Yeke Yazdandoost, "Photon Quantum Noise Limited Pixel and Array architectures in a-Si Technology for Large Area Digital Imaging Applications," 2011.
- [50] I. Nausieda, R. Kyungbum, I. Kymissis, A. Akinwande, V. Bulovic, and C. G. Sodini, "An organic active-matrix imager," *Electron Devices, IEEE Transactions on*, vol. 55, no. 2, pp. 527–532, 2008.
- [51] H. Klauk, *Organic Electronics: Materials, Manufacturing, and Applications*. 2006, pp. 1–449.
- [52] R. Wehrspohn, S. Deane, I. French, and M. Powell, "Stability of plasma deposited thin film transistors—comparison of amorphous and microcrystalline silicon," *Thin Solid Films*, vol. 383, no. 1, pp. 117–121, 2001.
- [53] S. Lilliu, M. Böberl, M. Sramek, S. F. Tedde, J. E. Macdonald, and O. Hayden, "Inkjet-printed organic photodiodes," *Thin Solid Films*, vol. 520, no. 1, pp. 610–615, Oct. 2011.

- [54] E. S. Zaus, S. Tedde, T. Rauch, J. Furst, and G. H. Dohler, "Design of highly transparent organic photodiodes," *Electron Devices, IEEE Transactions on*, vol. 55, no. 2, pp. 681–684, 2008.
- [55] F. Arca, S. F. Tedde, M. Sramek, J. Rauh, P. Lugli, and O. Hayden, "Interface Trap States in Organic Photodiodes," *Sci. Rep.*, vol. 3, 2013.
- [56] F. V. Assche, H. Rooms, E. Young, J. Michels, T. V. Mol, G. Rietjens, P. Weijer, and P. Bouten, "Thin-film barrier on foil for organic LED lamps," vol. 3, pp. 1152–1173, 2008.
- [57] D. Baierl, B. Fabel, P. Gabos, L. Pancheri, P. Lugli, and G. Scarpa, "Solution-processable inverted organic photodetectors using oxygen plasma treatment," *Organic Electronics*, vol. 11, no. 7, pp. 1199–1206, Jul. 2010.
- [58] C. W. E. V. Eijk, "Inorganic scintillators in medical imaging," *Phys. Med. Biol.*, vol. 47, no. 8, pp. R85–R106, Apr. 2002.
- [59] R. A. B. Devine, M.-M. Ling, A. B. Mallik, M. Roberts, and Z. Bao, "X-ray irradiation effects in top contact, pentacene based field effect transistors for space related applications," *Appl. Phys. Lett.*, vol. 88, no. 15, p. 151907, 2006.
- [60] P. E. Keivanidis, N. C. Greenham, H. Sirringhaus, R. H. Friend, J. C. Blakesley, R. Speller, M. Campoy Quiles, T. Agostinelli, D. D. C. Bradley, and J. Nelson, "X-ray stability and response of polymeric photodiodes for imaging applications," *Appl. Phys. Lett.*, vol. 92, no. 2, p. 023304, 2008.
- [61] X. Gong, M.-H. Tong, S. H. Park, M. Liu, A. Jen, and A. J. Heeger, "Semiconducting Polymer Photodetectors with Electron and Hole Blocking Layers: High Detectivity in the Near-Infrared," *Sensors*, vol. 10, no. 7, pp. 6488–6496, Jul. 2010.
- [62] U. Shafique and K. S. Karim, "Lateral organic photodetectors for imaging applications," in *Lateral organic photodetectors for imaging applications*, Lake Buena Vista, FL, 2011, vol. 7961, pp. 796103–796103–6.
- [63] J. W. Kingsley, A. J. Pearson, L. Harris, S. J. Weston, and D. G. Lidzey, "Detecting 6MV X-rays using an organic photovoltaic device," *Organic Electronics*, vol. 10, no. 6, pp. 1170–1173, Sep. 2009.

- [64] J. Xue and S. R. Forrest, "Carrier transport in multilayer organic photodetectors: I. Effects of layer structure on dark current and photoresponse," *J. Appl. Phys.*, vol. 95, no. 4, pp. 1859–1868, 2004.
- [65] J. Xue and S. R. Forrest, "Carrier transport in multilayer organic photodetectors: II. Effects of anode preparation," *J. Appl. Phys.*, vol. 95, no. 4, pp. 1869–1877, 2004.
- [66] T. Matsushima, H. Sasabe, and C. Adachi, "Carrier injection and transport characteristics of copper phthalocyanine thin films under low to extremely high current densities," *Appl. Phys. Lett.*, vol. 88, no. 3, p. 033508, 2006.
- [67] M. Kitamura, T. Imada, S. Kako, and Y. Arakawa, "Time-of-Flight Measurement of Lateral Carrier Mobility in Organic Thin Films," *Jpn. J. Appl. Phys.*, vol. 43, no. 4, pp. 2326–2329, Apr. 2004.
- [68] K. Onlaor, B. Tunhoo, P. Keeratithiwakorn, T. Thiwawong, and J. Nukeaw, "Electrical bistable properties of copper phthalocyanine at different deposition rates," *Solid State Electronics*, vol. 72, no. C, pp. 60–66, Jun. 2012.
- [69] S. P. Singh, A. Sellinger, and A. Dodabalapur, "Electron transport in copper phthalocyanines," *J. Appl. Phys.*, vol. 107, no. 4, p. 044509, 2010.
- [70] Y. Lu, W. H. Lee, H. S. Lee, Y. Jang, and K. Cho, "Low-voltage organic transistors with titanium oxide/polystyrene bilayer dielectrics," *Appl. Phys. Lett.*, vol. 94, no. 11, p. 113303, 2009.
- [71] A. Kawamoto, Y. Suzuoki, T. Ikejiri, T. Mizutani, and M. Ieda, "Photoinjection currents in polymers and electronic charge-exchange at the interface in insulating composites," in *Electrical Insulating Materials, 1995. International Symposium on*, 1995, pp. 169–172.
- [72] I. Khodami, F. Taghibakhsh, and K. S. Karim, "UV-enhanced a-Si: H metal–semiconductor–metal photodetector," *Electron Device Letters, IEEE*, vol. 29, no. 9, pp. 1007–1010, 2008.
- [73] K. Wang, F. Chen, G. Belev, S. Kasap, and K. S. Karim, "Lateral metal–semiconductor–metal photodetectors based on amorphous selenium," *Appl. Phys. Lett.*, vol. 95, no. 1, pp. 013505–013505–3, 2009.
- [74] K. Wang, F. Chen, N. Allec, and K. S. Karim, "Fast Lateral Amorphous-Selenium Metal–Semiconductor–Metal Photodetector With High Blue-to-Ultraviolet Responsivity," *Electron Devices, IEEE Transactions on*, vol. 57, no. 8, pp. 1953–1958, 2010.

- [75] F. Taghibakhsh, I. Khodami, and K. S. Karim, "Characterization of Short-Wavelength-Selective a-Si:H MSM Photoconductors for Large-Area Digital-Imaging Applications," *Electron Devices, IEEE Transactions on*, vol. 55, no. 1, pp. 337–342, 2008.
- [76] S. Ghanbarzadeh, S. Abbaszadeh, and K. S. Karim, "Low Dark Current Amorphous Silicon Metal-Semiconductor-Metal Photodetector for Digital Imaging Applications," *IEEE Electron Device Letters*, vol. 35, no. 2, pp. 235–237.
- [77] M. R. Esmaeili-Rad and S. Salahuddin, "High Performance Molybdenum Disulfide Amorphous Silicon Heterojunction Photodetector," *Sci. Rep.*, vol. 3, Aug. 2013.
- [78] S. Abbaszadeh, N. Allec, and K. S. Karim, "Characterization of Low Dark-Current Lateral Amorphous-Selenium Metal-Semiconductor-Metal Photodetectors," *Sensors Journal, IEEE*, vol. 13, no. 5, pp. 1452–1458, 2013.
- [79] M. Depas, T. Nigam, and M. M. Heyns, "Soft breakdown of ultra-thin gate oxide layers," *IEEE Transactions on Electron Devices*, vol. 43, no. 9, pp. 1499–1504, 1996.
- [80] D. Prime and S. Paul, "Electrical and morphological properties of polystyrene thin films for organic electronic applications," *Vacuum*, vol. 84, no. 10, pp. 1240–1243, 2010.
- [81] C. Hanna and A. Abass, "Optical properties of polystyrene and benzoate ester of polystyrene thin layers," *J. Appl. Phys.*, vol. 63, p. 5194, 1988.
- [82] U. Lachish and I. Steinberger, "Electrical current measurements on polystyrene films," *J. Phys. D: Appl. Phys.*, vol. 7, no. 1, p. 58, 1974.
- [83] Y. Kulshrestha and A. Srivastava, "Electrical conduction in solution-grown films of commercial grade polystyrene," *Thin Solid Films*, vol. 69, no. 3, pp. 269–274, 1980.
- [84] R. Bahri, "Solution-grown thin polystyrene films. I. DC electrical conduction," *J. Phys. D: Appl. Phys.*, vol. 15, no. 4, p. 677, 1982.
- [85] N. Tessler, Y. Preezant, N. Rappaport, and Y. Roichman, "Charge Transport in Disordered Organic Materials and Its Relevance to Thin-Film Devices: A Tutorial Review," *Adv. Mater.*, vol. 21, no. 27, pp. 2741–2761, May 2009.

- [86] A. M. Goodman and A. Rose, “Double Extraction of Uniformly Generated Electron-Hole Pairs from Insulators with Noninjecting Contacts,” *J. Appl. Phys.*, vol. 42, no. 7, pp. 2823–2830, 1971.
- [87] W. Woestenborghs, P. De Visschere, F. Beunis, G. Van Steenberge, K. Neyts, and A. Vetsuypens, “Analysis of a transparent organic photoconductive sensor,” *Organic Electronics*, vol. 13, no. 11, pp. 2250–2256, Nov. 2012.
- [88] V. Mihailetschi, J. Wildeman, and P. Blom, “Space-charge limited photocurrent,” *Phys. Rev. Lett.*, vol. 94, no. 12, p. 126602, 2005.
- [89] C. J. Lombardo, M. S. Glaz, Z.-E. Ooi, D. A. Vanden Bout, and A. Dodabalapur, “Scanning photocurrent microscopy of lateral organic bulk heterojunctions,” *Phys. Chem. Chem. Phys.*, vol. 14, no. 38, p. 13199, 2012.